CONTROLLING THE SYNTHESIS OF BUNTE SALT STABILIZED GOLD NANOPARTICLES USING A MICROREACTOR PLATFORM IN CONCERT WITH SMALL ANGLE X-RAY SCATTERING ANALYSIS

by

PATRICK MICHAEL HABEN

A DISSERTATION

Presented to the Department of Chemistry
and the Graduate School of the University of Oregon
in partial fulfillment of the requirements
for the degree of
Doctor of Philosophy

September 2013

DISSERTATION APPROVAL PAGE

Student: Patrick Michael Haben

Title: Controlling the Synthesis of Bunte Salt Stabilized Gold Nanoparticles Using a Microreactor Platform in Concert with Small Angle X-ray Scattering Analysis

This dissertation has been accepted and approved in partial fulfillment of the requirements for the Doctor of Philosophy degree in the Department of Chemistry by:

Mark Lonergan	Chairperson
James Hutchison	Advisor
David Tyler	Core Member
Catherine Page	Core Member
Raghuveer Parthasarathy	Institutional Representative

and

Kimberly Espy	Vice President for Research & Innovation/Dean of the Graduate School

Official approval signatures are on file with the University of Oregon Graduate School

Degree awarded September 2013

DISSERTATION ABSTRACT

Patrick Michael Haben

Doctor of Philosophy

Department of Chemistry

September 2013

Title: Controlling the Synthesis of Bunte Salt Stabilized Gold Nanoparticles Using a Microreactor Platform in Concert with Small Angle X-ray Scattering Analysis

Gold nanoparticles (AuNPs) have garnered considerable attention for their interesting size-dependent properties. These properties have fueled applications that span a continuum ranging from simple to sophisticated. Applications for these materials have grown more complex as syntheses for these materials have improved. For simple applications, current synthetic processes are sufficient. However, development of syntheses that generate well-defined particle sizes with specifically tailored surface functionalities is an on-going challenge for chemists. The aim of this dissertation is to improve upon current AuNP syntheses to produce sophisticated materials needed to discover new material properties and provide efficient access to materials to develop new advanced applications.

The research described in this dissertation improves upon current methods for AuNP production by using a microreactor to provide enhanced mixing and synthetic control and small angle X-ray scattering (SAXS) as a precise, rapid, solution-based method for size distribution determination. Using four ligand-stabilized AuNP samples as reference materials, SAXS analysis was compared to traditional microscopic size determination. SAXS analysis provided similar average diameters while avoiding deposition artifacts, probing a larger number of particles, and reducing analysis time.

Next, the limits of SAXS size analysis were evaluated, focusing on identifying multiple distributions in solution. Utilizing binary and ternary mixtures of well-defined AuNP reference samples, SAXS analysis was shown to be effective at identifying multiple distributions. While microscopy has limited ability to differentiate these modes, SAXS analysis is more rapid and introduces less researcher bias.

Because AuNP size and ligand functionality are interdependent, accessing desired core sizes with varied functionality is challenging. To address this, a new microfluidic synthetic method was developed to produce thiolate-passivated AuNPs with targeted core sizes from 1.5 - 12 nm with tailored functionality. This ability to control size while independently varying surface functionality is unprecedented.

Lastly, AuNP core formation was probed by simultaneous *in situ* SAXS and UV/visible spectroscopy. A coalescence mechanism for AuNP growth was observed when using Bunte salt ligands. This finding compares well to observed coalescence in other systems using weakly-passivating ligands and supports the hypothesis that Bunte salts passivate ionically during particle growth while resulting in covalent linkages.

CURRICULUM VITAE

NAME OF AUTHOR: Patrick Michael Haben

GRADUATE AND UNDERGRADUATE SCHOOLS ATTENDED:

University of Oregon, Eugene, OR
University of Idaho, Moscow, ID

DEGREES AWARDED:

Doctor of Philosophy, 2013, University of Oregon
Master of Science, 2008, University of Oregon
Bachelor of Science, 2006, University of Idaho

AREAS OF SPECIAL INTEREST:

Nanoparticle Synthesis and Characterization
Microfluidics
Small Angle X-ray Scattering Analysis

PROFESSIONAL EXPERIENCE:

Graduate Research Assistant, Department of Chemistry, University of Oregon, Eugene, Oregon, 2006-2013

Graduate Teaching Assistant, Department of Chemistry, University of Oregon, Eugene, Oregon, 2006-2007

Undergraduate Research Assistant, Department of Chemistry, University of Idaho, Moscow, Idaho, 2003-2005

PUBLICATIONS:

Haben, P.M.; Elliott III, E.W.; Hutchison, J.E. *Nano Lett.* Submitted for publication

Haben, P.M.; McKenzie, L.C.; Kevan, S.D.; Hutchison, J.E. *J. Phys. Chem. C* **2010**, *114*, 50, 22055-22063

ACKNOWLEDGEMENTS

To all my friends and family who are too numerous to name here: you guys are the greatest. Insert more sappy sentiments here.

This dissertation is dedicated to the cooking of Adam Shiroma, which may have prevented the early onset of type II diabetes during my undergraduate years.

TABLE OF CONTENTS

Chapter Page

Chapter Page

LIST OF FIGURES

LIST OF TABLES

Table Page

CHAPTER I

STUDYING GOLD NANOPARTICLES FROM THE PERSPECTIVE OF A SYNTHETIC CHEMIST

Introduction

Over the past few decades, colloidal nanoparticles (NPs) have garnered considerable attention for their interesting and useful size-dependent properties (i.e.; optical, catalytic, cell localization).[1-5] Most simply, a nanoparticle is defined as a spheroid of material with a diameter < 100 nm. Applications for these materials have grown more complex as syntheses and understanding of these materials have improved over centuries. One of the earliest examples of nanoparticle use is the Lycurgus cup from 4th century Rome, where gold nanoparticles (AuNPs) were incorporated into glass to create a dichroic effect.[6] This made the glass appear white in bright, reflective light and deep red in low lighting. Early applications for nanoparticles focused on physical properties that have little dependence on particle size and polydispersity.

While all nanoparticles are comprised of a core (usually inorganic) and stabilized with a passivant, the various applications for NPs exist on a continuum ranging from simple to sophisticated. Applications at the simple end of this spectrum require little control over nanoparticle physical properties while sophisticated applications require precise control over both particle size distribution and external functionality (Figure 1). Simple applications such as hydrophobic coatings[7] and light-scattering paint pigments[8] take advantage of physical properties of the materials that do not have a strong size-

dependence across large range of sizes (e.g.; hydrophobicity, refractive index) and do not require a specific surface coating on the nanoparticles. More sophisticated applications like selective catalysis[1,9,10] take advantage of highly core size-dependent properties, while not requiring any specific surface functionality. Other sophisticated applications like patterning and annealing films requires a high degree of control over the surface functionality, but little control over the core size.[11] The most sophisticated applications like nanotherapeutics,[12,13] harness both size-dependent core properties and require precise control over the surface functionality.

For simple applications, current synthetic processes are sufficient. Kilogram quantities of material can be synthesized, and polydispersity in the particle distribution is not problematic because the physical properties of interest are easily identified and do not vary strongly across a range of NP sizes.[8,14] Thus, there is little incentive for researchers to seek a higher degree of control over these particles.

In contrast to NPs intended for simple applications, appropriate processes to synthesize NPs intended for advanced applications have been much more difficult to develop for consumer production.[12] For these NPs, the development of efficient syntheses has lagged behind the development of potential applications largely due to the need for much tighter control over NP properties used in advanced applications.[15] For applications like theranostic agents that combine imaging and therapeutic ability, the NP size distribution and the relative ratios of the active ligands must be tightly controlled to achieve the desired particle localization and surface chemistries.[12,16] Current synthetic methods achieve this control through post-synthetic modification, greatly reducing

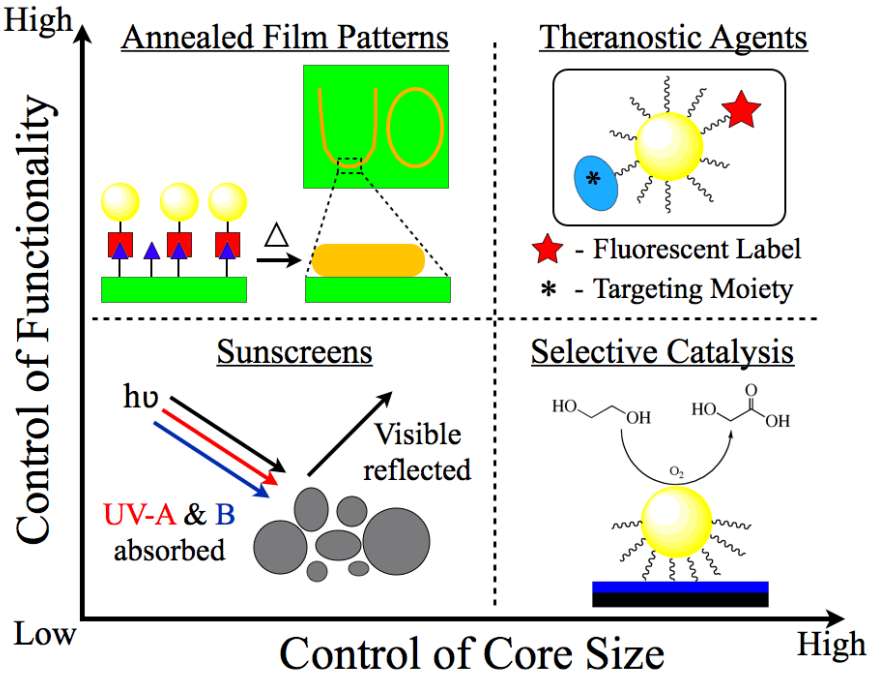

Figure 1. Examples of nanoparticle applications spanning the spectrum of necessary control over core size and surface functionality. Sunscreen applications require little control over core size or external functionality because light absorption characteristics have little dependence on size or surface coating. Selective catalysts show high size dependence, but require bare surfaces, which precludes the need for a high degree of control over surface functionality. Film patterning via annealing nanoparticles requires a high degree of control over ligand functionality to bind the particles in required locations, while core size is of little concern because the particle cores fuse after annealing. The most sophisticated applications, like theranostic agents, require control over both core size and ligand functionality to achieve necessary cellular targeting, sensing, and solubility.

overall throughput and efficiency. This results in difficulties scaling syntheses, achieving reproducibility, and limiting hazard while seeking control over the material properties of interest.[4,12,17]

Au nanoparticles (AuNPs) are a well-studied class of nanomaterials due to the strong size-dependence of their physical properties (especially in the size range d_{CORE} = 1 – 10 nm).[5,18] These NPs are comprised of a Au core, which defines optoelectronic properties, and an organic ligand shell, which defines chemical interactions with the environment. Properties of both the core[5] and ligand shell[19] vary with particle core size. AuNPs are also heavily investigated because gold is toxicologically benign.[20] While the toxicology of colloidal nanoparticles as a whole is not completely understood, current research suggests that the toxicity of these materials arises primarily from the exposed functionality on the surface of the particle and the elemental composition of the inorganic core.[4,20] With this in mind, we can utilize judicious ligand choices with benign Au core material to access products that are both useful and minimally hazardous. Through this responsible development of synthetic processes, we can harness the size-dependent properties of AuNPs to safely access tunable materials for a wide range of applications.

Diverse selections of functionalized AuNPs have been incorporated into many advanced applications and devices, including single-electron transistors,[13,21-23] selective catalysts,[9,21,24-26] plasmonic devices,[21,27,28] colorimetric sensors,[29-31] and therapeutic materials.[12,15,16,32] While many of these applications have been demonstrated with proofs-of-concept, these designs have yet to reach mass-production because of the high cost of AuNP production.[4,12,33] This is largely because current syntheses are inefficient for

producing materials with control over both core size and ligand functionality.[12] To achieve cost-effective materials for advanced applications, researchers need high-throughput synthetic methods that allow reproducible access to AuNPs of desired size and ligand functionality.

The aim of this dissertation is to harness the perspective of a synthetic chemist to improve upon current AuNP syntheses. Using this perspective, the goal of this work is to develop a high-throughput, direct synthesis for AuNPs that enables a high degree of control over core size independent of chemical functionality. These improvements in AuNP synthesis will facilitate the development of current advanced applications into consumer production and provide access to materials to develop new, more sophisticated applications. The remainder of this introduction will focus on the relevant literature for AuNP synthetic methods and mechanistic understanding, focusing on how to use the lessons learned from these studies to improve future syntheses.

Traditional AuNP Syntheses

Researchers have approached the synthesis of functionalized AuNPs with a variety of strategies. Perhaps the most common approach has been to synthesize particles with a well-studied ligand, then perform ligand exchange to introduce a new functionality of interest. This has been effective when the outgoing ligand is weakly-binding (e.g.; citrate), though traces of the initial ligand are typically still observable after exchange.[4] This strategy is less effective when the initial ligand is strongly binding. For example, thiol-for-thiol exchanges can require multiple days to reach completion and are often incomplete,

leaving multiple functionalities bound to the particles.[34,35] Purification of these materials typically requires copious washes, which increases solvent usage, decreases yield, and decreases throughput, all of which result in higher production cost.[4,12] This strategy can be thought of as a brute-force method for AuNP functionalization.

More efficient methods for producing functionalized AuNPs access desired core sizes and surface coatings through a direct synthesis. This strategy dramatically improves overall efficiency compared to ligand exchange methods, but requires a more thorough understanding of the reaction chemistry. Due to the strong interdependence of ligand identity and particle core size trends must be identified to define this relationship. The vast majority of syntheses following this strategy utilize a variation in ligand : Au ratio to achieve size control.[5] The drawback to this approach is that the trend of particle size vs. ligand : Au ratio varies for each ligand. Thus, there is a trade-off in time investment required between direct synthetic approaches and ligand exchange approaches. More initial experiments are required to understand chemical relationships for the direct synthetic approach, while more post-synthetic procedures are required for the ligand exchange approach.

The ideal scenario would be a direct synthesis where size control and functionality control were decoupled, where both variables could be tuned separately. While this ideal has not yet been realized, we can study the current state of AuNP synthetic methods to identify which aspects must be improved upon to access a more ideal synthetic approach. The following section summarizes literature methods for the synthesis of AuNPs with tunable core size and variable functionality.

Turkevich Preparation

The first AuNP preparation that demonstrated the ability to access a range of sizes was the Turkevich preparation,[36] published in 1951, where $HAuCl_4$ is reduced and passivated by sodium citrate while at elevated temperatures.[37] The original procedure claimed that particles ranging from 20 – 150 nm in diameter could be synthesized this way, though a clear trend of size control was not demonstrated. In a 1973 publication by Frens[38] it was shown that AuNP size could be reproducibly controlled by adjusting the amount of citrate introduced to the system.

Numerous researchers have built upon the pioneering work of Turkevich and Frens to further develop the synthesis of citrate-stabilized AuNPs and to understand the underlying mechanisms of AuNP formation in this system.[39-44] Efforts to explain the mechanistic pathway in this system continued over the next few decades with mixed results. Some researchers argued that the reaction proceeded through a chain-like growth pathway[45] while others suggested that discrete nucleation, growth, and ripening were occurring.[40] While it was clear that citrate was acting as both the reducing agent and the ionic passivant in this system, the role pH played in this system wasn't fully understood.

Citrate's role in pH modulation was not well understood until the work of Ji et al. in 2007.[46] The authors showed that citrate concentration affects the pH of the system, which in turn affects the reduction potential of aqueous $HAuCl_4$ to produce different sizes of AuNPs (see Chapter III for more detail on this reactivity). Depending on pH, AuNP formation proceeds either though chain-like aggregates that break apart and form

spheres, or through a nucleation-and-growth pathway. It is notable that Ji et al. also showed a high degree of size control with their increased understanding of AuNP formation in the Turkevich preparation.

The primary advantage of the Turkevich preparation is the wide range of core sizes available through control over ligand : Au ratio. In addition, this is an aqueous synthesis with relatively benign reagents. The most prominent disadvantage to this synthesis is the need for post-synthetic ligand exchange to achieve discrete ligand functionality.[4,5,21] Citrate-stabilized AuNPs are not considered to be functionalized particles because of their weak, ionic multilayer passivation. The necessity for ligand exchange not only results in some amount of citrate remaining in the ligand shell,[4,47] but this post-synthetic processing is also undesirable because it is low-throughput and cannot be scaled up easily for an industrial process.[12]

Two-phase Brust Preparation

The two-phase Brust preparation (also known as the Brust-Schiffrin method) was first developed in 1994 to synthesize functionalized AuNPs in a single reaction step.[48] This synthesis involves a water-toluene mixture where $HAuCl_4$ is dissolved in the aqueous layer, then transferred to the organic layer by complexation with tetraoctylammonium bromide (TOAB), a phase transfer catalyst. Subsequently, a desired thiol (originally dodecanethiol) is added to the organic layer and $NaBH_4$ is slowly added to the aqueous layer to induce particle formation at the organic-aqueous interface. By altering the ligand : Au ratio, AuNPs ranging from 2 – 8 nm can be accessed. A variety of

hydrophobic ligands have been utilized in this synthesis, though typically alkanethiols are used.[49,50]

This synthesis is advantageous because it allowed access to various functionalized particles with tunable size in one synthetic step. The ability to intentionally alter particle size and terminal functionality are two of the key components to an ideal nanoparticle synthesis. Additionally, the small core sizes available have been shown to be interesting for a variety of AuNP applications, and a high percentage of Au surface area is exposed to solution.[5,9,18] The utility of this approach is evident when one reviews the vast amount of literature based upon the two-phase Brust preparation or modifications thereof.

There are, however, some drawbacks to the two-phase Brust preparation. First, this method only produces organic-soluble AuNPs. Other methods must be pursued to produce water-soluble AuNPs. Second, the presence of TOAB is problematic because it is highly persistent in the ligand shells of AuNPs.[4] This is important because TOAB can disrupt the ligand functionality on the particle surface and because TOAB is cytotoxic.[4,51] Therefore, removal of this molecule is of paramount importance for biological and toxicological applications. Considerable solvent washes must be performed to remove TOAB from the particles, greatly reducing the solvent and time efficiency of this process.[4,12] Thus, while the 2-phase Brust preparation made for significant progress in AuNP syntheses, other methods were needed to access materials for aqueous (e.g.; biomedical) applications.

Single-phase Brust Preparation

In 1995 Brust et al.[52] published a single phase, methanolic adaptation to the two-phase Brust preparation of AuNPs. This synthesis represents a simpler, more efficient process than the biphasic counterpart, and has been since adapted for aqueous conditions to access hydrophilic functionalities.[53,54] An example of a modified single-phase Brust prep was shown by Briñas et al.[55] in 2008, where glutathione-passivated AuNPs were produced. The authors show one of the few examples of controllable particle size in a direct AuNP synthesis using thiols. AuNPs from 2 – 6 nm in diameter were obtained by varying the reaction pH from 8 - 5.5.

The size trend by Briñas et al., however, has large error associated with each data point (as much as +/- 1 nm) making it difficult to achieve a desired size reproducibly. Aside from the large errors, a number of the data points deviate significantly from the trend, further complicating efforts to obtain specific sizes of AuNPs. This method is advantageous because it enables direct, aqueous synthesis of size-tunable, functionalized AuNPs. Disadvantages to this approach include a small range of sizes and a lack of precision in size control.

Murray Bunte Salt Preparations

The Murray group published two papers in 2000[56] and 2001[57] using thiosulfates (Bunte Salts) as ligands in a modified single-phase Brust preparation to synthesize AuNPs. These papers each present one ligand and one particle size, but they show that AuNPs synthesized with these ligands are indistinguishable in composition from particles

made with analogous thiols. This makes Bunte Salts very attractive ligands, because, unlike thiols, they do not form disulfides in solution, and a wide variety of water-soluble functionalities are accessible through simple syntheses with few synthetic steps. Thus, this approach is advantageous because it utilizes versatile ligands in a direct, aqueous synthesis with benign reagents. The major drawback to this approach is a lack of understanding of chemical relationships necessary to control core size.

Hutchison Bunte Salt Preparation

After Murray et al. demonstrated that thiolate-passivated AuNPs could be synthesized using Bunte Salts, the Hutchison lab began investigating this as a route to generating versatile AuNP functionalities. Lohse et al.[47] demonstrated that a wide range of AuNP sizes ($d_{CORE} \sim 2 – 20$ nm) and functionalities were available with this method. This synthetic approach is promising because of the wide range of core sizes and functionalities available. However, the synthesis suffered from high polydispersities and no single variable provided precise control of particle core size.

Considerable work has been done working toward direct syntheses of size-controlled, functionalized AuNPs (Figure 2). However, barriers to producing these desired materials still exist: poor reproducibility, low throughput, low yield, and limited range of core sizes. Target attributes for an ideal AuNP synthesis include highly reproducible particle size distributions, high throughput of synthesis and analysis, high initial yields, and precise control over both average core size and external functionality. The following

section reviews literature formation mechanisms to enact practical improvements to direct AuNP syntheses.

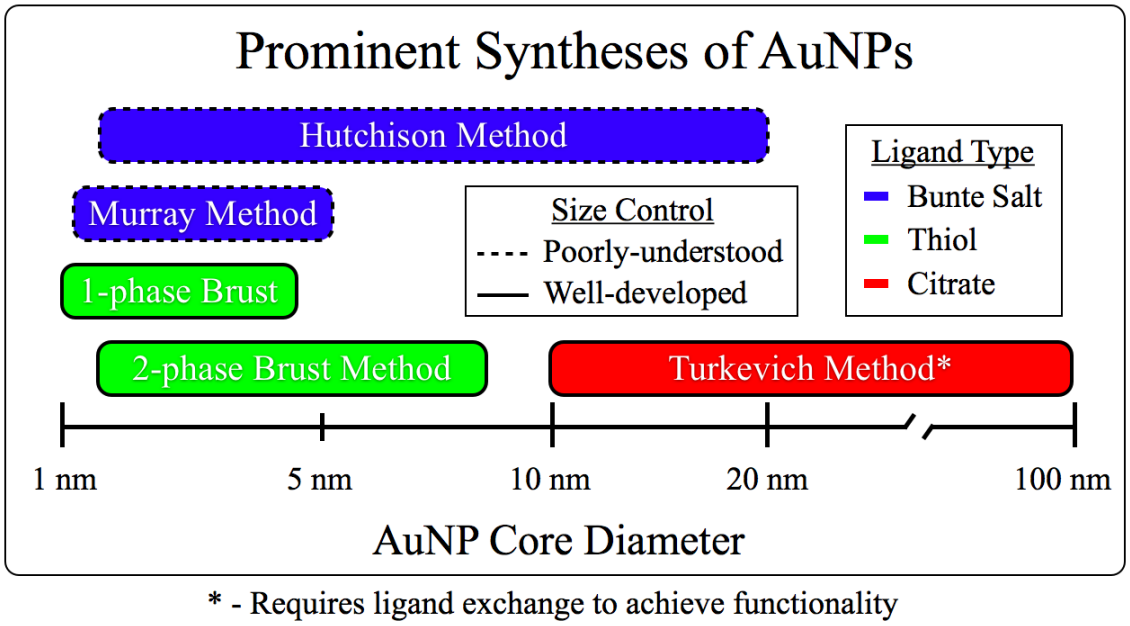

Figure 2. Summary of direct synthetic routes to size-tunable AuNPs. The Turkevich method accesses a large range of AuNP sizes, but particles must be post-synthetically functionalized. Brust methods utilize functional thiol ligands, but 2-phase method uses deleterious TOAB phase-transfer catalyst and 1-phase method accesses limited size range. Murray and Lohse methods use Bunte Salts to access larger range of functional materials, but trends to control size are still poorly understood.

AuNP Formation Mechanisms

The study of AuNP formation mechanism has been challenging because of the complexity of the materials and due to overlapping mechanistic processes. The drive to understand these mechanistic processes, however, is closely tied to attempts to improve current synthetic methods. A prime example is in CdSe nanocrystal systems where nucleation and growth have been separated temporally using a microreactor.[58,59] Probing the optimal duration of nucleation enabled researchers to induce particle formation by heating the precursor solution for specific durations, then reduce the temperature to prevent further nucleation and facilitate growth processes.[60] Understanding which mechanisms are relevant to a particular system directly aids in the improvement in that system, and provides researchers with areas of focus when optimizing reaction conditions. This section summarizes common nanoparticle reaction processes and then describes more detailed AuNP formation mechanisms.

Nanoparticle Reaction Processes

Nucleation. Nucleation (Figure 3) is the process through which particles are initially formed. Comparison of total surface energy and bulk energy for a given particle dictates that a critical nucleation size exists.[61] Below this size, particles exist in equilibrium with molecular species and can re-dissolve when formed. A certain probability exists that the particle will grow to exceed this critical nucleation size. Above the critical nucleation size, the bulk energy gained from bonds in the particle core overtakes the loss of surface energy and it becomes favorable for particles to grow larger.

Growth. The growth phase involves the incorporation of molecular monomeric species into growing nanoparticle cores. This process could potentially be either diffusion-limited or reaction-limited, depending on how strongly the monomeric species interact with the growing particle core.[62] Once the growth process begins, it will continue until the reservoir of growth monomer is depleted. It is typically assumed that these growth monomers are single molecules or ionic complexes of core material (e.g., $HAuCl_4$), but it is possible that small clusters of a few bound atoms could exist as growth monomer species.

Coalescence. Coalescence is the process during nanoparticle formation where weakly passivated nanoparticle cores fuse to form larger particles.[63] This process is more likely when weak or ionic ligands are used. A hallmark of this process is a drop in particle concentration as core size increases.

Ripening. This process typically occurs at long reaction times, after nanoparticles have formed and been passivated.[64,65] If ligand passivation is sufficiently weak (eg., citrate), material can escape the particle core and diffuse away from the particle. Studies of ligand exchange suggest that association of a ligand species to molecular core material is required for these species to escape the particle in this fashion.[66] To minimize surface energy, the ligand-associated material transfers from small particles to large particles, first creating a bimodal size distribution and eventually leading to a larger monomodal distribution of particles.

Aggregation. Aggregation is considered to occur when passivated particles in solution come into close contact and the cores become bound irreversibly.[67] The cores are

often observed to fuse completely, forming irregular shapes or necks between individual particles. Aggregation is almost always considered undesirable, as it is very difficult to control and drastically alters the size-dependent properties of the initial particle size distribution. This process should not be confused with sintering, which is a process observed on solid supports where bare particles at elevated temperatures fuse completely.

Agglomeration. Agglomeration is a process similar to aggregation, but where the particle cores remain distinct and partially separated.[68] This usually involves a significant interaction between neighboring ligand shells where the particles are strongly attracted, but the cores are still observably distinct.

AuNP Formation Theories

Classical Nucleation Theory. The most commonly cited theory for colloidal AuNP growth is the LaMer mechanism, also known as classical nucleation theory (CNT). This theory was first applied to colloids by LaMer and Dinegar[69] to describe the precipitation of sulfur colloids from solution. The theory described in this paper involves the buildup of a reactive species (molecular sulfur, S_2) in solution over time. During this period, the concentration is too low to nucleate particles. This is referred to as an incubation period. As the concentration continues to increase past the saturation point into supersaturation, particles of sulfur spontaneously nucleate (also referred to as burst nucleation), rapidly consuming the reactive species. The initial concentration of sulfur species dictates the length of time over which nucleation can occur, where higher

concentrations will result in a longer nucleation period and vice versa. The ideal scenario to generate monodisperse particles is a short nucleation period, where a quick burst of nucleation occurs, quickly ceases, and subsequent growth of the nuclei then occurs. These

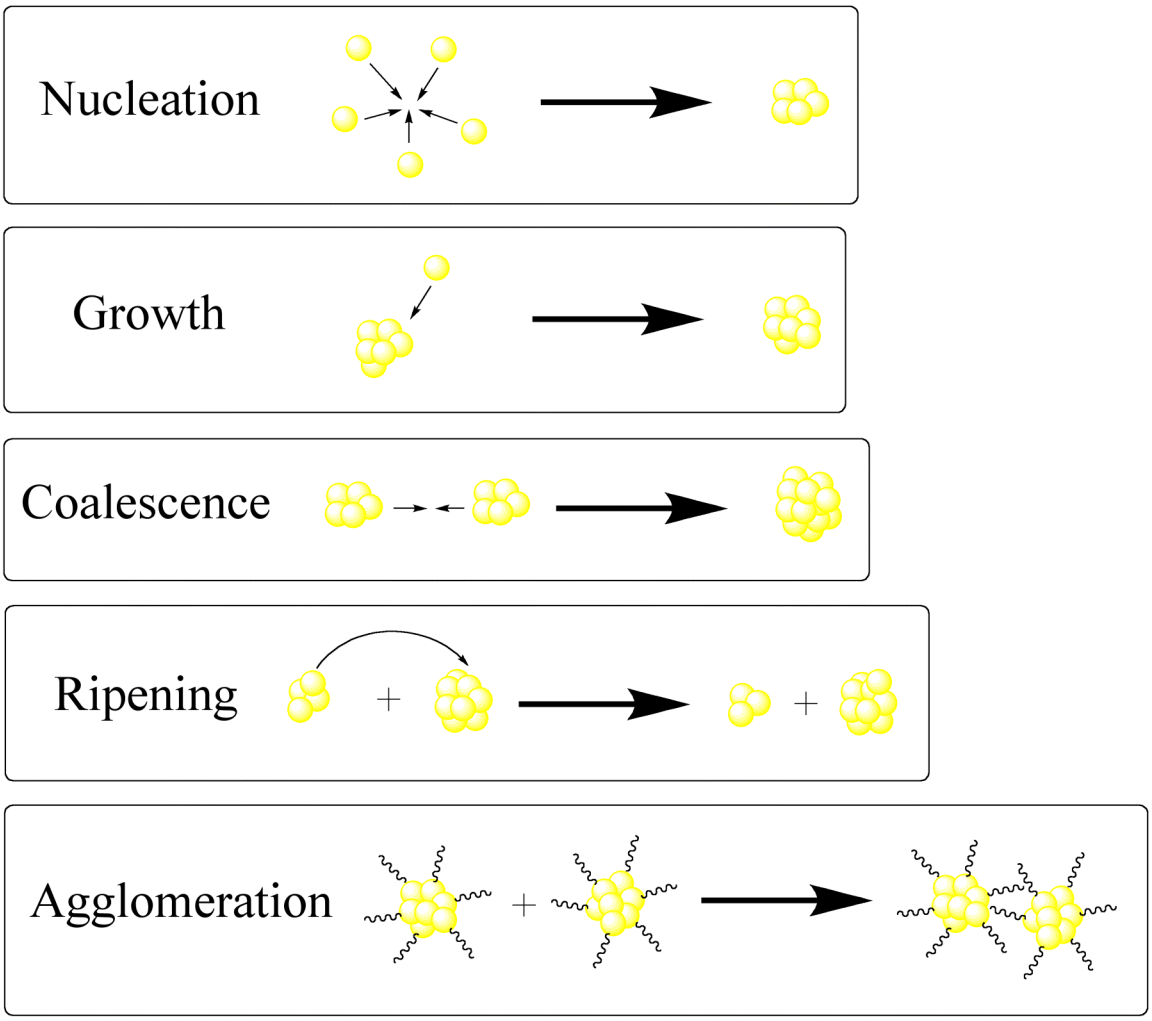

Figure 3. Summary of relevant mechanistic processes for AuNP systems. In addition to those shown here, Aggregation can be thought of as coalescence where the particles become insoluble and precipitate.

growing nuclei can continue to incorporate reactive S_2 into the colloid even after the concentration of reactive species drops below the saturation level. At this point the critical nucleation energy has been surpassed, meaning that it is thermodynamically favorable to minimize the surface area of sulfur exposed to solution. This is described as the growth phase. Growth continues until the reactive monomer species is depleted.

While LaMer's original work was limited to studying sulfur sols, Sugimoto[62] was the first to adapt CNT to describe inorganic nanoparticle formation. In this work, the focus was on obtaining monodisperse colloids through temporal separation of nucleation and growth phases, and subsequently inhibiting coagulation of particles through the use of various passivating agents. Sugimoto goes into great detail discussing diffusion-controlled reactivity versus reaction-controlled reactivity and a variety of other inorganic nanoparticle systems. This work inspired many other researchers to consider nanoparticle reactions as a combination of nucleation, growth, and coagulation processes, and provided some useful mechanistic insight for improvement to existing syntheses.

CNT suggests that the key to obtaining monodisperse AuNPs is to maintain a short nucleation phase while keeping the growth phase temporally distinct. This strategy has been effectively employed for the synthesis of CdSe nanocrystals in microreactors where nucleation in initiated in a region of increased heat, then growth is allowed to continue at reduced temperatures, once the critical nucleation size has been exceeded.[58,59] Further, CNT suggests that passivating agents must interact with the core material with rapid kinetics to prevent coagulation as the particles are growing. Thus, for AuNP

systems, thiolate ligands have been a common choice of passivant due to their strong interaction with Au.

While CNT provides some useful mechanistic hypotheses, there are shortcomings in the ability to describe NP systems. CNT assumes that the nucleation process is solubility-driven, meaning that some reactive species must accumulate in solution past saturation to induce nucleation. This is an effective description of sulfur sol behavior, but a different material may not require supersaturation if bond formation is more energetically favorable. In the case of AuNPs, it's well known that Au has a high self-affinity, where aurophilic bonding strength is roughly on the order of hydrogen bonding.[70,71] Thus, we would expect very rapid formation of NPs in this system where Au-Au bond formation is highly favorable. This rapid particle formation has been confirmed experimentally.[72,73] In cases with rapid reduction, there is often no evidence of an incubation period, suggesting that supersaturation is not required to form particles in these systems. Thus, while CNT does offer insight toward achieving monodisperse, passivated particles in certain systems, it does not completely describe formation and growth of functionalized AuNPs.

Dispersive Kinetic Theory of Nucleation. Skrdla highlights the shortcomings of CNT in his paper as reason to utilize a dispersive kinetic model of NP nucleation.[74] Therein, the author points out that CNT assumes only one critical nucleation size exists (corresponding to a unique nucleation/activation energy) for a given set of reaction conditions. However, as the reactants are depleted from solution, the changes in reaction conditions cause variation in the critical nucleation size. This approach presents a method

for determining the varied critical nucleation size at different stages of reactant depletion. The overall goal in developing this approach is to more accurately describe the kinetics of nucleation.

This model is attractive in its ability to explain polydispersity in a AuNP sample due to variable nucleation conditions. However, this approach has been criticized for using empirical fitting parameters that have little physical meaning. Further, this model doesn't offer much additional insight into synthetic design as the theory suggests that, like CNT, the nucleation phase should be a short as possible to achieve monodisperse particles.

Ostwald Ripening. There are a number of mathematical treatments for Ostwald ripening in the literature, though Lifshitz-Slyozov-Wagner (LSW) Theory is most commonly cited.[75] Ostwald ripening is a well-understood phenomenon where core material transfers from small NPs to large NPs in order to minimize surface energy. Thus, LSW theory is comprised of diffusion rates for molecular species and various sizes of NPs with the minimization of particle surface area as the driving force.

Ostwald ripening has been observed for citrate-stabilized AuNPs and other particles with weak surface passivation that facilitate material transfer to and from the gold cores.[40,41] This ripening is typically a slow process relative to particle nucleation and growth, and is thus observed at long reaction times in AuNP systems. In the case of citrate particles, the AuNPs are often stirred at elevated temperatures after particle formation to enable Ostwald ripening, because this causes the particle distribution to focus, becoming less polydisperse over time. The average AuNP size also increases during

the process. While this is a convenient process for AuNP systems with weakly bound or ionic ligand shells, strongly binding ligands prevent material transfer to and from the NP cores. Thus, direct AuNP preparations using thiols, or other covalently binding ligands preclude Ostwald ripening from occurring, and therefore this process need not be considered under these synthetic conditions.

Coalescence Models. While ripening involves the molecular transfer of material, coalescence is the process of two or more NP cores fusing to become one larger NP. A model that was originally developed by Avrami to describe grain coarsening in a solid has been adapted in a variety of ways to mathematically explain coalescence of particles in solution.[76-78] This is inherently problematic, because in Avrami's original model there is no consideration of solvent or diffusion of growing nuclei. Only the original crystalline material, growing grain nuclei, and final coarsened crystalline phases are included in the model. Researchers have tried to utilize this model for colloidal systems because the mathematical treatment of nucleation and growth are attractive, but the base assumptions in the model are not sufficient to describe AuNP growth in solution.[79] In general, it can be assumed that coalescence only occurs when particles are weakly passivated during growth. Attention should be paid to the nanoparticle concentration during growth to assess whether this process is active.

Four-step Double-autocatalytic Mechanism. This theory, developed by Finke et al.,[80] was developed to explain growth of a variety of catalytic inorganic clusters. The general mechanism is based on four distinct chemical steps, two of which are autocatlytic. This kinetic model is fitted to cyclohexene reduction data, treated as an indirect

measurement of catalyst formation. This model has been cited in the literature for its ability to fit sigmoidal kinetic curves,[81] but has been criticized as being overly complex.[82] Further, it was suggested that a mechanism with four chemical steps having similar rates to the rate-limiting step is highly improbable. Finke et al. argue that 4 unique rates are the minimum required to fit their data.[83]

It is interesting that Finke et al. were able to gain kinetic insight into their system by monitoring the formation of the Pt catalyst via hydrogenation of cyclohexene. This type of indirect study can be used to cleverly monitor other nanoparticle systems, but care must be taken to consider other variables that may affect the hydrogenation. However, this model has been effective as modeling sigmoidal kinetics and can be considered when autocatalytic reactivity is possible.

A number of consistent themes arise throughout AuNP mechanism literature. First, the active mechanisms in AuNP systems can vary depending on the ligand used. This is a major challenge for studying these materials, because similar systems can follow drastically different pathways. However, all nanoparticle reactions must have some nucleation phase to begin particle growth. There is mounting evidence that this is the most important stage of nanoparticle formation, as polydispersity introduced early in the reaction can be carried throughout the reaction.[73]

It is clear that AuNP reactions are very rapid,[72,73] and more rapid mixing is required to achieve consistent conditions over multiple syntheses.[84,85] Comparing current synthetic methods to literature using applied nanomaterials, it is also clear that more high-throughput, cost-effective methods are needed to produce large quantities of AuNPs with

tunable sizes and variable functionality.[4,12] Focus should be directed on covalently bound ligand shells that present specific desired moieties to the local environment around the nanoparticle to access the desired material properties.

Overall, traditional synthetic methods are not sufficient to achieve the necessary level of control over many nanomaterial preparations. Batch reactions do not allow researchers the ability to control mixing rates or reagent addition rates precisely enough.[86] New synthetic platforms along with new AuNP preparations are necessary to obtain control over these complex materials and to generate well-defined products with desired properties.

Microreactors as a Synthetic Platform for Nanomaterial Production

Because of the complex nature of nanoparticle syntheses, traditional batch methods are insufficient to achieve control over these reactions.[86] New synthetic platforms are needed that have fast mixing times, precise reagent addition times, and the ability to implement in-line observation or synthetic manipulation (e.g., heating, microwave exposure) at specific reaction times.[58,59] Microreactor platforms (defined for this work as having channel diameters of < 1 mm) offer three broad benefits over traditional batch reactions: (1) the potential to obtain more well-controlled nanomaterials with improved throughput, (2) rapid methods development, and (3) flow-based *in situ* characterization.[86,87]

Microfluidic synthetic platforms offer the potential to access improved nanomaterial properties over batch reactions because of more reproducible synthetic

conditions (i.e.; mixing rates, reagent addition rates) and rapid reagent mixing. Reproducible reaction conditions provide obvious benefits from synthesis-to-synthesis,[60] and there are multiple advantages of rapid mixing. Since many nanoparticle reactions occur on fast time scales, with observable particle sizes as early as 75 μs,[88] rapid mixing is necessary to achieve homogeneous conditions during relevant stage of particle growth. In addition, it has been shown that product distributions are more monodisperse when synthesized under the more homogeneous conditions presented by microfluidic systems.[87,89,90] Polydispersity is still present to some degree because reaction times can still be more rapid than the fast mixing times in a microreactor.[88] It should also be noted that mixing rate in microreactors has been utilized as a reaction parameter. At varied flow rates, different sizes of particles are produced for certain reactions.[89,91] Though some increase in polydispersity may be observed in cases of slower flow rates, using mixing rate as an additional reaction parameter can be a useful way to tune product distributions. Overall, the rapid mixing observed in flow provides the potential for more reproducible nanoparticle syntheses with improved material propreties.

Another distinct advantage of a microreactor platform over traditional batch syntheses is the potential for scale-up.[4,92,93] Batch reaction volumes cannot always be increased without altering NP product distributions, making scale-up challenging. Microreactors, however, can be run continuously with a peristaltic pump to produce material continuously.[13,93] In addition, microreactors can be run in parallel to multiply the reaction throughput.[4,92,94]

It is important to note that a variety of microreactor platforms exist with drastically different throughput. The smallest scale, on-chip, microreactors utilize small volumes and, thus, low total flow rates. These reactors exhibit the best control over mixing, but reaction throughput is low and the necessary components are relatively expensive, requiring etching or lithographic techniques to produce the very small reactor channels. Larger-scale microreactors sacrifice some control over mixing rates to access higher reaction throughput at lower cost. These reactors utilize polymer tubing and simple T-mixers instead of prefabricated chips to combine reagents in flow. These components can be readily purchased at low cost. Overall, the versatility in microreactor technology means that different systems can be assembled for unique needs. If an industrial lab requires precisely made materials, small chip-based reactors can be assembled in parallel. Conversely, an academic lab pursuing reaction optimization or fundamental studies can utilize a larger-scale reactor to perform larger numbers of syntheses and generate more material. Thus, the range of potential designs for microreactors makes these versatile synthetic platforms for a variety of research needs.

Another advantage microfluidic platforms offer is the ability to perform in-line characterization. A unique aspect of microreactor technology is the steady-state conditions at each point along the length of the reactor.[95,96] Though the solution is continuously flowing, each point after mixing along the reactor length corresponds to a specific reaction time. Additional input streams can be added at specific locations in the flow path to introduce reagents at precise reaction times.[91] Further, if a reaction requires heating, exposure to microwaves, or another external treatment, this can be done over

specified durations in the reactor.[58,92] The continuum of sequential steady-states along the microreactor enables a wide variety of advanced reaction geometries. This enables researchers to achieve product distributions with a high degree of control and tunability.

The unique steady-state conditions in a microreactor facilitate incorporation of an observation cell at any point to observe a specific reaction time for extended durations.[92,96] These types of reactors are highly valuable for mechanistic studies, as the observation cell can be utilized to observe which products or intermediates are present at various reaction times.[73,95] A variety of studies have been performed where particle sizes are observed over time and a general growth mechanism can be inferred.[72,73,81,88,92,95,97,98] Incorporating different *in situ* techniques in this way accesses a comprehensive, time-resolved picture of reactivity. This is a powerful way to monitor reactions and allows researchers to elucidate more detailed NP reaction mechanisms.

Despite the range of advantages, microreactors do not always add significant value to a given system (Figure 4). For example, slow reactions do not require fast mixing and the 10-15 sec mixing times in a batch reaction are sufficient. However, very fast reactions show significant benefits from microfluidic synthesis because mixing occurs on the same time scale as the reaction. Mixing in batch conditions is much slower than reactivity in these cases. AuNP reactions benefit greatly from microfluidic synthesis because nucleation occurs on the order of milliseconds,[73,88] which necessitates rapid mixing. Further, improvements to polydispersity are observed because the increased homogeneity of reaction conditions limits the formation of byproducts.[86] Thus, while microreactors do

not necessarily result in significant benefits to every synthetic system, the rapidity of reactivity in AuNP systems makes the use of microreactor platforms highly beneficial.

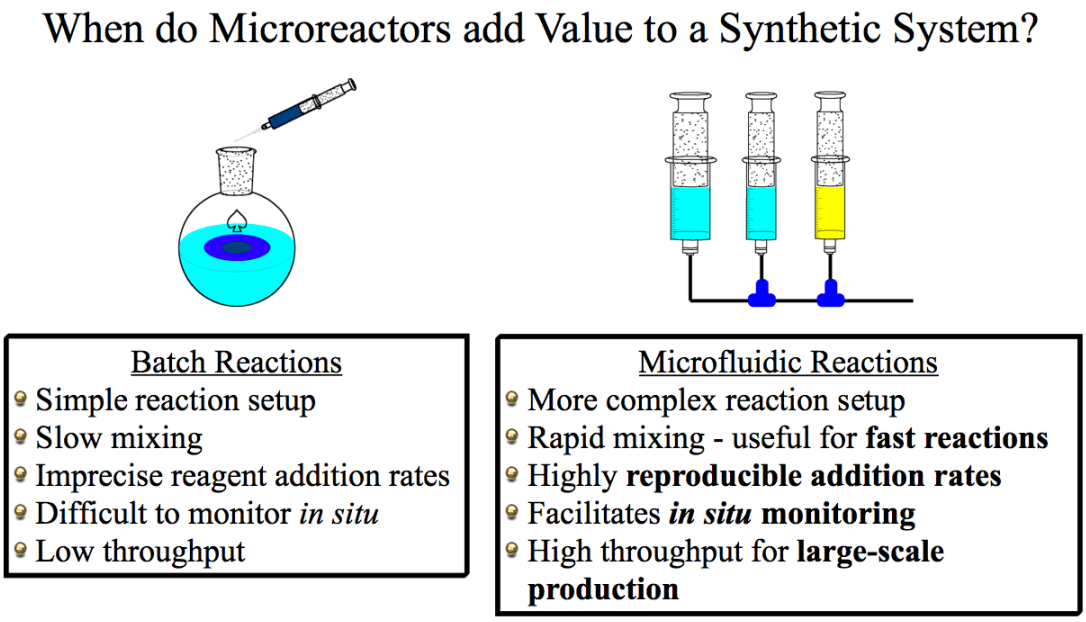

Figure 4. Summary of the scenarios when microreactors add value to a synthetic system. Simple batch reactions are sufficient for many systems, especially when reaction rates are slow. When reaction rates a fast, however, slow mixing in the batch reaction can lead to a range of products. More rapid mixing in a microreactor results in more homogeneous products for these reactions. In addition, highly reproducible addition rates are beneficial for these fast reactions. Further, the steady-state conditions in a microreactor facilitate *in situ* monitoring. Lastly, microreactors can be run with peristaltic pumps and in parallel to achieve large-scale production if large quantities of material are needed.

Microreactors represent the next generation of nanomaterial synthetic methods for rapid, complex reactions, in addition to enabling *in situ* observation. Now

researchers must develop methods to match the throughput of characterization with the high throughput of synthesis. The so-called characterization bottleneck has been a major factor in limiting the incorporation of NPs into commercial products, since materials must be thoroughly vetted before passing regulatory hurdles.[99] It can require days to completely characterize a new nanomaterial, while organic chemists can analyze their products within minutes using NMR techniques. Materials scientists must pursue new characterization strategies to minimize time of analysis and maximize overall throughput of material generation if they are to make new nanomaterials accessible for commercial products.

Characterization Methods

Characterization is a crucial and challenging aspect of generating new nanomaterials. In contrast to small molecules, where NMR is often sufficient to characterize the product, nanoparticles must be observed with a variety of techniques to fully define the relevant physical properties. Given the complexity of nanomaterials, quantification of the particle core size, polydispersity, concentration, and surface chemistry is needed.[99] When new materials are developed, a comprehensive characterization strategy should be employed, while only a few rapid techniques are necessary once the class of materials has been well-studied. Understanding the necessary level of characterization is an important aspect to minimizing characterization time commitment.

As researchers push the characterization of nanomaterials forward, focus will be directed towards techniques that provide rapid, quantitative feedback of material

properties.[99] These techniques must be used in an integrative, complementary fashion to fully characterize a material quickly. Techniques such as TEM, SAXS, and XPS are often time-consuming, but new automated methods[73,100,101] for collecting and processing data are greatly reducing the time investment required by researchers to obtain these data. Widening the characterization bottleneck will require an increasing use of these automated techniques so that researchers can spend less of their time analyzing current materials and more time developing the next generation of materials.

The characterization methods utilized in this thesis work are described below. Small-angle X-ray scattering (SAXS) and transmission electron microscopy (TEM) were utilized to quantitatively determine AuNP size distributions and morphology, while UV/visible spectroscopy (UV/vis) was used to qualitatively corroborate these data and determine bulk optical properties. X-ray photoelectron spectroscopy (XPS) provided ligand shell composition data while thermogravimetric analysis (TGA) was used to determine particle surface coverage. Nuclear magnetic resonance (NMR) was utilized to determine ligand identity and purity. More detail for each of these characterization methods is provided below.

Transmission Electron Microscopy (TEM)

TEM has traditionally been used as the standard measurement of nanoparticle core size.[15,54] This technique utilizes an electron beam focused on a nanoparticle sample that has been deposited on a substrate.[102] Analysis works best if there is a significant difference in electron density between the nanoparticles and the substrate. A typical

sample might consist of AuNPs deposited on a silica substrate. This substrate is fabricated as a TEM grid, where very thin, electron transparent windows are spaced periodically across a thicker, more robust substrate. In a standard 'bright field' TEM experiment, the beam is focused at one of these windows where incident electrons largely pass through the substrate and the electron-dense nanoparticles absorb or diffract the electron beam, creating what is essentially a shadow or negative exposure at a phosphor screen (for temporary viewing) or CCD detector (for data collection). Note that older TEM instruments may utilize a photographic emulsion to collect data. While all of the data shown in this thesis work are bright field images, note that some of the electrons absorbed by the nanoparticle sample are back-scattered, and can be collected by a second detector to form a dark field image (positive exposure) where the direct beam is excluded.

Once an image is collected, it will contain particle size information for all of the individual nanoparticles that were in the direct electron beam path. If the beam is focused properly, the shadows representing each of the particles will correspond directly to the core size of the particles. With resolution and magnification information, these magnified images are analyzed in a program such as ImageJ or Fiji to determine the size of each of the particles.[103] These collected data are then input into a spreadsheet for more detailed analysis and are typically displayed as a histogram. Data are most often displayed as the average core diameter (in nm) +/- one standard deviation of the distribution width (again in nm). Note that thorough TEM experiments will analyze at least several thousand to several tens-of-thousands of particles to obtain appropriate statistical counts for the sample. This is important because a large component of sample bias can be introduced

when image locations are chosen on a sample TEM grid. In addition, deposition artifacts can skew results, necessitating a large number of particle counts to average out these effects.[96]

Traditionally, the major drawback to TEM analysis has been the large time investment required to collect and process data. The advent of automated TEM has significantly reduced this necessity,[100] though samples must be sufficiently homogenous for this technique to be effective. In addition, liquid cell sample holders are now available for TEM instruments, allowing researchers to view samples under solution phase conditions.[104] These new techniques will ideally allow more TEM measurements to be collected with less researcher time input, mitigating one of the most prominent drawbacks to these analyses.

Small-angle X-ray Scattering (SAXS)

SAXS has historically been confined to use at high-intensity synchrotron X-ray sources,[41,98,105] but has become much more common over the past few years with the advent of lab-scale SAXS technologies.[73,106] For this technique, a solution of nanoparticles is exposed to monochromated X-rays.[107] Based upon the size, shape, and polydispersity of the particles, a varied number of X-ray photons will scatter off of the sample at various angles (~ 0.1° – 10°). The function of scattering intensity vs. scattering vector, q, is characteristic of the sample size distribution.

SAXS is attractive because of its ability to quantitatively determine particle core size, polydispersity, and concentration (utilizing a standard to normalize beam intensity

to the absolute scale) in solution.[107] The ability to collect these data in solution is of particular importance because deposition artifacts often observed in TEM analyses are avoided. In addition, this allows a much larger number of particles – often an increase of 10 orders of magnitude – to be analyzed by SAXS than with TEM measurements. This higher degree of statistical relevance means that SAXS analysis gives much more representative core size and polydispersity information than TEM analysis(see Chapter II).[96] This has resulted in a general trend where researchers are beginning to treat SAXS as a standard nanoparticle size analysis technique over the historical prevalence of TEM.

While SAXS analysis is highly useful for precise core size determination, this technique does have some limitations. SAXS is a model-based technique, meaning that considerable expertise is required to fit models to raw data.[107] As with any model-based technique, there can be ambiguity from the modeled results. Reduced chi-squared values can be used to assess fit quality, but reports in the literature often do not provide any value for model fit quality. A further challenge with SAXS analysis is the accurate determination of error values. Due to the unique nature of individual CCD detectors, challenges of binning CCD pixels, and the complicating factor of polydisperse samples, determined error values are only considered to be estimates. This is a difficult problem to circumvent; therefore the error bars shown in this thesis work were generated by performing analyses of multiple AuNP syntheses to determine the standard deviation between final results. In this manner, real error values between output values of modeled core size and polydispersity values were determined.

It should be noted that SAXS presents the opportunity for high-throughput, automated analysis: a capability that is often unavailable or impractical for TEM analysis. The lab-scale SAXS in the University of Oregon Lokey Labs is equipped with an autosampler, such that dozens of samples can be analyzed in rapid succession without researchers present. This aspect was particularly useful during this dissertation work, enabling rapid optimization of AuNP syntheses and providing the ability to probe a multitude of synthetic variables quickly (see Chapter III).

UV/visible Spectroscopy (UV/vis)

UV/vis is a simple, ubiquitous technique that is particularly useful for AuNP samples.[108] AuNPs have unique, size-dependent optical properties that can be used to estimate core size. Qualitative determination of particle core diameter and concentration is possible based on the relative absorbance at the surface plasmon resonance lambda-max (ranging from ~ 500 nm – 530 nm) and the absorbance at 450 nm.[109,110] Estimation of particle size works well for AuNPs larger than 5 nm in diameter.

In addition to core size and concentration estimations, UV/vis also provides excellent indication of particle stability due to the strong dependence of AuNP optical properties on size and morphology.[4] It is trivial to compare UV/vis spectra at different times to determine if the sample has changed. Additionally, a raised baseline in UV/vis is a telltale sign for particle precipitation. Further, plasmon lambda-max shifts to longer wavelengths (> 550 nm) indicate particle aggregation in solution.[30] Overall, this is a quick and simple method for determining qualitative stability information of AuNPs in solution.

UV/vis has also been useful for determining what molecular precursor species are left in solution. $HAuCl_4$, for example, has a characteristic absorbance at ~315 nm from a Au-Cl LMCT band. Au(I) species, however, have small but distinct absorbance at ~210 nm and ~215 nm. UV/vis is a convenient way to determine if these species are present, and if the AuNP formation reaction has gone to completion. This simple method can be extended to any precursor species having absorbance in the UV/visible range.

X-ray Photoelectron Spectroscopy (XPS)

XPS is considered the standard method for determining the oxidation states of species bound to (or closely associated with) a nanoparticle surface.[15] For this technique, a nanoparticle sample is directly deposited onto a substrate (typically chromium) and dried. Once placed into a vacuum, the sample is then exposed to monochromated X-rays.[102] Upon absorption of X-rays, electrons are ejected from the sample with different energies and collected for analysis. The specific observed energies are characteristic of the element and its oxidation state such that the chemical environment of the adsorbed molecule can be inferred. The penetration depth of XPS is only a few nanometers, making this a surface sensitive technique, and the primary way researchers characterize the bonding environment of nanoparticle ligands.

In this dissertation work the majority of collected XPS data were used to distinguish sulfur oxidation states in AuNP ligand shells. Thiosulfate-terminated ligands have distinct oxidation states from thiols. XPS was utilized to determine what percentage of the thiosulfate ligands had been converted to thiolate ligands.

Thermogravimetric Analysis (TGA)

TGA is a simple technique where a dried sample is placed in a tared pan and exposed to increasing temperature at a defined ramp rate.[5,47,84] The mass of the sample is recorded as a function of temperature. More volatile compounds will vaporize at low temperatures, and vice versa. These experiments are typically run up to temperatures that will vaporize all organic matter, but leave inorganic material. In the case of nanoparticles, the mass lost corresponds to the mass of the ligand shell plus any remaining solvent. The remaining mass corresponds to the inorganic nanoparticle cores. In this work, TGA is used to calculate the AuNP surface coverage of the ligand shell.

Nuclear Magnetic Resonance (NMR)

NMR is a ubiquitous technique for determining the identity of molecular compounds.[5] Molecules bound to nanoparticles still give distinct resonance peaks if the particles are small (< 2 nm), but these are significantly broadened due to the slowed relaxation time they experience and varied chemical environments across the particle. Large particles often show no distinct NMR peaks. Slowed relaxation times are attributed to the effect of being bound to a substrate and not freely diffusing through solution. The majority of the NMR data shown in this work are to characterize ligands before use in synthesis and determine purity.

Dissertation Overview

Chapter I described the relevant background information on gold nanoparticle applications, synthesis, mechanistic studies, and characterization methods. Chapter II was coauthored with Lallie C. McKenzie, Stephen D. Kevan, and James E. Hutchison. This chapter focuses on the use of SAXS to analyze known AuNP samples. Comparisons of four AuNP standards are drawn between SAXS size analysis and TEM size analysis using UV/visible spectroscopy as a bridging technique. Chapter III was coauthored with Edward W. Elliott III and James E. Hutchison. This chapter shows the development of a new synthetic method to target and synthesize 2 – 10 nm AuNPs with a variety of terminal functionalities. SAXS is instrumental in determining the precise, pH-dependent size trends shown in this chapter. Chapter IV utilizes the synthesis developed in the previous chapter to access a direct preparation of ~ 1.5 nm functionalized AuNPs, improving upon the efficiency of previous methods for accessing this material. Chapter V probes the ability of several size determination techniques to analyze three standard samples and binary and ternary mixtures made from those samples. This work shows that SAXS reliably identifies bimodal and trimodal distributions, while TEM has a more limited ability to do so. Lastly, Chapter VI probes AuNP growth *in situ* to determine whether a nucleation-and-growth mechanism is operative. This work shows that a coalescence mechanism is the most likely mechanism for growth when using Bunte salt ligands.

Bridge to Chapter II

Chapter I summarizes Au nanoparticle syntheses, mechanistic studies, and what ultimate lessons the synthetic chemist can learn from these studies. This chapter demonstrates the progress that has been made in AuNP synthesis, and where researchers are currently looking to improve upon these methods and make the next generation of advanced nanomaterials. Specifically, microreactors and SAXS are highlighted as important areas of progress. Chapter II utilizes a microfluidic platform to validate SAXS as a quantitative method for AuNP size determination against traditional TEM analysis, utilizing UV/visible spectroscopy as a bridging technique.

CHAPTER II

DETERMINING NANOPARTICLE SIZE IN REAL TIME BY SMALL ANGLE X-RAY SCATTERING IN A MICROSCALE FLOW SYSTEM

This chapter was coauthored with Lallie C. McKenzie who assisted in both data collection and manuscript editing. Dr. Stephen D. Kevan provided assistance in processing and interpreting small-angle X-ray scattering data. My advisor, Dr. James E. Hutchison, helped conceptualize the project and provided editorial assistance.

Introduction

Precise structural analysis is becoming more important as we seek to identify and harness the size-dependent physical and biological properties of nanomaterials,[1-3] yet most current analytical approaches provide incomplete structural information. For example, the most widely used technique, transmission electron microscopy (TEM), provides precise, structural information on individual nanostructures but requires that samples be isolated prior to analysis, is time-consuming, only probes a small number of particles, and is subject to sample preparation artifacts.[1,4] A popular alternative involves solution-based measurements, such as optical absorption or emission spectroscopy, that sample statistically larger numbers of particles and require no isolation or specialized sample preparation. However, these methods cannot directly determine nanoparticle size or structure.[5,6] A variety of other techniques (e.g., dynamic light scattering, atomic force microscopy, field flow fractionation, differential mobility analysis) have been used to determine nanoparticle size, but these do not measure the core diameter directly. Additionally, each measured value is uniquely influenced by the nature of the ligand shell

of the particle and the measurement medium (e.g., solvent). Definitive determination of core size and size distribution within a nanoparticle sample, therefore, requires the use of multiple techniques in combination with TEM, as has been done for gold nanoparticle reference materials.[7]

Small-angle X-ray scattering (SAXS) has shown promise as a method for precisely determining the size, shape, and polydispersity of a variety of nanoparticles in solution.[5-14] The SAXS measurements of core size and dispersity for a variety of metal and metal oxide nanoparticles have been shown to correlate well with those obtained from other techniques (e.g., TEM, XRD).[8-12] Of particular interest to this work, SAXS has been demonstrated to be a fast and precise method for determining the sizes and size distributions of a series of gold nanoparticle reference materials.[13] The *in situ* application of a wide range of X-ray techniques, using a variety of cells and reactors, has facilitated the study of many complex structural reorganization processes at the nanoscale.[14-18] In particular, time-resolved reaction data have provided insights into new intermediate species, reaction kinetics, and nanoparticle growth mechanisms.[8-11,19-24]

Monitoring the dynamics of nanoparticle systems by SAXS presents a number of challenges related to the need for long data acquisition times. In sealed capillaries and stopped-flow reactors, extended data collection times reduce the temporal resolution of the experiment and therefore preclude the study of fast reactions.[9,11,12,19,21] Another complication with X-ray monitoring of nanoparticle reactions involves damage to the sample or radiation-induced reactivity of the species in solution during extended and/or intense X-ray exposure.[22,25] Recent work suggests that flow-based, *in situ* SAXS analysis could improve time resolution and increase signal-to-noise ratios and reduce the potential for beam damage.[23,26] However, direct corroboration of the *in situ* measurements by TEM

was not possible because the particles continue to grow during the time between the SAXS and TEM measurements.

The challenges highlighted above led us to develop a new multitechnique approach for analyzing nanoparticles in real time wherein *in situ* SAXS and UV-vis measurements could be validated using *ex situ* UV-vis and TEM. UV-vis data serve to bridge *in situ* and *ex situ* analyses. Thus, a critical aspect of our strategy was the design and use of a microscale flow system that included a custom-made monitoring cell for simultaneous, *in situ* SAXS and UV-vis analysis (Figure 1). Commercially available syringe pumps, fittings and tubing were incorporated to feed standardized nanoparticle solutions through the cell while SAXS and UV-vis absorbance data were collected through perpendicular observation pathways. A selection valve and separate syringe were included so that clean solvent could flow through the system for rinsing and background collection. Although the work we describe here focused on monitoring static nanoparticle populations, the system was designed so that residence time in the system could be correlated to reaction time of rapidly changing nanoparticle populations.

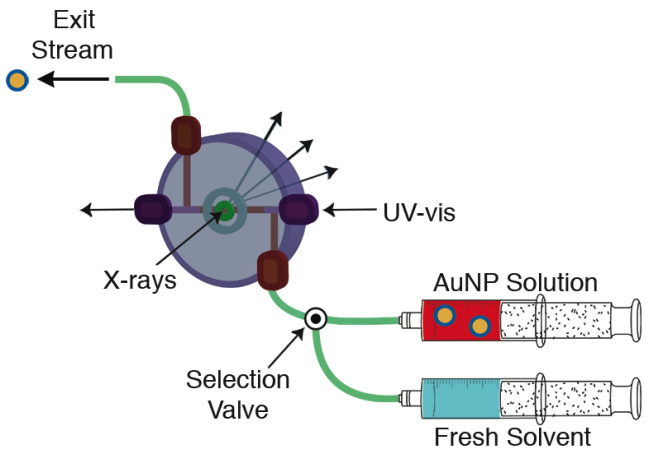

Figure 1. Microscale flow system with specially designed cell for *in situ* multitechnique measurement of nanoparticle size distributions. As shown in the diagram, flowing nanoparticle solutions pass through the cell where the nanoparticles are probed simultaneously by UV-visible spectroscopy and SAXS through perpendicular observation paths. The flow system permits extended data collection without X-ray damage, and the acquisition time is limited only by syringe volume. Switching the selection valve accesses a solvent syringe for rinsing and background collection.

Here we report the real-time SAXS and UV-vis measurement of a series of ligand-stabilized Au nanoparticle standards (d_{CORE} = 0.8, 2, 3 and 5 nm) within a microscale flow system and corroboration of those measurements with *ex situ* techniques. These precisely engineered, purified samples have defined structures and core diameters within a size range that is expected to be present during early stages of nanoparticle growth. The use of stable, prefabricated nanoparticles permitted extended analysis of the materials, ensured stability during the flow studies, and validated the applicability of the approach for a range of nanoparticle populations. Continuous monitoring by UV-vis and comparison to *ex situ* measurements confirmed the identity, stability and concentration of

the nanoparticle population in the X-ray path. This approach allows *in situ* SAXS and *ex situ* TEM measurements to be correlated through the direct comparison of associated UV-vis spectra.

Experimental

Materials

Hydrogen tetrachloroaurate hydrate ($HAuCl_4 \bullet xH_2O$, 99.9%) was purchased from Strem and used as received. Dichloromethane was distilled over calcium hydride prior to use. Nanopure water was prepared with a Barnstead NANOpure filtration system (18.2 MΩ cm) and used for all aqueous samples. $Au(PPh_3)Cl$ and mercaptoethoxyethoxyethanol (MEEE) were synthesized according to known procedures.[4,27,28] Sephadex LH-20 was obtained from GE Healthcare/Amersham Biosciences. All other reagents and solvents were purchased from Aldrich or Mallinckrodt and used as received.

Nanoparticle Synthesis and Functionalization

Synthesis of Au_{11}. Triphenylphosphine-stabilized undecagold (Au_{11}) was synthesized by previously reported methods.[29,30] Briefly, 55 mL of absolute ethanol was added to a 100-mL round bottom flask containing 1.00 g (2.02 mmol) $Au(PPh_3)Cl$. The cloudy white solution was stirred while finely ground $NaBH_4$ (76 mg, 2.02 mmol) was added in small portions over 15 min (~1 addition/minute). After stirring at room temperature for two hours, the mixture was poured into hexanes (1 L) and allowed to precipitate overnight (~20 hours). The brown precipitate was collected and washed with hexanes (4 X 15 mL), CH_2Cl_2/hexanes (1:1, 4 X 15 mL), and CH_2Cl_2/hexanes (3:1, 1 X

10 mL). The remaining solid was dissolved and washed through the frit with CH_2Cl_2 (~ 40 mL). Crystallization by vapor diffusion of hexanes/CH_2Cl_2 at 4 °C produced red and orange crystals (~180 mg). The UV-vis (Appendix A) and NMR data were in agreement with the literature, and the particles were used without further functionalization. Single-crystal X-ray structure determination of Au_{11} compounds has indicated that the cores of these species are almost identical with slight distortions due to ligand substitution.[31] TEM analysis yielded a size distribution of 0.8 ± 0.4 nm (Appendix A).

Synthesis of 2nm-AuNP-MEEE. MEEE-stabilized Au nanoparticles were synthesized through a previously reported two-step procedure. Precursor PPh3-stabilized Au nanoparticles (Au-TPP) were synthesized as described by Hutchison et al.[32] The data were in agreement with the literature. MEEE ligand exchange reactions were performed as described in the literature with minor modifications.[28,32] Briefly, Au-TPP (80 mg in 40 mL of CH_2Cl_2) and MEEE (80 mg in 40 mL water) were stirred rapidly at room temperature for 8 hours until the transfer of the nanoparticles to the aqueous layer was complete. Upon completion of the exchange, the layers were separated, and any residual CH_2Cl_2 was removed from the aqueous layer in vacuo. The aqueous layer was concentrated and purified via column chromatography using Sephadex LH-20. The purified nanoparticles were lyophilized and stored as a solid at -20 °C. The absence of sharp resonances from the free ligand and resonances in the aromatic region in the ^1H NMR spectrum indicated that the sample was pure and that the exchange had gone to completion. The average core diameter was 2.6 ± 1.3 nm as determined by TEM. The TEM micrographs, however, showed a significant amount of aggregation and/or agglomeration (Appendix A). This suggests that the size of the nanoparticles determined via TEM is larger than the average size of those in solution. Additionally, the UV-visible

spectrum included a broad absorbance and no evidence of a surface plasmon band, indicating a core diameter of <2 nm (Appendix A).

Synthesis of 3nm-AuNP-MEEE. MEEE-stabililized Au nanoparticles were synthesized through a procedure developed by Brust and co-workers with minor modifications.[33] Briefly, in a 125-mL round-bottom flask, MEEE (0.0126 g, 0.1 mmol) and $HAuCl_4$ (0.1050 g, 0.322 mmol) were dissolved in 40 mL of 2-propanol, yielding a yellow solution. To this solution, 5.5 mL of a 1.6 M methanolic $NaBH_4$ solution was added rapidly with stirring, which resulted in an immediate color change from yellow to dark purple. The solution was stirred under ambient conditions for 1.5 hours and was then filtered through a 150-mL fine porosity fritted funnel. The resulting dark solid was washed through the frit with 20 mL of water. The nanoparticles were purified through diafiltration with 300 mL of water using a 70 kDa diafiltration membrane (Pall).[34] The solution was concentrated to 10 mL by ceasing makeup flow, and the nanoparticles were collected by pumping the solution into a 20-mL scintillation vial. The purified nanoparticles were lyophilized and stored as a solid at -20 °C. As for 2nm-AuNP-MEEE, the absence of sharp resonances from the free ligand and resonances in the aromatic region in the 1H NMR spectrum indicated that the sample was pure and that the exchange had gone to completion. Measurement by TEM indicated that the average core diameter was 3.4 ± 1.7 nm (Appendix A). A broad surface plasmon band dominated the UV-visible spectrum, suggesting nanoparticles with a core diameter of >2 nm (Appendix A).

Synthesis of 5nm-AuNP-MEEE. MEEE-stabilized Au nanoparticles were synthesized through MEEE ligand exchange reactions with Au nanoparticles stabilized with tetra-n-octylammonium bromide (TOAB) through a previously reported procedure with minor modifications.[35] Briefly, in a 500-mL round-bottom flask, $HAuCl_4$ (0.74 g,

1.8 mmol) was dissolved in 60 mL of H_2O, yielding a yellow solution. TOAB (4.4 g, 8 mmol) was dissolved in 160 mL of toluene and added to the reaction flask, and the mixture was stirred for two hours, producing a red organic phase. 50 mL of a 0.4 M $NaBH_4$ solution in water was added over the course of two minutes, with stirring, resulting in an immediate color change from red to dark brown. The solution was stirred under ambient conditions for 5 h. The organic phase was separated, washed with H_2O (3 X 50 mL), dried over sodium sulfate, filtered, and diluted to 375 mL. To a 250-mL round-bottom flask was added 50 mL of toluene solution of TOAB-stabilized Au nanoparticles. MEEE (0.325 g, 3.3 mmol) was dissolved in 50 mL of H2O and added to the reaction flask. The mixture was left to stir under ambient conditions for 16 hours. After the color transferred to the aqueous layer, it was separated, washed with toluene (20 mL), concentrated to ~5 mL of solution, and purified via column chromatography using Sephadex LH-20. The purified nanoparticles were lyophilized and stored as a solid at -20 °C. Sharp resonances in the NMR spectrum indicated the presence of a small amount free ligand and remaining TOAB. However, the exchange had gone to completion and the impurities were not expected to impact the experiments, so no further purification was performed. The UV-visible spectrum included a strong, narrow surface plasmon band (Appendix A), suggesting the presence of larger nanoparticles, and the average core diameter was 5.3 ± 2.1 nm as determined by TEM (Appendix A).

Microscale Flow System

Two syringe pumps (Kloehn Versa 6), a selection valve, PTFE tubing (1/16" OD, 0.030" ID), and a monitoring cell were assembled into a flow system using fittings and connectors (Upchurch). The monitoring flow cell was machined from a cylinder of Kel-F with perpendicular pathways for X-ray and UV-visible measurements. Solutions were

pumped at a flow rate of 0.125 – 4.8 mL/min through a predetermined length of tubing into an inlet in the bottom of the cell, crossed through the middle of the cell, and exited through the top. Solution concentrations were adjusted to be similar to those used in nanoparticle syntheses (i.e., 4-6 mM in Au atoms as calculated from concentrations of Au precursors). Background spectra were collected using the selection valve to allow solvent to flow through the system. Bubble traps (Stovall Life Sciences, Inc.) were incorporated to eliminate the propagation of bubbles through the flow system. The SAXS measurements were collected across the flow channel (path length = 750 μm) through parallel mica windows that were seated in removable stainless steel holders and twisted into the cell to form the sides of the channel. UV-visible absorbances were collected along the flow channel with variable pathlength optical fibers that extended into the channel and attached to the cell with ferrules and ¼-28 fittings (Ocean Optics). The pathlength for UV-vis measurements varied from 4-10 mm and was adjusted based on the nanoparticle concentrations.

Analytical Procedures

Transmission electron microscopy (TEM) was performed on a Philips CM-12 operating at 120 kV accelerating voltage. Samples were prepared by aerosol deposition of aliquots of nanoparticles dissolved in CH_2Cl_2 or H_2O onto SiO_2 Smart Grids™ (Dune Sciences) or carbon-coated Cu grids (Ted Pella).[4] The samples were dried under ambient conditions prior to inspection by TEM. Images were recorded and processed as described previously.[4] UV-visible spectra of nanoparticle solutions (CH_2Cl_2 or H_2O) were obtained with an Ocean Optics USB2000 spectrometer using 1-cm quartz cuvettes. Nuclear magnetic resonance (NMR) spectra were collected on a Varian Unity Inova 300 MHz

instrument equipped with a 4-channel probe. For 1H NMR spectroscopy, the spectra were collected from samples dissolved in CD_2Cl_2 or D_2O, and chemical shifts were referenced to the residual proton resonance of the solvent.

In Situ Measurements

SAXS measurements were performed at BL 11.3.1 and BL 7.3.3 at the Advanced Light Source (ALS, LBNL, Berkeley, CA). BL 11.3.1 is an X-ray diffraction facility that is mounted on a regular ALS bending magnet that provides monochromatic X-rays in the range of 6-17 keV (0.73 - 2 Å). X-ray beams of 11 keV were used for these experiments, and the spot size at the sample was 100 μm. The volume of solution observed by SAXS, defined by the pathlength and the dimensions of the X-ray beam, is 0.18 μL. At a flow rate of 0.08 mL/sec, this volume is refreshed every two milliseconds. A CCD detector (Bruker/ Fairchild) was used to record images that were processed to determine the scattering intensity, I(q), as a function of the modulus of the scattering vector $q=(4\pi/\lambda)$ $\sin(\theta/2)$, where θ is the scattering angle and λ is the wavelength of the X-rays. BL 7.3.3 is a SAXS/WAXS facility and also is mounted on a regular ALS bending magnet. A Mo/BC double multilayer monochromator provides monochromatic X-rays at 10 keV, and the spot size at the sample is 1 mm horizontal x 0.24 mm vertical. The scattering intensity was recorded using ADSC Quantum 4u CCD detectors. With SAXS and WAXS measurements, the total q range of the system is between 0.004 and 8.7 A^{-1}. The accumulation time for SAXS measurements of each sample was between two and five minutes. Several measurements were taken for each sample and averaged to determine scattering intensity. The observed scattering intensities were corrected by subtraction of scattering of the solvent-filled cell and with corrections for the fluctuation of the beam

intensity. *In situ* UV-visible absorbance spectra were collected from flowing nanoparticle solutions in methanol or H_2O using ferrule-terminated fiber optics (Ocean Optics - FIA-P400-UV), an Ocean Optics DT-MINI-2-GS Deuterium-Tungsten-Halogen light source, and an Ocean Optics USB2000 spectrometer.

SAXS Data Analysis

SAXS data were processed using IGOR Pro v6.02A software. SAXS data averaging, background subtraction, and conversion from 2D CCD images to 1D plots were performed using the Nika v1.17 macro.[36] Application of models to the SAXS plots was performed using the Irena v2.27 macro.[37] Solvent plots were normalized at large q values to compensate for the variation in X-ray intensity between runs. Normalized solvent plots were then subtracted from corresponding Au nanoparticle plots, and the resultant data were fitted to an appropriate model as discussed below.

Each set of Au nanoparticle data was fitted to a monomodal distribution of scatterers, and each component of the distribution was modeled using a spheroidal form factor, F, defined by the equation:

$$F^2 = \frac{3}{qR^3} * (\sin(qR)) - (qR * \cos(qR)) \qquad (1)$$

where q refers to the scattering vector in nm^{-1} and R is the average spheroid radius. Data were fitted to both Gaussian and lognormal distributions of nanoparticle sizes. Best-fit models were developed by minimizing χ^2 values. In all cases, models using a lognormal distribution output a smaller χ^2 value than for the corresponding Gaussian distribution. Thus, all reported values for nanoparticle size and polydispersity have been derived from

models using a lognormal distribution. Final SAXS patterns were depicted as $I_{fit}(q)$ vs. q, where q is expressed in nm^{-1} and $I_{fit}(q)$ is defined by the equation:

$$I_{fit}(q) = |\Delta\rho|^2 \sum_{r_{min}}^{r_{max}} |F(q,r)|^2 V^2(r) * N * P(r) * \Delta\rho \qquad (2)$$

where $\Delta\rho$ refers to contrast, F(q,r) is the structure form factor, V(r) is the particle volume, N is the total number of scattering particles, and P(r) is the probability that a particle possesses a radius equal to r according to the lognormal distribution.

The same standardized modeling procedure was utilized to fit the data for all samples. Models were applied to the SAXS data over select q ranges where signal-to-noise ratios were adequate and the scattering intensity was reproducible between runs. The 5nm-AuNP-MEEE SAXS data were fit from q = 0.64 – 2.3 nm^{-1}, 3nm-AuNP-MEEE data were fit from q = 0.60 – 2.6 nm^{-1}, 2nm-AuNP-MEEE data were fit from q = 0.82 – 3.8 nm^{-1}, and Au_{11} data were fit from q = 1.5 – 4.5 nm^{-1}. Best-fit models were developed for each data set by iteratively refining distribution parameters and performing a cross-correlation analysis to determine which values minimized χ^2. We have not reported these χ^2 values in this publication because some of the models resulted in χ^2 values of less than one. Although χ^2 values are expected to be greater than one, anomalous error values are sometimes recorded because the modeling software is designed to use a multitude of different detectors. The modeling software only assesses quality of fit by minimizing χ^2, regardless of whether the value is greater or less than one. Therefore χ^2 values are a valid method to identify the best fit for given SAXS patterns, but comparisons of these values across data sets are not meaningful. In our recent studies at a beamline optimized for SAXS measurements, we typically obtain χ^2 values of 1-5. In all cases, lower χ^2 values

corresponded to a closer fit between the model and the data, as determined by analyzing residual values. All final models fit the data well over the q ranges of interest.

Results and Discussion

A series of ligand-stabilized Au nanoparticle standards was synthesized and analyzed to facilitate comparisons between *in situ* and *ex situ* techniques. Simultaneous UV-visible spectra and SAXS patterns were collected using a specially designed observation cell embedded within a microscale flow system. The SAXS measurements of the four standards were correlated to *ex situ* TEM measurements via bridging UV-visible spectroscopy.

Standard Nanoparticles

We chose a series of small Au nanoparticles with average core diameters of 0.8, 2, 3, and 5 nm as standard materials for our flow experiments because these core sizes would be present during the early stages of nanoparticle growth reactions. They are also of interest due to the size-dependent electronic and optical properties exhibited by small gold particles.[2,32,38-42] The nanoparticles were coated with ligand shells to fully passivate and stabilize the Au cores. The choice of standard materials facilitated comparisons between *in situ* and *ex situ* analytical techniques.

Prior to our experiments, the series of stable nanoparticles was prepared through direct synthesis or ligand-exchange reactions, purified, and stored as solids. Au_{11} (d_{CORE} = 0.8 nm) was synthesized by a procedure described previously.[41,43] MEEE-stabilized Au nanoparticles with average core sizes of 2, 3, and 5 nm (2nm-AuNP-MEEE, 3nm-AuNP-MEEE, and 5nm-AuNP-MEEE) were synthesized through previously reported one- or

two-step procedures with minor modifications.[28,32,33,35,41] Each standard nanoparticle sample was fully characterized by ^{1}H NMR, TEM imaging, and UV-visible spectroscopy (Appendix A) to confirm the previously reported compositions and structures.

Quantitative *ex situ* measurements of the size and size distributions of the four standard samples were determined by TEM. Au_{11}, 2nm-AuNP-MEEE, 3nm-AuNP-MEEE and 5nm-AuNP-MEEE were determined to have average sizes and size distributions of 0.8 ± 0.4 nm, 2.6 ± 1.3 nm, 3.4 ± 1.7 and 5.3 ± 2.1 nm, respectively. In each of these samples some degree of aggregation and/or agglomeration was observed as a consequence of the sample deposition. Aggregation and/or agglomeration inflates the average core size and uniformly leads to large size dispersities.[4,9,44]

UV-visible absorption spectroscopy provides qualitative information about particle size and served as a bridge between *in situ* and *ex situ* data. Because differences in the peak positions and shapes in UV-vis spectra can be used follow changes in core size, the optical spectra provide a method for verifying that the nanoparticles were stable prior to and during the flow experiments. Thus, baseline *ex situ* data were collected for each of the four samples. All Au_{11} spectra showed the expected sharp absorbance peaks due to molecule-like transitions.31 The slightly larger 2nm-AuNP-MEEE sample exhibited a broad featureless optical absorbance spectrum with no evidence of a surface plasmon band, which indicated a core diameter of <2 nm. For the larger 3nm-AuNP-MEEE sample, a broad surface plasmon band dominated the UV-visible spectrum and suggested that the nanoparticles had a core diameter of >2 nm. The UV-visible spectrum of the largest nanoparticle sample, 5nm-AuNP-MEEE, included a strong, narrow surface

plasmon band in the region of 520 nm that suggested the particles possessed core diameters >3 nm.[45]

Technique Development and Cell Design

A primary goal for this research was to develop an *in situ* method for quantitatively determining nanoparticle size and dispersity under conditions typical of nanoparticle growth reactions. Use of a microscale flow system and specially designed monitoring cell addressed many of the challenges inherent in SAXS measurements of nanoparticles in solution. In contrast to stopped-flow reactors or sealed capillaries, continuous-flow systems provide extended access to steady-state populations of species at a given tubing length and flow rate. Data collection times of several to tens of minutes are possible and are limited only by the capacity of the syringe used and the flow rate. Longer acquisition times provide increased signal-to-noise ratios, making it practical to collect useful data from dilute solutions or weak scatterers moving through the system.[8-11,19-22] A further benefit of the flow-based approach is reduced X-ray exposure. Whereas deleterious effects of X-rays on the sample accumulate in capillary or stopped-flow systems, the influence of X-rays in a flowing system is minimized because exposures are very short and any damaged materials rapidly move out of the region of the probe. These considerations are particularly important when studying nanoparticle reactions with synchrotron radiation because intense X-ray exposure can induce nanoparticle deposition or decomposition and can also lead to new particle formation.[22,46]

Initial studies conducted with quartz capillary tubing motivated the need to develop the monitoring cell described herein. In those studies, consistent alignment of the capillary, and thus collection of reliable scattering patterns for samples and solvent

backgrounds, was not possible. These problems motivated the development of a cell that could be easily aligned and fixed in position. In an ideal cell, samples could be introduced and rinsed out by a flow system, permitting a fixed geometry that would facilitate comparison of sample and solvent background runs. In addition, a convenient technique such as UV-vis was desired to assess the presence of sample in the X-ray beam. Thus, we designed a monitoring cell that included an integrated flow path for nanoparticle solutions and provided inline access to simultaneous SAXS and UV-vis measurements. UV-visible spectra can be used to verify both the presence and concentration of the nanoparticle solutions being investigated in real time and assess conditions in the cell.

The monitoring cell was integrated into a microscale flow system that included syringe pumps, tubing and fittings, and a selection valve. For each measurement, solutions were pumped through a predetermined length of tubing into an inlet in the bottom of the cell, crossed through the middle of the cell, and exited through the top (Figure 1). To maximize SAXS signals, these measurements were collected across the flow channel (path length = 750 μm) through easily replaceable parallel mica windows that formed the sides of the channel. To extend the range of UV-vis absorption measurements, the spectra were collected along the flow channel with variable pathlength optical fibers that extended into the channel and attached to the cell with ferrules and fittings. The pathlength for UV-vis measurements varied from 4-10 mm and was adjusted based on the nanoparticle concentrations. SAXS patterns were collected only when consistent conditions in the cell were indicated by stabilization of the absorbance spectra (i.e., equilibrated concentrations and no air bubbles). Background spectra of the solvent were collected using the selection valve to flush solvent through the system.

In our initial trials, reliable subtraction of the background from SAXS profiles was challenging due to scattering from the solvents used and gas bubbles within the observation cell during data collection. In fact, most of the intensity in the SAXS patterns results from scattering by the solvent because of the small core diameters of the nanoparticle samples and dilute nature of the solutions. Preliminary experiments were conducted in ethanol, but scattering in the range of $q = 6 – 10$ nm^{-1} (a range of interest) prevented consistent background subtraction when this solvent was used. An analysis of SAXS interference of potential solvents (Appendix A) led to the use of water and methanol for further work in the flow system. These solvents provided effective solvation of nanoparticle samples and lower scattering intensity in the region of interest. Occasionally, UV-vis measurements indicated that bubbles became lodged in the cell. These interfered with consistent measurement of SAXS intensities but could be eliminated by placing commercially available bubble traps upstream of the flow cell.

Nanoparticle solutions were analyzed by SAXS and UV-visible spectroscopy in the flow system to determine concentrations and exposure times needed to provide high signal-to-noise ratios and reproducible values of nanoparticle core size. Concentrations similar to those used in nanoparticle syntheses, 4-6 mM in Au atoms, required SAXS exposure times of 2-5 minutes in order to provide adequate signal. Slow flow rates maximized the flow time for a given volume of solution, and continuous flow enabled a series of SAXS patterns to be collected from each nanoparticle solution. The separate data points could be compared or averaged. As expected, shorter exposure times could be used for the larger nanoparticles, but five-minute data collection was necessary to extend this method to core diameters of ≤ 2 nm.

In order to determine the reproducibility of the SAXS data obtained from the flow system, multiple processed SAXS patterns of the same sample were compared. Solutions of Au11 were used for this experiment as a stringent test of the system because these samples are the weakest scatters and possess the lowest signal-to-noise ratios of the standard samples. SAXS data were collected during a series of 5-minute runs of the same Au_{11} sample. After rinsing the cell until there was no evidence by UV-vis of residual nanoparticles, scattering patterns from solvent were collected for the same exposure times as for samples. By collecting multiple sample and background scattering patterns, we were able to determine that the background-subtracted SAXS patterns were reproducible over multiple runs. For example, Figure 2 shows two pair of SAXS profiles derived from two different five-minute SAXS exposures of flowing Au_{11} in methanol and two separate 5-minute exposures of flowing methanol. After background subtraction the patterns overlapped from 1.5 – 5 nm^{-1} and yielded nearly identical average diameter values. Deviations were observed only at low and high q and resulted from differences in scattering near the beamstop and from the solvent, respectively. The data in the figure confirmed that the microscale flow system provides precise, reproducible SAXS measurements of extremely small nanoparticles in dilute solutions.

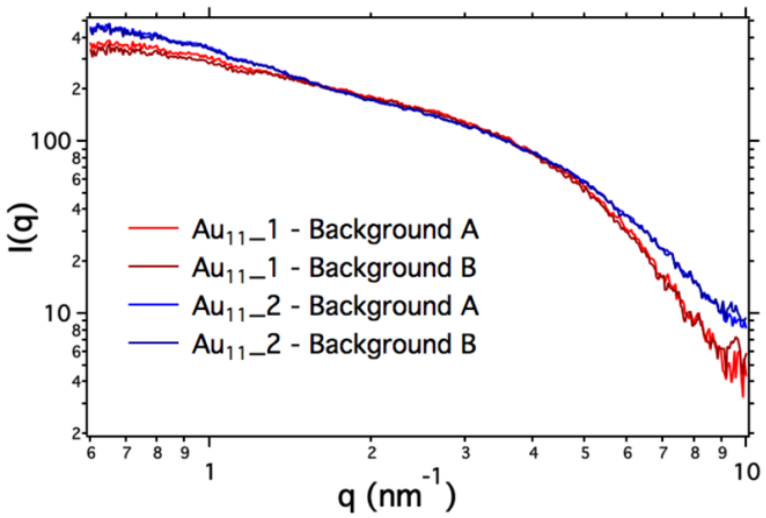

Figure 2. Reproducible background-subtracted SAXS patterns of flowing methanolic solutions of triphenylphosphine-stabilized Au_{11}. Patterns for two different samples of Au_{11} were each analyzed after subtracting either of two background scans. Each of the resulting scattering patterns is superimposable over the range of 1.5 – 5 nm^{-1}. These patterns were chosen from a larger data set to illustrate the reproducibility in the middle of the q range and the deviations in the data at high and low q that result from solvent scattering and scattering near the beamstop, respectively.

In Situ Measurements and Data Modeling

Once optimized conditions for data collection had been developed, *in situ* UV-vis spectra and SAXS patterns were collected from flowing aqueous solutions of the thiol-stabilized Au nanoparticles (5nm-AuNP-MEEE, 3nm-AuNP-MEEE, and 2nm-AuNP-MEEE) and methanolic solutions of Au_{11} (Figure 3). Solvent scans were collected both before and after each sample run to facilitate background subtraction and quantify any potential material deposition. SAXS patterns were converted from 2D patterns to 1D plots of intensity vs. q via radial integration.[36,37] Converted plots from each nanoparticle

flow run were averaged and then the analogous, averaged background plot was subtracted. Background solvent plots were normalized at large q values to compensate for the variation in X-ray intensity between runs. Appropriate models were fitted to the background-subtracted plots to determine nanoparticle core size and dispersity. Reported values for nanoparticle diameter and polydispersity were obtained from models fit to a lognormal distribution with quality of fit being determined through comparison of χ^2 values.

Upon examination of the processed data several features were noted that provided qualitative assessments of nanoparticle size and polydispersity. As shown in Figure 3, the plots for the larger particles exhibit higher scattering intensity and curve toward baseline at comparatively lower q values than for the smaller particles. Additionally, each of the four plots curve smoothly toward the baseline without inflection points or shoulders, suggesting a single distribution of particles is present in each sample. Plots for the two larger standards exhibit characteristic increases in scattering intensity at higher q values, suggesting a narrow distribution of particle sizes. In contrast, the fact that the 2nm-AuNP-MEEE sample does not exhibit a region of increased scattering intensity at high q suggests a more polydisperse size distribution. The q range accessible in these experiments was not wide enough to determine whether the Au_{11} sample exhibited these characteristic increases in scattering intensity.

The quantitative values determined by fitting the models to the plots agree well with the qualitative trends observed in the data. Fits to the plots of 5nm-AuNP-MEEE, 3nm-AuNP-MEEE, 2nm-AuNP-MEEE, and Au_{11} yielded size distributions of 5.3 ± 0.8 nm (~15% polydispersity), 3.6 ± 0.6 nm (~17% polydispersity), 1.8 ± 0.5 nm (~30% polydispersity), and 0.8 nm (monodisperse population) respectively.

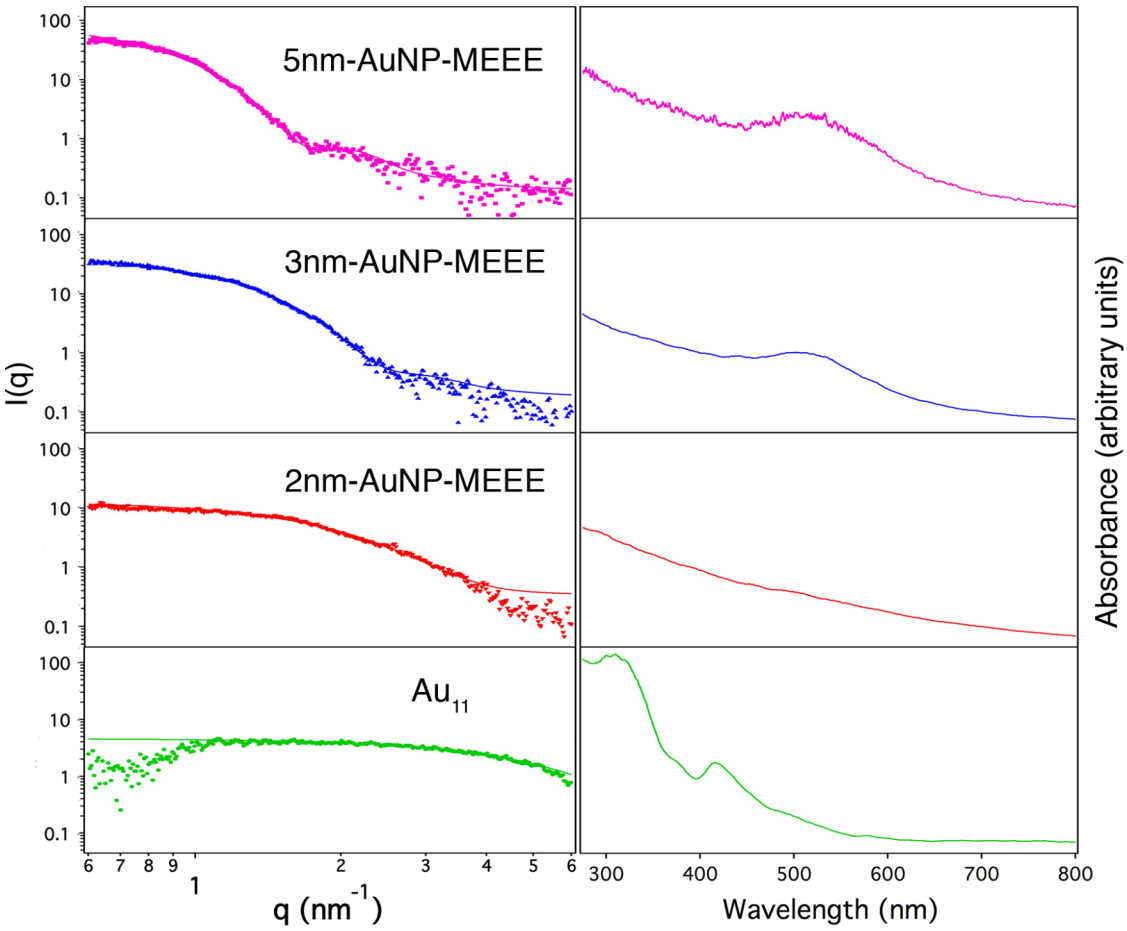

Figure 3. *In situ* SAXS (left) and UV-vis absorbance (right) data collected simultaneously for the set of reference AuNPs. SAXS patterns and corresponding UV-vis spectra were collected for a series of flowing solutions of nanoparticles of different core sizes and size distributions including 5-, 3-, and 2-nm thiol-stabilized Au nanoparticles and 0.8 nm phosphine-stabilized Au_{11}. The trend in the SAXS data (plotted as points) demonstrates more intense scattering at lower q for larger nanoparticles. The solid lines represent models fit to the data as described in the experimental section. The UV-vis data correlate with *ex situ* measurements and show the expected broadening of the spectra and enhanced absorption in the surface plasmon band as nanoparticle core size increases.

Models for 5nm-AuNP-MEEE, 3nm-AuNP-MEEE, and 2nm-AuNP-MEEE provide good fits to the SAXS plots, having χ^2 values < 2. These models fit particularly well at low q values, where the particles scatter X-rays intensely, but deviate from the data at higher q values where the particles scatter more weakly and therefore H_2O scattering becomes significant. The model for Au_{11}, in contrast, does not match the data well at low values of q. The increased error in this range is most likely a result of low signal-to-noise ratios from the weakly scattering subnanometer particles combined with parasitic scattering around the beamstop. In addition, scattering from methanol is more intense than water at all observed q values (Appendix A) and consequently decreases the signal-to-noise ratio for the Au_{11} data. Although modeling particles of this size is challenging due to their small size and low scattering intensity, we were able to routinely obtain good fits to the data using the approach described here.

Correlation of Techniques

Our approach utilized highly stable, ligand-passivated Au nanoparticles as standards to independently confirm the results of *in situ* (SAXS and UV-vis) and *ex situ* (UV-vis and TEM) techniques. We incorporated SAXS into this approach to determine quantitative size distribution information for nanoparticles in solution. Since SAXS is a model-based technique, it was important to validate the size analyses determined by SAXS through correlation to other analytical approaches.

As shown in Figure 4, simultaneous *in situ* measurement from the same sample volume allowed for direct comparison of the UV-vis spectra and SAXS data. Consistency in the optical absorbance between *in situ* and *ex situ* UV-vis measurements confirmed the identity, concentration, and stability of the standard samples contained

within the observation cell. Since the samples were probed by *ex situ* UV-vis and also analyzed by TEM, a quantitative size distribution could be linked to the representative optical spectra for each standard sample. Correlation of the *ex situ* TEM and *in situ* SAXS measurements therefore was possible through the bridging UV-vis data.

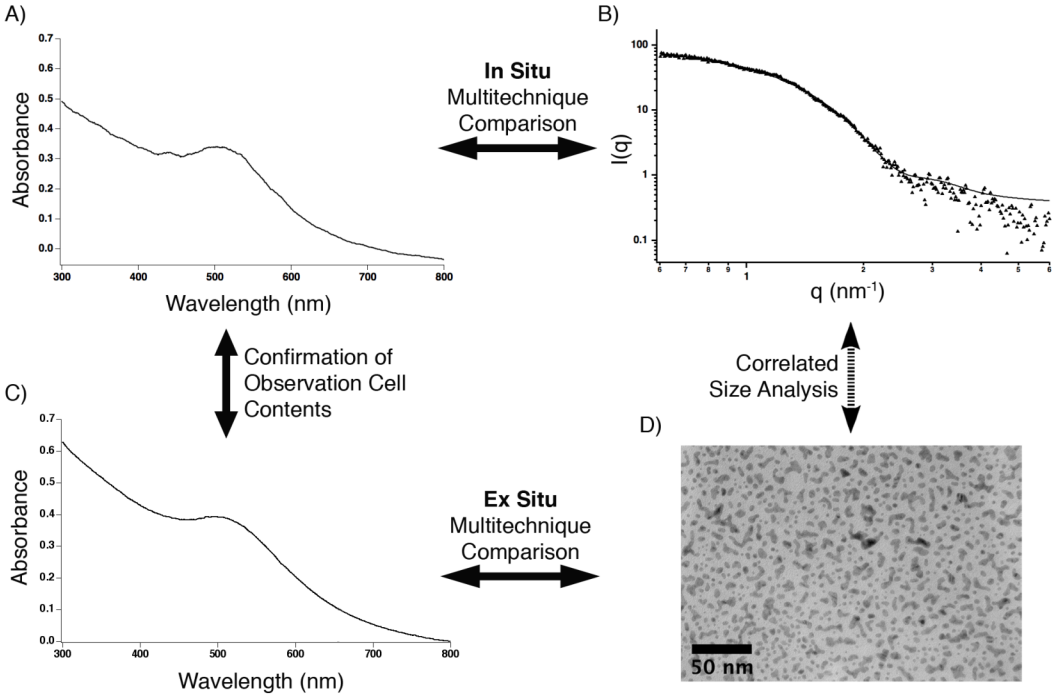

Figure 4. Correlated data for 3nm-AuNP-MEEE samples that establish a direct relationship between the SAXS and TEM measurements. *In situ* UV-vis (A) and SAXS (B) data were collected simultaneously on the same flowing sample volume providing an *in situ*, multitechnique comparison. The samples had been previously analyzed by *ex situ* UV-vis (C), and comparisons of the two sets of UV-vis data confirmed the identity and stability of the observed material. Direct visualization of the nanoparticles in the sample by TEM (D) facilitated the *ex situ* multitechnique comparison. Therefore, the use of UV-vis analysis as a bridging technique enabled the correlation of SAXS (B) and TEM (D) data.

As shown in Table 1, core diameter measurements from the SAXS data matched closely with those determined through *ex situ* TEM size analysis for most of the samples. For the 5nm-AuNP-MEEE, 3nm-AuNP-MEEE, and Au_{11} samples, the values fall within 0.2 nm of each other. In the case of 2nm-AuNP-MEEE, the core diameter determined by TEM is larger than the SAXS value, but the UV-vis spectrum does not show a plasmon absorbance for this sample (Figure 3). These data suggest that the particles are ≤ 2 nm in diameter and that the value determined by SAXS is more representative of the sample. The increased core size observed via TEM measurement is likely due to drying effects[4,9,44] upon deposition of the Au nanoparticles onto TEM grids (Appendix A).

Table 1. Comparison of size distribution measurements obtained from SAXS and TEM techniques

Nanoparticle Sample	Size Distribution[a]	
	by TEM (nm)	by SAXS (nm)
5nm-AuNP-MEEE	5.3 ± 2.1	5.3 ± 0.8
3nm-AuNP-MEEE	3.4 ± 1.7	3.6 ± 0.6
2nm-AuNP-MEEE	2.6 ± 1.3	1.8 ± 0.5
Au11	0.8 ± 0.3	0.8

[a] The size distribution is defined as the average diameter ± the distribution width. Both values are directly output by the Irena software.[37]

For every sample, the SAXS data exhibit lower polydispersity values than the TEM data. This trend might be expected since SAXS is a solution-based technique and is therefore devoid of sample deposition artifacts. In addition, the number of observed particles by SAXS is much larger than can be analyzed by TEM measurements. For example, in the 2nm-AuNP-MEEE sample, 978 particles were analyzed by TEM while

~5 x 1015 particles were analyzed by SAXS. The increased sample size of SAXS measurements combined with the avoidance of deposition effects result in the significantly lower polydispersities observed across the SAXS data set. In the case of Au_{11}, the TEM data show a 37% polydispersity while the SAXS data show a completely monodisperse population that has a distribution width less than the diameter of a single Au atom. The fact that the structure of Au_{11} has been determined by X-ray crystallography[31] and confirmed by UV-vis suggests that SAXS is a more accurate technique for assessing the size distribution of these particles. Collectively, the data in Table 1 show that this multitechnique approach is a valid method to obtain quantitative size distribution data for nanoparticles between 0.8 and 5 nm in diameter.

Conclusion

The results presented here show that it is possible to quantitatively determine nanoparticle sizes and distributions over the range of 0.8 to 5 nm in dilute solutions flowing through a microscale flow system. By using a series of small nanoparticle standards and a specially designed observation cell that enabled the simultaneous collection of *in situ* SAXS and UV-vis data, it was possible to compare *in situ* and *ex situ* UV-vis spectra and thereby corroborate the SAXS measurements with *ex situ* TEM analysis. Core sizes correlate well between these two techniques while SAXS exhibited systematically lower polydispersity values than TEM measurements. This approach establishes the foundation for the investigation of dynamic nanoparticle transformations in flowing solutions such as might be found when studying nanoparticle growth reactions. In the configuration described here, the microscale flow system is able to access residence times from 1.4 seconds to 14 minutes with a time resolution of 2 ms.

The ability to collect data for extended acquisition times for a steady-state population of particles within the observation cell opens the door to obtain kinetic data on nanoparticle formation reactions for which the reaction dynamics are too rapid to measure in bulk solution or in stopped-flow configurations.

Bridge to Chapter III

The work in Chapter II demonstrated that SAXS analysis is effective for precise determination of AuNP core size in solution. The determined core sizes correlated well with TEM size determinations, though SAXS analyses avoided deposition artifacts and observed much higher particle counts. Having demonstrated that this technique is reliable for AuNP size determination, SAXS was used as the primary method of size analysis for developing a new AuNP synthesis.

In Chapter III, a combination of microfluidic synthesis and rapid SAXS size analysis are used to reproducibly generate and measure AuNPs of a desired core size. Through tuning of Au(III) speciation, specific core diameters are targeted and synthesized from 2 – 10 nm. The precision of this targeted size control is unprecedented in previous literature.

CHAPTER III

DIRECT SYTHESIS OF FUNCTIONALIZED, WATER-SOLUBLE GOLD NANOPARTICLES WITH TARGETED CORE SIZES FROM 2-10 NM

This chapter was coauthored with Edward W. Elliott III, who assisted in experimental design, manuscript editing, and probing the species of Au(III) at varied pH's. My advisor, Dr. James E. Hutchison aided in project conceptualization and manuscript editing.

Gold nanoparticles (AuNPs) with size-dependent properties and chemical functionalities are being widely investigated.[1-5] Despite considerable effort to develop syntheses of thiolate-stabilized gold nanoparticles with specific core sizes and molecularly-defined surface functionality,[6] preparation of each new structural variant typically requires a considerable amount of trial and error to identify conditions that lead to the desired size and coating.[2] Here we describe a systematic approach to rapidly develop reaction conditions that produce water-soluble, functionalized AuNPs with specifically targeted core sizes over the range of 2-10 nm.

AuNPs have become frequent synthetic targets for applications that require (1) specific control of optical properties through tuning of core size and (2) chemical targeting combined with biocompatibility through control of the ligand shell. For example, recent interest has been directed towards the diagnosis and treatment of cancer as targeted contrast agents for CT imaging[7,8] and as agents for chemotherapy, hyperthermic therapy and radiotherapy.[9,10] In these applications both the optoelectronic properties and the fate and transport *in vivo* depend strongly on the nanoparticle size and functionality.[11,12] A recent study by Oh et al.[13] showed that for small oligoethyleneglycol-functionalized AuNPs,

particle diameter greatly influences localization to various cellular compartments.[14] The smallest, d_{CORE} = 2.4 nm, AuNPs localized to the nucleus, while 5.5 and 8.2 nm AuNPs localized to the cytoplasm, and 16 nm AuNPs did not enter the cell.

To realize the potential for analogous applications, synthetic methods are needed that offer simultaneous control over both targeted core size and ligand functionality. This is challenging due to the strong influence of ligand functionality on the resulting core size during synthesis. Although two-step synthetic methods involving core formation followed by ligand exchange have shown success,[2,15-17] each additional synthetic step adds complexity and introduces the potential for persistent impurities such as unexchanged ligands or surfactants.[2] Thus, a direct (single-step) process to produce this range of targeted materials would minimize complexity if the core size and surface coating can be independently controlled during synthesis.

Typical syntheses for sub-10 nm AuNPs are either limited in the range of accessible core sizes and functionalities available, involve multiple steps, and/or utilize toxic surfactants during particle formation. In the well-known biphasic Brust preparation, 2-8 nm particles are synthesized with organic soluble ligands in the presence of tetraoctylammonium bromide.[18] Ligand exchange is necessary to obtain water-soluble particles from this synthesis. Unfortunately, these exchanges are often time-consuming,[2,16] incomplete,[19-21] and may alter the core size of the particles.[4,15] To circumvent these issues, single phase methods were developed; however the size range available is further restricted to 1-4 nm.[22] Oh, et al.[23] employed specialized dithiol binding functionalities and large polymeric ligands to produce AuNPs over the range of 2-20 nm, utilizing ligand / gold ratio to control the core diameter.

In the examples above, size is controlled by adjusting the ligand / gold / reducing agent ratio,[24] however the size range available is typically constrained. In addition, the use of specialized ligands limits the types of functionality that can be introduced. We aimed to develop an alternative method of controlling the nanoparticle formation kinetics that would permit the use of a range of desired surface functionality.

We reasoned that it might be possible to control the reaction kinetics by taking advantage of the different reduction potentials of the Au(III) species that result from pH-dependent hydrolysis of $HAuCl_4$.[25,26] Initial attempts using this approach in the presence of thiol or disulfide ligands resulted in no significant variation in NP diameter (Appendix B), perhaps owing to the strong surface passivation of these ligands. Recent reports have demonstrated that AuNP diameter does depend upon the Au(III) speciation in the presence of a weakly-passivating ligands such as citrate or benzenesulfonate.[25,26] Thus, we explored the use of alkyl thiosulfates (Bunte salts) to control size through pH variation of the Au(III) solution while introducing desired functionality. Bunte salts are known to passivate the NP core weakly during nanoparticle growth, yet produce strong covalent linkages to the final AuNPs.[27-30]

Using this strategy we developed a direct synthesis of functionalized AuNPs with precise control over final core size across the range of 2-10 nm. AuNPs were synthesized with three different Bunte salt ligands in batch conditions. A Bunte salt, $HAuCl_4$ and $NaBH_4$ were combined (in a 1 : 5 : 2 ratio) in a round bottom flask stirred at moderate speed. $NaBH_4$ was first added to the flask, followed by Bunte salt solution, with $HAuCl_4$ added last. Prior to addition, NaOH was added to both the $HAuCl_4$ and $NaBH_4$ solutions. The base added to the $HAuCl_4$ solution controls the Au(III) speciation and thus AuNP

size (Appendix B). Base was added to the $NaBH_4$ solution to maintain the same final pH between batches.

Increasing the pH of the Au(III) solution produced larger particles as indicated by a shift in the plasmon λ-max in the UV/visible spectra.[31] (Appendix B). There appeared to be differences in the AuNP size dependence on pH when using different Bunte salt ligands, but the qualitative nature of optical spectroscopy and batch-to-batch variation precluded drawing definitive conclusions. Understanding this dependence on pH required quantitative size analysis, good reproducibility, and high throughput of synthesis and analysis.

In order to quantify the pH-dependent size trends, SAXS was performed on the AuNPs in solution.[32-34] TEM analysis confirmed that the particles were spherical but proved to be too time-consuming for efficient size determination.[35] SAXS analysis confirmed batch-to-batch variation in AuNP core size. When different researchers performed these syntheses, this variability was as high as 18% (Appendix B**)**. When a single researcher performed multiple syntheses in succession, the variation in AuNP core size was reduced to 5%. The use of microfluidic synthesis (Figure 1) to control reagent addition and mixing rates significantly reduces variation,[36] to less than 2%, even when performed by different researchers.[33,37,38]

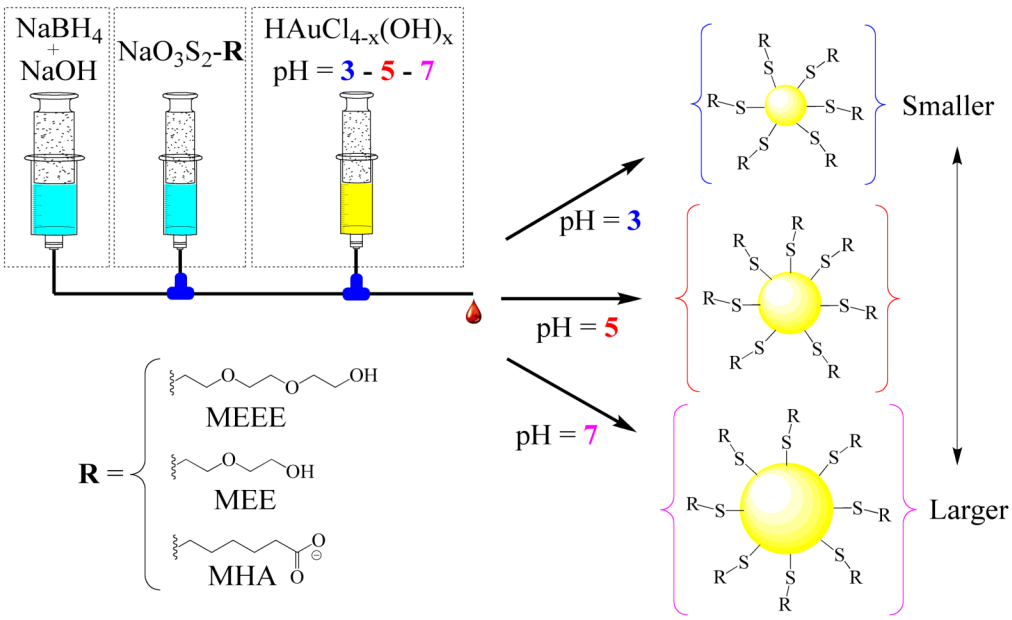

Figure 1. Microfluidic system for the synthesis of thiolate-passivated AuNPs using a selection of Bunte Salt ligands. Adjustment of the pH of the Au (III) solution produces NPs with targeted core diameters.

Microfluidic syntheses were performed at 60 mL/min using identical reagent ratios as previous batch syntheses. Thus, 10 mL of 5.0 mM $HAuCl_4$, 10 mL of 1.0 mM Bunte Salt ligand, and 20 mL of 1.0 mM $NaBH_4$ were prepared for each flow synthesis (40 mL total volume). A total of 0.825 mL of 1.0 M NaOH was added, divided between the $HAuCl_4$ and $NaBH_4$ solutions. The required amount of NaOH (ranging from 0.127 mL – 0.510 mL) was first added to the $HAuCl_4$ solution, changing the Au(III) speciation and controlling the final AuNP dimensions. Volumes of NaOH added and corresponding Au(III) solution pH values are summarized in Appendix B. The remaining amount of total NaOH was added to the $NaBH_4$ solution. The solutions were delivered by syringe pumps and mixed in Tefzel T-mixers connected by FEP tubing. Details are provided in Appendix B.

Combining the improvements from microfluidic syntheses and automated SAXS, we rapidly generated AuNPs with uniform, reproducible core sizes (Figure 2). There is a smooth, non-linear trend in AuNP core size as the pH of the Au(III) solution is scaled from ~ 3 to 7. From pH 3 to 5, a gradual increase in AuNP core size is observed. A more rapid rise in the slope of this trend occurs as the pH is increased, with the steepest slope observed as the pH approaches 7. The observed trend appears to correlate with the changing speciation of the Au(III) salt from $HAuCl_4$ to $HAuCl_{4-x}(OH)_x$ and finally to $HAu(OH)_4$ as pH increases. Multiple species co-exist at each pH (Appendix B).[26] The reduction potential of the Au species is most positive with four chloro ligands and decreases as hydroxo ligands are substituted onto the Au(III).[26] Greater substitution of hydroxo ligands decreases the rate of reduction and, consequently, increases the final AuNP core size. The change in the observed sizes correlates to the changes in Au(III) speciation across the measured pH range.

This synthetic method affords the ability to incorporate specific functionality on the AuNP surface while simultaneously maintaining control over core size. The NP size and surface chemistry were characterized using a multitechnique approach.[39] Details are provided in Appendix B. Briefly, XPS of the S2p region indicates the ligands are bound as thiolate, while TGA mass loss is consistent with a fully formed monolayer on the gold surface. AuNP functionality is confirmed by the presence of relevant peaks in the XPS spectra of the purified products and corresponding ratios of elements. Collectively these data suggest that the particles should exhibit the stability of thiol-stabilized AuNPs. The particles exhibited long term (> 3 months) stability in solution as well as stability during diafiltration, lyophilization and resuspension.[27-30]

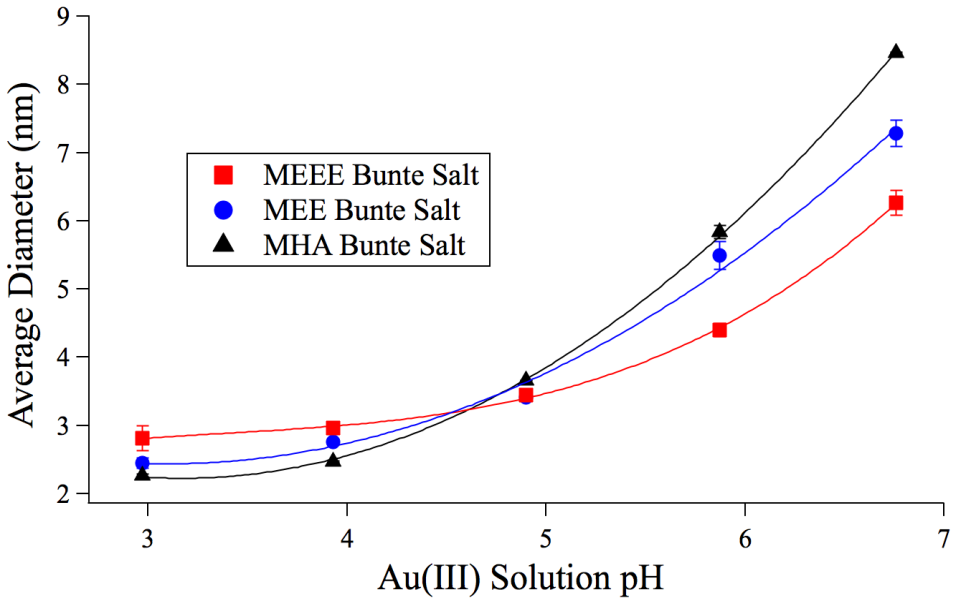

Figure 2. Compiled SAXS data for AuNPs made in a microreactor system showing smooth trends of core size vs. Au(III) solution pH. Each data point is the average of at least three synthetic runs.

Each of the three ligands examined in this study produced different plots of size vs. pH. At the extremes of pH, the dependence of size upon ligand type is reversed. At low pH, MEEE produces the largest NPs, whereas at high pH, MHA produces the largest cores. Thus, it is necessary to compare the particle sizes across this whole pH range to elucidate the ligands' effects on the passivation chemistry.

Given the smooth trend of particle sizes as a function of pH, we examined whether a continuous curve drawn through these points (a working curve) could be used to generate AuNPs with targeted core sizes.[40] These are particularly useful when describing complex trends or when mechanistic understanding is limited. Here the curves could be used to predict the pH needed to produce a particle with a specific core size for a selected ligand.

We tested the utility of the working curve shown for MHA in Figure 3 by attempting to synthesize 3.0, 5.0, and 7.0 nm functionalized AuNPs. Using values from the working curve, we determined the appropriate Au(III) solution pH for the targeted core sizes and then synthesized AuNPs at each of these conditions through addition of NaOH to the Au(III) solution (Appendix B). Size distributions determined by SAXS show that these syntheses produced AuNPs with diameters of 3.0, 4.9 and 6.9 nm respectively, with < 1% average variation in size between three runs. Each synthesis produced core diameters within 3% of targeted value. It was possible to target specific nanoparticle sizes for each of the ligands used in this study (Appendix B). These results suggest that the working curves are descriptive of the trend in AuNP size vs. Au(III) solution pH, and facilitate targeted synthesis of AuNPs across a continuous size range.

The direct synthetic method described here utilizes systematic control of Au(III) speciation using a variety of Bunte salt ligands targeting AuNP core sizes while independently tailoring functionality. This is the first work to utilize Au(III) speciation as a method for controlling the size of covalently-passivated AuNPs. The use of a microreactor facilitated rapid, more reproducible syntheses compared to batch reactions while an autosampler-equipped SAXS instrument provided rapid analysis of AuNP core size as-synthesized.[33,35] Future studies that require specific nanoparticle core sizes with different ligand shell functionalities should benefit from this method.

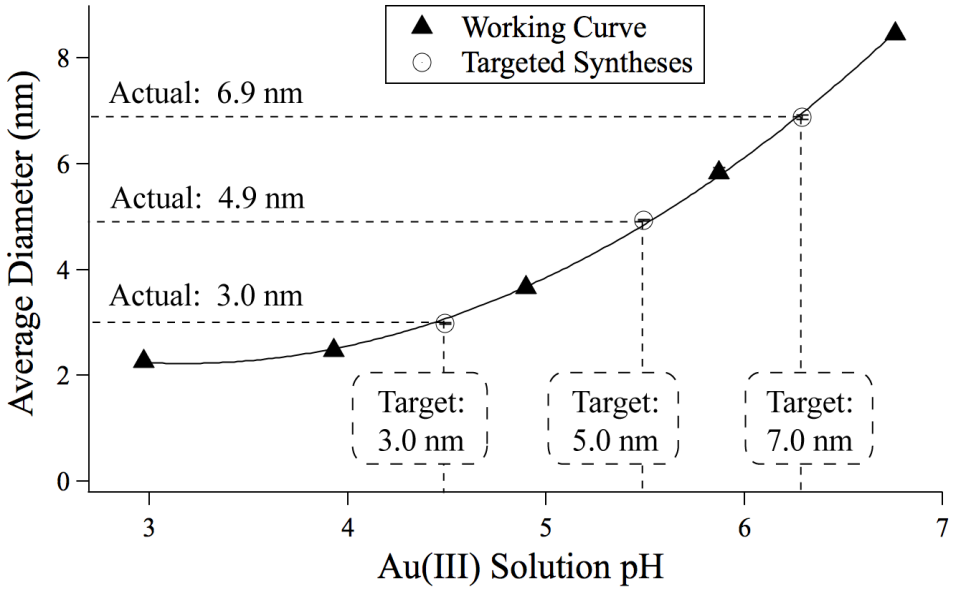

Figure 3. A working curve, fitted to the observed size data (using MHA Bunte salt ligand) guided the synthesis of AuNPs of a desired core diameter. Using the working curve to determine appropriate pH values for the Au(III) solutions, three particle sizes were targeted and synthesized within 3% of desired diameter.

Bridge to Chapter IV

The work in Chapter IV developed a new method for synthesizing targeted AuNP sizes across 2-10 nm. The only variable used to achieve this size control was Au(III) solution pH. Chapter IV focuses on extending this size range through variation of other synthetic variables. This chapter investigates flow rate, ligand concentration, and reducing agent concentration in order to access both larger and smaller AuNPs.

CHAPTER IV

EXTENDING THE SIZE RANGE AVAILABLE THROUGH THE SYNTHESIS OF GOLD NANOPARTICLES USING BUNTE SALTS: INVESTIGATION OF REACTION PARAMETERS

Introduction

Controlling the core size of gold nanoparticles (AuNPs) is crucial to researchers' ability to utilize the size-dependent properties of these materials for specific applications.[1-8] In previous work, we have demonstrated a high degree of control over AuNP core size by tuning the pH-dependent speciation of Au(III) in an aqueous microfluidic synthetic method.[9] While a useful range of sizes was produced with this method, it would be beneficial to extend this range of size control through variation of reaction parameters other than the pH of the Au(III) solution.[13,14]

The method we recently developed[9] utilizes a microreactor[15-17] to produce AuNPs with precise control over core size while introducing tailored functionality to the particle surface by using Bunte salt ligands (Figure 1).[18,19] A range of core sizes (d_{CORE} = 2 – 10 nm) is accessible by varying the pH of the Au(III) solution[13,14] and keeping all other synthetic variables constant. This work aims to extend this size range by altering other reaction variables, specifically (1) flow rate, (2) ligand concentration, and (3) reducing agent concentration.

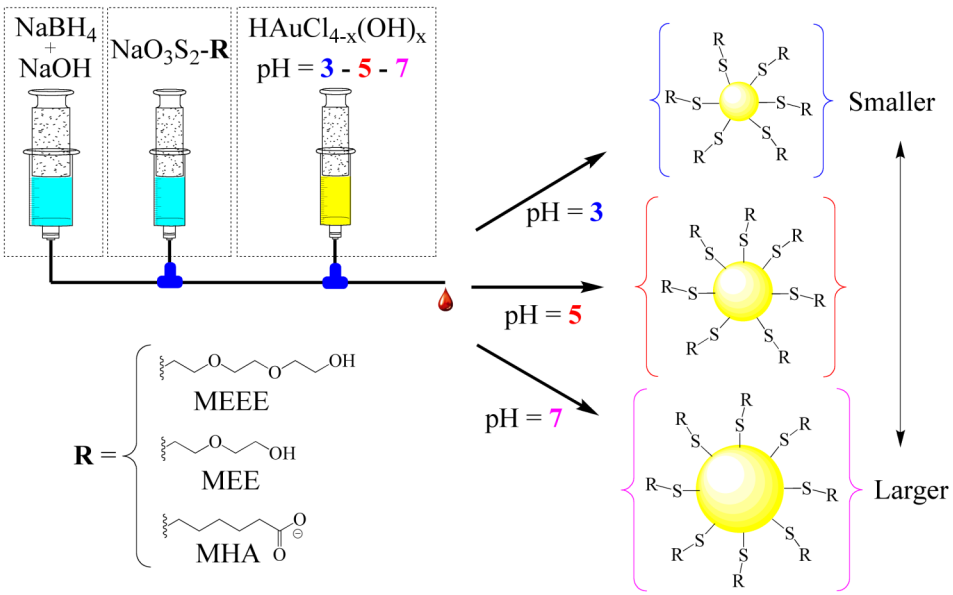

Figure 1. Microreactor setup to synthesize AuNPs with controlled core size and functionality. Size control afforded by tuning Au(III) pH accesses 2 – 10 nm AuNPs. Variation of other reaction parameters (flow rate, ligand concentration, and reducing agent concentration) is expected to extend this available size range.

The flow rate is hypothesized to affect AuNP core size by affecting the rate of reagent mixing in the microreactor.[20,21] Because AuNP reactions are very rapid, particles are already formed before the precursor reagents have mixed completely.[22,23] Faster mixing results in a greater apparent concentration of $NaBH_4$ with respect to Au(III) during AuNP formation. This increase in apparent concentration is expected to produce more growing nuclei during the early stages of NP formation, which leads to smaller final particles.[22] Conversely, lower flow rates are expected to result in larger core sizes. Since the synthetic method developed previously used the maximum flow rate available to the microreactor, the flow rate can only be lowered to access larger AuNP core sizes.

Ligand concentration is expected to affect AuNP core size through varying the kinetics of passivation during particle growth.[24] Raising the ligand concentration is expected to decrease AuNP core size by increasing the rate of passivation. Conversely, lowering the ligand concentration is expected to increase core size.

Reducing agent concentration is expected to affect AuNP core size by altering the rate of Au(III) reduction.[24] An increased rate of reduction is hypothesized to result in a higher rate of AuNP formation, and thus a larger number of growing nuclei. An increased number of nuclei should result in smaller AuNP core sizes. Therefore, a lower reducing agent concentration is then hypothesized to yield larger AuNP core sizes (assuming enough equivalents are present to reduce all of the Au(III)).

In this work, these three synthetic variables were probed to determine their effect on AuNP core size. Flow rate, ligand concentration, and reducing agent concentration were varied with the goal of maximizing the range of available sizes for the microfluidic synthetic method described in our previous work.[9] In the case of ligand and reducing agent concentration variables, hypotheses are based on previous observations in systems with strong passivants. It will be interesting to determine if these predictions hold for a system using Bunte salt ligands. Small-angle X-ray scattering (SAXS) was utilized as a precise and rapid method for determining AuNP size distributions.[25] Decreasing flow rate allowed access to larger AuNP sizes (up to 12 nm) while increasing ligand and reducing agent concentrations allowed access to smaller AuNP sizes (down to 1.5 nm).

Experimental

Materials and Analytical Methods

Hydrogen tetrachloroaurate hydrate ($HAuCl_4 \bullet xH_2O$, 99.9%) was purchased from Strem and used as received. Water used for syntheses was purified with a Barnstead NANOpure filtration system (18.2 MΩ resistivity). Bunte Salt ligands were prepared using known procedures,[24] or slight modifications thereof. Briefly, 1 molar equivalent of appropriate alkyl halide precursor was dissolved in nanopure water. Sodium thiosulfate (0.8 molar equivalents) was added and the solution was refluxed for 3 hours. Water was removed en vacuo, then the crude product was triturated with ethanol to remove salt impurities. All other reagents and solvents were purchased from Sigma-Aldrich or Macron Chemicals and used as received.

The nanoparticle sizes in solution were determined by SAXS. Details are provided in our recent publication.[25] Briefly, AuNP samples were analyzed as synthesized and exposed to monochromated X-rays from a Long Fine Focal spot (LFF) sealed X-ray tube (Cu 1.54 Å) powered by a generator at 2 kW focused by multilayer optics, measured with a Roper CCD in a Kratky camera. The Anton Paar SAXSess, in line collimation mode, was set to average 50 scans of 20 sec for all samples. The corresponding dark current and background scans were subtracted from the data before desmearing was performed using the beam profile in Anton Paar SAXSQuant software. The desmeared data were imported to IGOR Pro (v. 6.22A) software for modeling with third-party macros. The size distribution of the sample was determined by using the Modeling II macros in the IRENA package (v. 2.49). [26] The SAXS patterns were fitted using least-squares fitting

(LSQF), a size distribution model, a spheroidal form factor (Aspect Ratio = 1), a Gaussian distribution, and a dilute system (Structure Factor = 1). For each sample, reported polydispersity and average core size values were determined through optimization of volume, mean size, and distribution width values to produce the lowest χ^2 value for the model fit to the data.

All AuNP samples were analyzed by UV/visible spectroscopy (Ocean Optics) for determination of particle concentration and qualitative determination of particle stability. Ligand precursors and final Bunte Salt products were analyzed by ^{1}H NMR (300 MHz, Varian). For XPS analysis, excess ligand and salts were removed from solution by diafiltration using a 5 kDa membrane (Pall).[11] XPS spectra were taken at 20 eV pass energy on a ThermoFisher ESCALab 250 with a monochromated Al K-alpha, using a 400 μm spot size. Spectra were corrected to aliphatic carbon at 84.95 eV. Peak fitting was performed using ThermoFisher Avantage software.

Batch AuNP Syntheses

All glassware and stir bars were cleaned with aqua regia, rinsed with nanopure water, and dried before synthesis. Stir rates were kept low, at ~ 200 rpm. Syntheses were performed according to the pH-dependent size-controlled method developed in our previous work.[9] Briefly, the particles were synthesized in 80 mL batches using 250 mL round bottom flasks. Nanopure water (39.05 mL) was added to the flask first. The appropriate amount of 1.0 M NaOH (0.46 mL) was added to the stirring flask. The MEEE Bunte Salt (0.56 mg) was prepared in a centrifuge tube to produce 20 mL of a 1.0

mM solution from. The $HAuCl_4$ (20 mL of 5.0 mM solution, 34 mg) was prepared in a separate centrifuge tube and an appropriate amount of 1.0 M NaOH was added to this solution to adjust the Au salt solution pH to ~ 3 and ~ 7, respectively (0.08 mL to result in Au(III) pH =3). Approximately 15 min were allowed for this solution to reach equilibrium. A 0.10 M solution of $NaBH_4$ was prepared and 0.40 mL was added to the stirring round bottom flask. The MEEE Bunte Salt solution was then added to the stirring flask. ~ 20 second were allowed for equilibration, then the pH-adjusted $HAuCl_4$ solution was added rapidly to the stirring flask. An immediate color change was observed.

Microfluidic AuNP Syntheses

Syntheses were performed according to the pH-dependent size-controlled method developed in our previous work.[9] Three syringe pumps each equipped with 3-way distribution valves were purchased from Kloehn (Versa 6, 48k model with rotary valve). All other microreactor components were purchased from IDEX Health and Science. FEP tubing (1/16" outer diameter, 0.030" inner diameter), T-mixers (1/16", 1/4-28, 0.020" Thru, ETFE), 15 psig check valves, and appropriate fittings (1/4-28) and ferrules were assembled with the syringe pumps as shown to enable microfluidic generation of AuNPs. Tubing and T-mixers were swapped out if material deposition occurred. Solutions were pumped at a total flow rate of 60 mL/min, with tubing lengths selected to allow for sufficient mixing time in the microfluidic system.

Aqueous solutions were prepared to enable three successive microfluidic syntheses

at each reaction condition. Thus, 30 mL of 5.0 mM $HAuCl_4$, 30 mL of 1.0 mM Bunte Salt ligand, and 60 mL of 1.0 mM $NaBH_4$ were prepared. A total of 0.825 mL of 1.0 M NaOH was added to these solutions, split between the $HAuCl_4$ and $NaBH_4$ solutions. The desired amount of NaOH (ranging from 0.127 mL – 0.510 mL) was first added to the $HAuCl_4$ solution, determining the initial Au(III) speciation and effectively controlling the final AuNP dimensions. Corresponding Au(III) pH values and added volumes of NaOH are summarized in Table 1. The remaining amount of total NaOH (ranging from 0.698 mL – 0.315 mL) was added to the $NaBH_4$ solution to maintain final pH of the system. It is advantageous to prepare the $HAuCl_4$ solution first, as it can take up to 15 min to reach equilibrium at high pH. Additionally, the $NaBH_4$ solution should be prepared last, as this reagent also undergoes undesirable hydrolysis in water, albeit slowly.[14] Note that 0.125 mL of additional 1.0 M NaOH was added to the 30 mL of 1.0 mM MHA ligand solution to ensure the acid group was deprotonated at all conditions (a total of 0.837 mL base).

Table 1. Summary of NaOH volumes added to precursor solutions to tune Au(III) pH and achieve AuNP size selectivity.

Au(III) pH	Au(III) pH Abbreviation	1M NaOH added to $HAuCl_4$ solution (mL)	1M NaOH added to $NaBH_4$ solution (mL)
2.97	~ 3	0.127	0.698
3.93	~ 4	0.225	0.600
4.90	~ 5	0.325	0.502
5.87	~ 6	0.420	0.405
6.76	~ 7	0.510	0.315

Once the appropriate amount of base was added to the respective solutions, each of the three solutions was aspirated by the three syringe pumps as shown in Figure 1. The 20 mL of $NaBH_4$ solution was dispensed at 30 mL/min, mixed with a stream of 10 mL of ligand solution flowing at 15 mL/min, mixed along a 1.64 m length of tubing (1 second of residence time), before introducing the third stream of 10 mL of Au(III) solution flowing at 15 mL/min. Two simple T-mixers were used to mix the reagents. 15 psig check valves were utilized at each of the 10 mL syringes to avoid backflow. At a total flow rate of 60 mL/min, the final mixed solution is allowed to flow through the reactor for ~ 2 seconds (~ 5 m of tubing) before being collected. Small fractions at the beginning and end of each reaction were discarded. The microreactor system was rinsed with nanopure water three times (full aspirate/dispense cycles of the syringe pumps) after each synthesis. Each synthesis was repeated another two times, using the remainder of the prepared solutions, to determine reproducibility. After each set of three syntheses, the downstream T-mixer that introduces the $HAuCl_4$ solution was replaced with a clean mixer. The used mixers are later cleaned with aqua regia and water to remove any plated Au material left behind. If any plated material was evident in the reactor tubing, it was discarded and replaced with fresh tubing.

Results and Discussion

The flow rate within the microreactor was the first variable investigated in attempts to extend the available AuNP size range for the synthetic method of interest. Using a 1 : 5 : 2 ratio of MEEE Bunte salt / Au(III) / $NaBH_4$, a series of particles were

synthesized with the Au(III) solution pH set to 5 using different flow rates (3 – 60 mL/min) in the microreactor (Figure 2). Tubing lengths were adjusted for each flow rate to maintain identical residence times in the reactor. Small-angle X-ray scattering (SAXS) size analysis was utilized to determine AuNP size distributions.[25,27] Comparing the AuNP sizes produced across the range of flow rates reveals that a threshold exists at ~ 20 mL/min. Decreasing flow rate below this threshold results in larger AuNPs. Increasing flow rates above 20 mL/min results in no significant change in size distribution. This suggests that at this threshold, the rate of mixing is on the order of AuNP formation. Decreasing the flow rate results in slower mixing than NP formation, while raising the flow rate maintains efficient mixing and has little impact on the final products.

The threshold that exists at 20 mL/min is indicative of where mixing efficiency matches the rate of AuNP formation in this synthetic system. Based upon simple calculations for a T-mixer in a microreactor system, fully turbulent mixing doesn't occur until ~ 60 mL/min, with higher flow rates showing similar turbulent mixing. In this case, turbulence is desirable because the individual reagents become completely mixed, creating homogeneous conditions.[28] Below this flow rate, a mixing regime referred to as chaotic advection occurs.[28] In this regime, complex flow patterns cross and mix reagents over different durations, depending on the flow conditions. This type of mixing occurs more slowly than true turbulent mixing, but reagent mixing reaches equilibrium on the millisecond time scale for small volumes.[28]

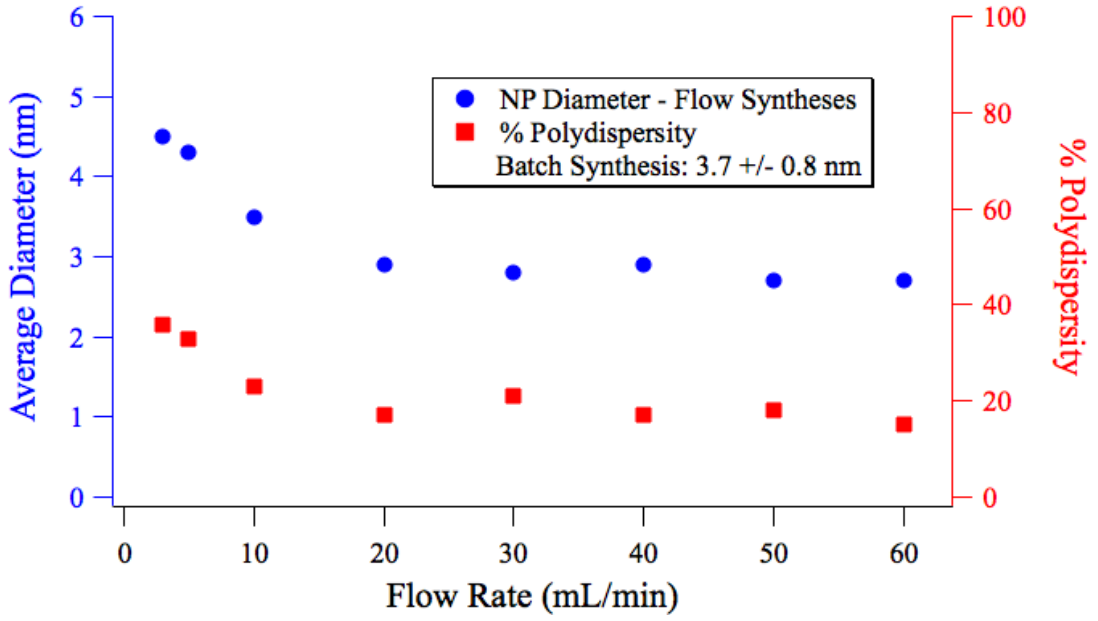

Figure 2. Compiled SAXS data for AuNP syntheses performed with pH of Au(III) solution set to 5. Flow rate was varied from 3 – 60 mL/min and a batch synthesis was included for comparison. Below 20 mL/min, there is a significant impact of flow rate on AuNP size distribution where lower flow rates result in larger AuNPs. Above 20 mL/min, there is little change in size distributions with increased flow rate. Polydispersity scales proportionally to core diameter across these data. Values for a corresponding batch synthesis of AuNPs are shown for comparison: 3.7 +/- 0.8 nm (21% polydispersity).

Calculations for the system used in this study suggests that chaotic advection dominates from 20 – 60 mL/min. Below 20 mL/min, laminar flow dominates, where the two incoming streams do not combine upon mixing, but rather flow along the tubing parallel to one another. Mixing in this scenario occurs more slowly, through diffusion between the parallel flow paths.[28] We observe a clear size dependence on flow rate in this regime. This suggests reaching the rate of mixing in the chaotic advection regime (20 –

60 mL/min for this system) is sufficient to reach homogeneous conditions before AuNP formation has occurred. However, the size dependence observed at lower flow rates suggests that the reagent mixing reaches homogeneity more slowly than NP formation. Although larger NPs can be produced at these flow rates, this scenario is generally undesirable, as evidenced by the increase in polydispersity.

Having investigated flow rate at a specific pH for the Au(III) solution, we sought determine how flow rate affects AuNP size using a series of pH values. Thus, plots of size as a function of pH were generated according to the previously developed synthetic method at 5, 20, and 60 mL/min flow conditions, along with a set of analogous batch conditions for comparison (Figure 3). Results followed the overall trend observed in Figure 2, with 5 mL/min conditions resulting in the largest particles across all pH values (for the investigated flow rates). Batch conditions resulted in slightly smaller AuNP sizes across this range, while 20 and 60 mL/min conditions resulted in almost identical trends, having the smallest observed core sizes at all pH values. This suggests that the effect of flow rate (and thus mixing) is independent from the pH of the Au(III) solution.

The flow rates investigated facilitate synthesis of AuNPs up to ~12 nm diameters, extending the accessible size range available trough this synthetic method. This increased level of control over size is advantageous; however, polydispersities are observed to increase proportionally with increased core size. In addition, reducing the flow rate necessarily decreases reaction throughput. Thus, the increased size range comes at the cost of increased polydispersity and decreased reaction throughput.

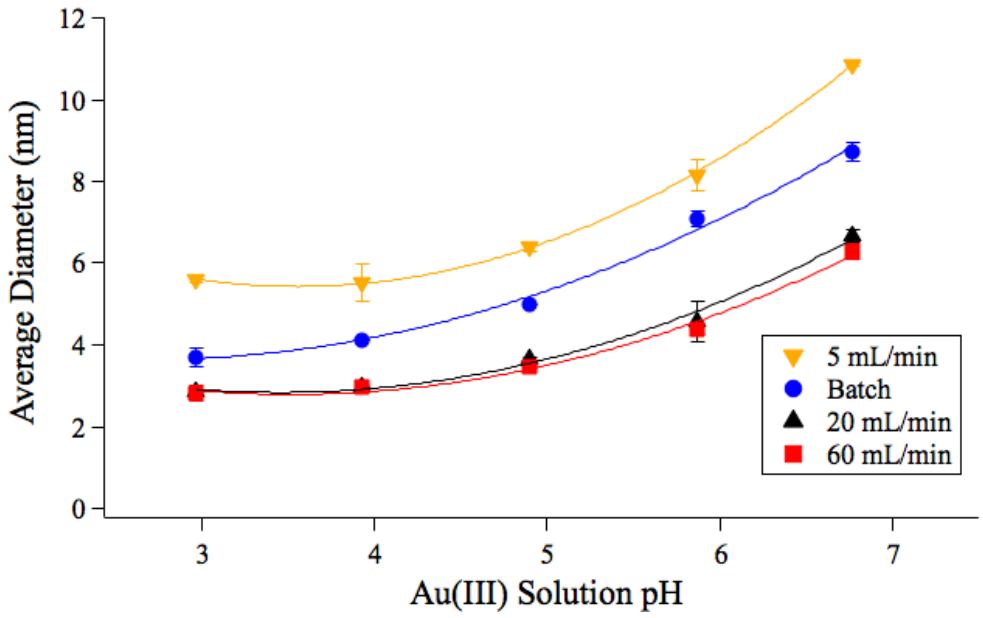

Figure 3. Compiled SAXS data, showing 4 different plots of AuNP size vs. pH of the Au(III) solution where each trace represents different mixing conditions. Three traces (5, 20, 60 mL/min) were generated through microfluidic syntheses using varied flow rates, and a data series generated from batch conditions are shown for comparison. The varied mixing conditions for each series results in a different window of accessible sizes. Faster mixing results in smaller AuNPs at all pH values, while slower mixing results in larger AuNPs. Flow rates of 20 mL/min and 60 mL/min yield virtually identical size trends, suggesting that a threshold is reached where increasing flow rate further has no appreciable effect. Notably, batch conditions result in smaller AuNPs than 5 mL/min conditions at all pH values (as in Figure 2), suggesting mixing is faster in batch than at 5 mL/min conditions. Given that 5 mL/min flow rates are known to result in laminar flow in this system, this is not surprising that batch conditions can achieve more rapid mixing. Each data point is obtained by averaging the determined core size from three different syntheses.

While decreasing flow rate is a useful strategy to increase AuNP core diameters, methods are still needed to access smaller sizes. We hypothesized that varying ligand concentration and reducing agent concentration would facilitate access to smaller AuNPs than had been possible with the standard reaction conditions.[24] Thus, two series of AuNPs were synthesized to probe the effect of (1) ligand concentration and (2) reducing agent concentration, using batch conditions with pH of the Au(III) solution set to 5.

The MEEE Bunte salt concentration was varied from 0.002 – 1 equivalents with respect to Au to determine the effect on AuNP size distribution (Figure 4). As ligand concentration was increased, a decrease in core size was observed along with a slight drop in polydispersity. The decrease in size is attributed to an increase in the rate of passivation.[24,29]

In parallel experiments to the ligand concentration study, the $NaBH_4$ concentration was varied for a series of AuNP syntheses (Figure 5). $NaBH_4$ concentration was varied from 0.1 – 5 mM (0.02 – 2 equivalents with respect to Au) to determine the effect on AuNP size distribution. As $NaBH_4$ concentration is increased, a modest decrease in AuNP size is observed, while polydispersity remains roughly constant. This decrease in size is attributed to an increased rate of particle nucleation and a higher final AuNP concentration.[24,30]

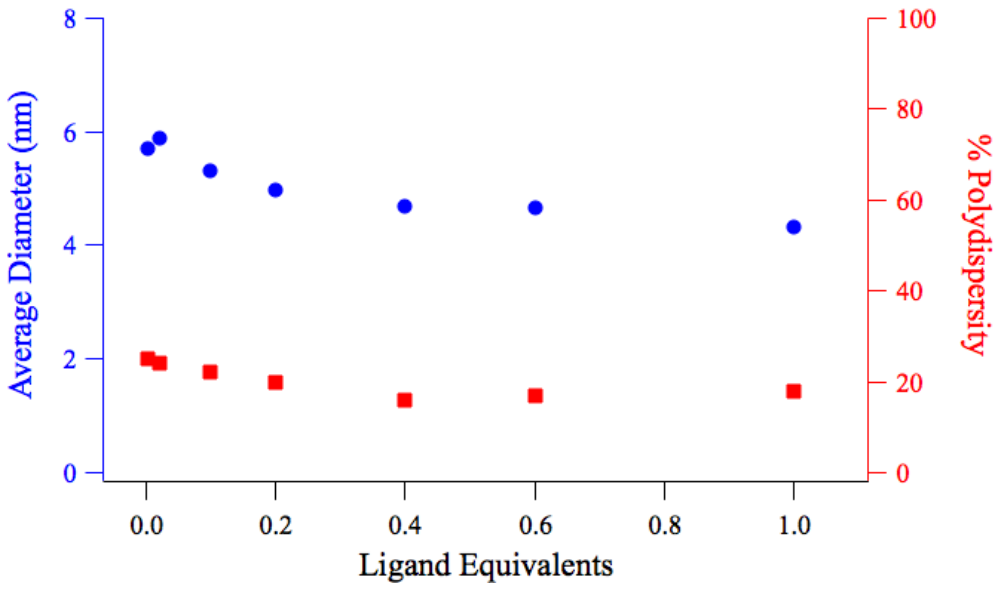

Figure 4. SAXS data showing AuNP batch syntheses, with pH of the Au(III) solution set to 5, using varied MEEE Bunte salt concentrations. Increased ligand concentration results in decreased particle size due to increased rate of passivation during NP growth. These experiments preceded the development of the microfluidic synthesis, and were thus performed in batch.

While we observe a modest effect of reducing agent concentration on AuNP size, we might expect this effect to be more prominent. Only ~ 1 nm difference in AuNP size is observed across the investigated range, excluding data points with incomplete reduction. While a distinct lower threshold exists for reducing agent equivalents, these data show no indication of an upper threshold. Thus, it is possible that even smaller AuNP sizes can be accessed by a further increase in reducing agent concentration.

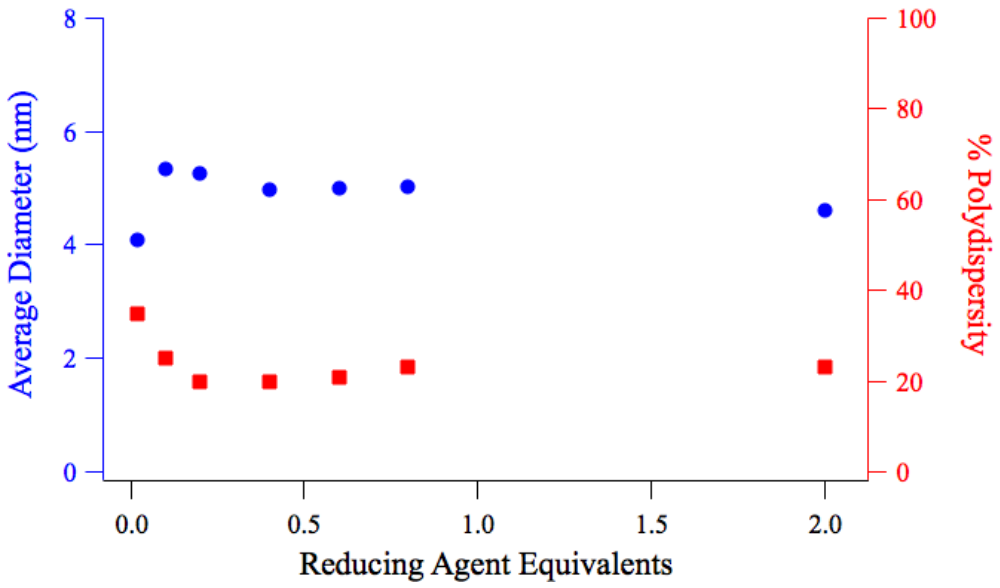

Figure 5. SAXS data showing AuNP batch syntheses, at Au(III) pH = 5, using varied $NaBH_4$ concentrations. Increased reducing agent concentration results in a higher rate of particle nucleation. The higher concentration of AuNPs results in smaller final core sizes. These experiments preceded the development of the microfluidic synthesis, and were thus performed in batch.

Given that increased ligand concentration and reducing agent concentration result in smaller AuNP sizes, we sought to produce the smallest possible AuNPs using microfluidic synthesis. To accomplish this, we utilized high flow rates (60 mL/min), and low pH of the Au(III) solution. The MHA Bunte salt was used because previous studies demonstrated that this ligand provides the smallest core sizes of those investigated.[9] From the standard 1 : 5 : 2 ratio of Bunte salt / Au(III) / $NaBH_4$, we increased the concentration of each reagent, to maximize the rate of passivation, minimize the pH of the Au(III) solution, and maximize the rate of nucleation. A series of experiments varying each individual reagent concentration were performed to optimize reaction conditions and

minimize AuNP core size. These studies show that a 10 : 7 : 10 ratio (of Bunte salt / Au(III) / $NaBH_4$) produces 1.5 nm AuNP cores (Figure 6).

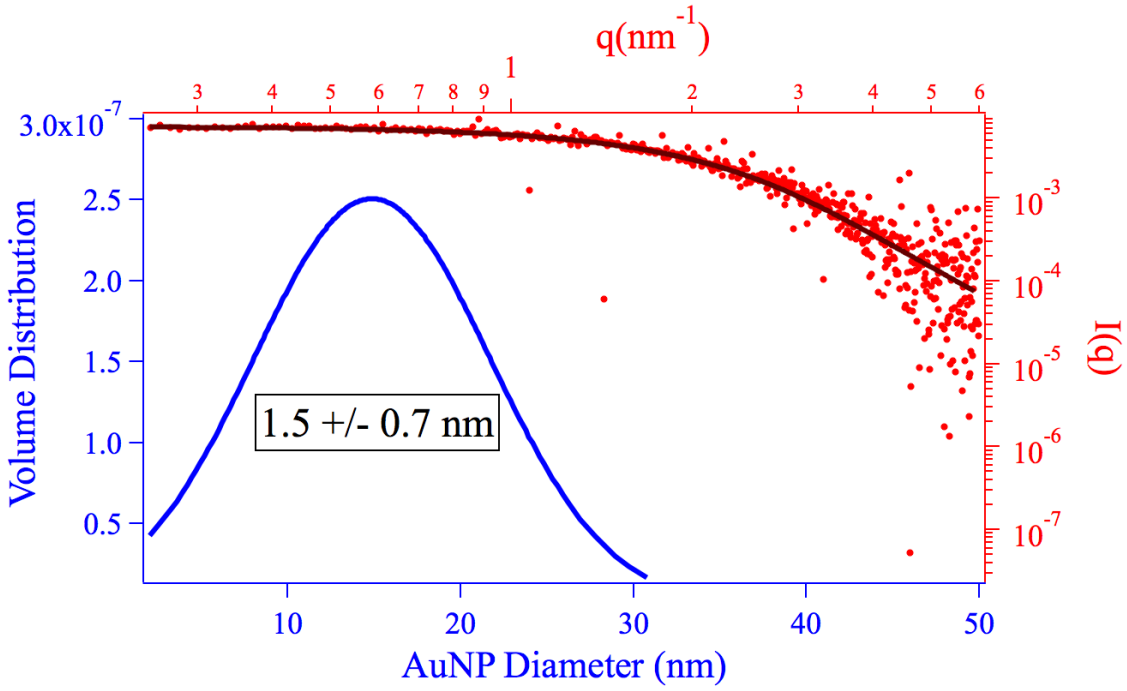

Figure 6. SAXS data showing modeled scattering pattern (red) and output size distribution (blue) of 1.5 nm AuNPs functionalized with MHA Bunte salt. These AuNPs are remarkable because they were directly synthesized in high yield with no post-synthetic washes. This represents a greener route to this size of functionalized AuNPs than previous methods.[10]

The synthetic method shown here accesses 1.5 nm AuNPs more efficiently than previous methods. Previous syntheses of this size of AuNP required lengthy reaction times, copious washes, and post-synthetic ligand exchange to achieve functionalized particles.[1,2,10,31] This direct synthetic method both improves total yield and reduces the number of synthetic steps required to access these materials. However, XPS analysis reveals that these particles are passivated by both oxidized and reduced sulfur-containing species (Figure 7).

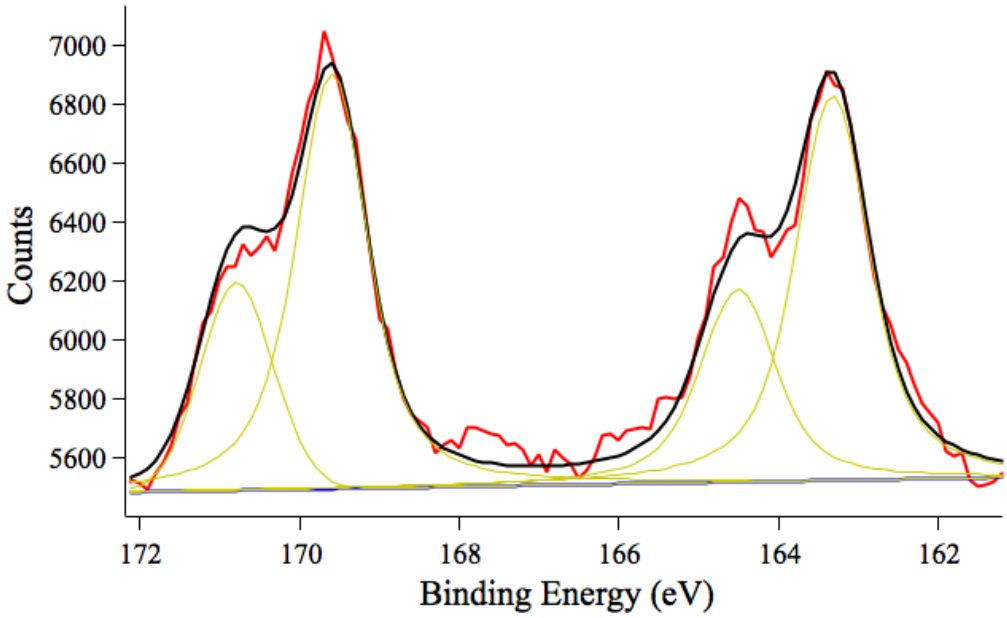

Figure 7. XPS data of the S2p region for the 1.5 nm MHA-stabilized AuNPs. Two distinct species are observed. The species at ~163 eV corresponds to bound thiolate on the AuNP surface, while the species at ~169 eV corresponds to strongly-adsorbed Bunte salt species. Peak integration suggests that ~50% of the ligands on the AuNP surface are thiolate, and ~50% are Bunte salt. Diafiltration was performed to remove excess ligands.[11,12]

XPS analysis of the 1.5 nm AuNPs revealed that ~50% of the ligand shell is comprised of bound thiolate species while the other ~50% is comprised of Bunte salt species. Because this sample was diafiltered, the Bunte salt species must be strongly associated with the particles.[11] It is not clear whether or not the thiosulfate functionality is adsorbed directly to the AuNP surface. Additional trials showed that the smallest particles synthesized through the described synthetic method that display complete thiolate monolayers are 1.9 nm (Figure 8). It is possible that reaction conditions can be further optimized to achieve complete conversion of Bunte salt to thiolate for 1.5 nm AuNPs, but this has not yet been demonstrated.

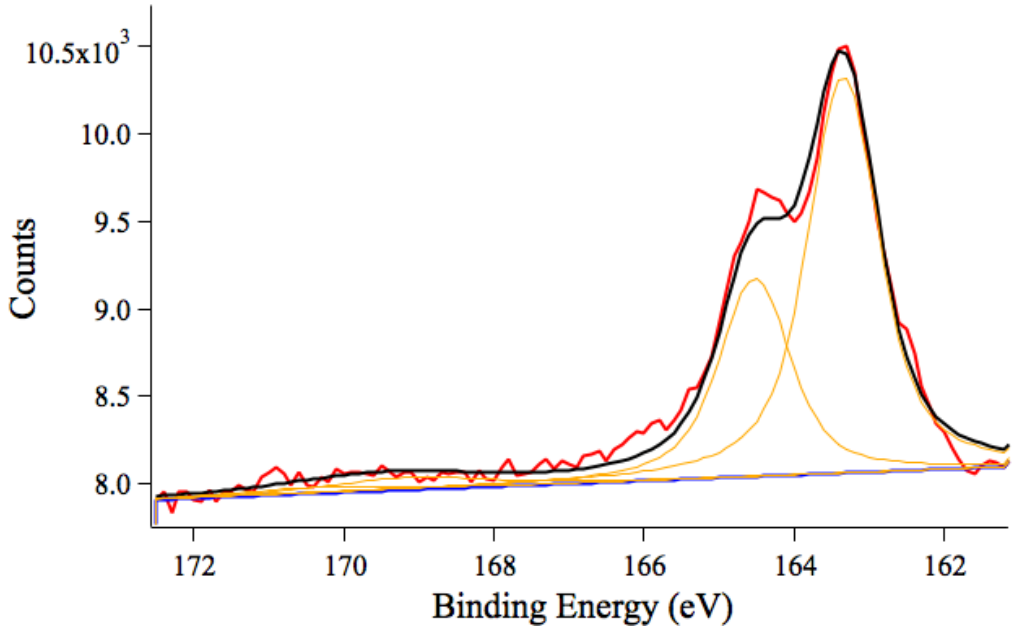

Figure 8. XPS data of the S2p region for the 1.9 nm MHA-stabilized AuNPs. This XPS spectrum shows ~ 95% of the sulfur species are bound to the AuNP surface through thiolate linkages, while only trace Bunte salt is observed. Diafiltration was performed to remove excess ligands.[11,12]

The observed disparity between the surface chemistry of 1.5 and 1.9 nm AuNPs could arise for a number of reasons, and may not be due simply to size differences. It could be that a high enough radius of curvature facilitates interdigitation of ligands, retaining unreduced Bunte salt in the ligand shell. This seems unlikely because the extensive purification of these samples should remove any excess ligand. Another possibility is the initial solubility of the Bunte salt ligand. In the 1.5 nm synthesis, the ligand solution was cloudy and required sonication to prevent precipitation. In the case of the 1.9 nm synthesis, a new batch of ligand had been synthesized and the ligand solution was clear upon synthesis. The difference between these is likely the amount of residual NaBr salt left in the ligand. Thus, the cloudy solution may have simply resulted in more oxidized sulfur due to the poor solubility, though smaller sizes were reached due to the higher effective concentration of ligand. Reaching 1.5 nm AuNPs with fully reduced ligand shells will likely require the maximum possible concentration of ligand while maintaining solubility. Future efforts should be directed at generating a supersaturated ligand solution by heating the solvent, dissolving the ligand in as high a concentration as possible, and then allowing the solution to return to room temperature before use in synthesis.

Conclusion

In this work, we have shown the ability to extend the available size range for the microfluidic synthetic method described in our previous work.[9] Decreasing flow rate provided access to larger (> 10 nm) AuNPs while increasing the ligand and reducing agent concentrations provided access to smaller (< 2 nm) AuNPs. Studying the effect of

these reaction conditions has expanded the utility of this synthetic method, providing the ability to synthesize ~ 1.5 – 12 nm AuNPs with controlled core size and desired functionality.

Bridge to Chapter V

Chapter IV demonstrated that, through tuning of several synthetic variables, the new synthetic method developed in Chapter III can access a wider range of sizes than was originally possible with only Au(III) solution pH variation. It is interesting, however, that AuNP growth using Bunte salts shows significant differences from thiol ligands. We still desired a deeper understanding of the AuNP reaction chemistry using Bunte salts.

First, we needed to understand which techniques are best equipped to probe complex AuNP distributions. With the intent of investigating AuNP formation processes, four workhorse techniques are compared in Chapter V. In this next chapter, three well-characterized reference materials are used to compare each technique's ability to identify binary and ternary mixtures of these materials.

CHAPTER V

EXAMINING CHARACTERIZATION METHODS TO RESOLVE MULTIPLE GOLD NANOPARTICLE DISTRIBUTIONS IN BINARY AND TERNARY MIXTURES

Introduction

Nanoparticles (NPs) have well known, interesting size-dependent properties.[1-3] Gold nanoparticles (AuNPs), for example, have size-dependent properties that are useful for a variety of applications.[4-7] The strong dependence of these properties on the diameter of the particles makes analytical determination of particle size of crucial importance for several reasons.[8,9] First, understanding how NP size varies with changes in synthetic parameters helps to guide future syntheses and realize optimal reaction conditions to produce materials with well-defined properties.[8,10] Second, the ability to precisely determine size is central to identifying structure-activity relationships for these materials.[9,11,12] Third, determination of NP size distributions is necessary to achieve quality control for the materials and assure that the particles behave similarly from batch-to-batch.[13] Lastly, size determination is needed to observe any variation in particle dimensions during transformations of the material.[11] In all, accurate size determination is as important as synthesizing the NPs.[13]

Despite the importance of NP size determination, it has not been clear which analytical technique is optimal to achieve this. While microscopy has historically been the standard method to obtain core size measurements for NPs,[14,15] this analysis is limited because it is time-consuming, prone to deposition artifacts, and can only access low

particle counts to determine size distributions. A number of other techniques have become more prominent over the last decade. These techniques have varying degrees of usefulness for day-to-day NP characterization. In this work, we briefly review all major NP size-determination techniques, then evaluate and compare four workhorse techniques, with respect to routine NP analysis, using a set of ligand-stabilized AuNPs as reference materials.

The six major techniques for NP size analysis that will be discussed herein are: (1) transmission electron microscopy (TEM), (2) UV/visible spectroscopy (UV/vis), (3) dynamic light scattering (DLS), (4) small-angle X-ray scattering (SAXS), (5) diffusion-ordered spectroscopy (DOSY), and (6) analytical ultracentrifugation (AUC). Each technique is compared and evaluated based on access to a large range of particle sizes (d_{CORE} = 0 – 30 nm), reproducible size analysis, and rapid characterization. Techniques that are impractical for routine analysis of a range of particle sizes are briefly reviewed, while potential workhorse techniques are experimentally evaluated using AuNP reference materials.

Transmission electron microscopy (TEM) is a straightforward technique where particles are directly visualized by exposure to an electron beam and differences in contrast between the particles and the substrate allow the particles to be observed.[16] Multiple images are collected and processed to obtain sufficient particle counts and generate a distribution histogram. TEM has traditionally been considered the standard technique for NP size determination because it provides the ability to directly visualize particles and generate unambiguous size distribution results. In addition, morphology information is easily obtained for NP samples.[17] TEM is limited, however, by low

statistical counts of particles (100's – 1000's), which can result in noisy histogram data or overlooked distributions.[13] The advent of image processing software[18] has reduced the time commitment required to process these data, but particle counts are still limited. Further, there are often deposition artifacts that result in larger apparent particle sizes.[19] This has been mitigated by improved TEM grid fabrication (e.g.; Dune Smart Grids[3]), though these artifacts are still a common issue. Despite improvements to data collection and processing, TEM analysis is still time-consuming, hindered by low statistics, and presents a high chance for researcher bias because images are chosen deliberately on the sample grid.[19,20]

UV/visible spectroscopy (UV/vis) is a ubiquitous optical technique where wavelength-dependent absorbance is measured.[21,22] Estimation of particle size can be achieved with this technique if a distinct, size-dependent optical signature can be measured. However, the size distribution of some materials cannot be determined with this technique. AuNPs have observable absorbance across the UV/visible spectrum, and particles with $d_{CORE} > 3$ nm have a distinct plasmon absorbance at ~ 520 nm. Literature comparisons between UV/vis and TEM measurements have led to an empirical relationship between the two techniques.[21] This empirical relationship allows particle size to be estimated in solution through determining the ratio of absorbance at 450 nm and the plasmon absorption maximum. This analysis is rapid, but the literature trend is only shown to be valid for 5 – 50 nm AuNPs.[21]

Dynamic light scattering (DLS) measures scattering of visible light in a solution of dissolved nanoparticles.[23] A laser probes a sample solution where particles are undergoing Brownian motion. A detector records the time-dependent fluctuations of the

light scattering. Smaller particles fluctuate more quickly and larger particles fluctuate more slowly based on their relative rates of diffusion. A correlation function is applied to the raw data and a series of modeling steps (often automated) extract particle size, polydispersity, and relative mass if other distributions are observable.[24] This technique is advantageous because hydrodynamic size distributions are determined rapidly in solution[25] and minimal expertise is required to run the instrument. However, drawbacks to this technique include high sensitivity to solution conditions (i.e., total concentration, ionic strength, minor dust impurities), questionable accuracy for particles with $d_{CORE} < 20$ nm, and a limited ability to optimize modeling of the data through control of software variables.[13,24,26]

Small angle X-ray scattering (SAXS) utilizes a focused beam of X-rays passed through a sample to determine particle dimensions.[27] The intensity and angles at which X-rays are scattered by the sample are characteristic of the size, shape, polydispersity, and concentration of the particles in the sample.[27] Plots of scattering intensity vs. scattering vector are modeled to extract the relevant NP parameters. Both solid and liquid samples can be quantitatively analyzed, though analysis in solution is preferable for colloidal species because deposition artifacts are avoided.[19] This technique does, however, require some expertise to model the data and determine these values. In addition, data collection times can be lengthy for samples with low signal-to-noise, though researchers need not be present for this process. SAXS had traditionally been confined to synchrotron sources to generate sufficient flux of X-rays for analysis.[28,29] Advances in lab-scale X-ray sources in recent years have increased the accessibility of this technique.[28,30]

DOSY is an NMR-based technique that measures how quickly an analyte diffuses through a magnetic gradient.[15,31,32] Larger analytes have slower diffusion rates, providing a means for determining the hydrodynamic radius of particles in solution. This technique is advantageous because it is non-destructive, can detect multiple species simultaneously, and is relatively rapid to perform.[33] Disadvantages to DOSY include the need to correct for solution viscosity, and the need for discrete NMR signals, which requires very high concentrations.[33] Because NPs over $d_{CORE} \sim 3$ nm do not exhibit strong NMR signals, this technique is highly limited in the sizes of particles and types of ligands that can be analyzed.[33] Thus, DOSY is only useful for a small subset of NPs, and cannot be considered a workhorse method.

Analytical ultracentrifugation (AUC) is a fractionation technique that can measure the sedimentation coefficient and/or diffusion coefficient of colloids.[34-36] These data can be collected using a variety of experimental setups to determine NP size, polydispersity, concentration, shape, molar mass, and density.[34] However, considerable modeling is required to extract these relevant parameters from the raw data.[35] This modeling is non-trival and is computationally intensive due to AUC's sensitivity to many solvent and solute variables.[35] NPs in particular have several characteristics making them particularly challenging to analyze with AUC: (1) size polydispersity results in sedimentation polydispersity, often making small volumes of large AuNPs or other small impurities unobservable, (2) particles can aggregate during sedimentation, (3) the density of the particles is often unknown, hampering conversion of sedimentation coefficient to particle size, (4) particles stabilized by charge exhibit non-ideal sedimentation characteristics, (5) multiple-distribution samples are difficult to identify and differentiate, and (6) scattering

of the particles requires a further mathematical correction.[35] Overall, AUC is potentially powerful because so many sample variables can be probed, but it is challenging to account for the interdependence of these variables. Thus, AUC experiments, while useful for a specific research question or a unique sample, is not practical for day-to-day analysis of NPs.

Four workhorse methods are evaluated in this study: (1) small-angle X-ray scattering, (2) transmission electron microscopy, (3) dynamic light scattering, and (4) UV/visible spectroscopy. Each of these workhorse techniques has demonstrated utility for analyzing pure NP samples.[18,21,22,37] Literature reports have also compared size analysis between these techniques,[19,38,39] including one report by Roebben et al. that investigated DLS size analysis between various labs.[40] Yet, no study has compared the ability of these techniques to differentiate binary or ternary mixtures of particles. There is a need for a robust technique that can reliably model multiple distributions in solution. Researchers would ideally have access to a rapid technique, free from artifacts, that could determine if multiple mixtures of particle sizes were present in solution, and quantitatively determine the average core size, polydispersity, and relative volume of each distribution. The goal of this work is to evaluate the relative merits of the four listed workhorse methods with respect to their ability to differentiate binary and ternary mixtures of known reference materials.

Well-defined reference materials that maintain stability under a variety of conditions are needed for this study. In addition, each set of reference materials must have identical ligand shells to facilitate comparisons of core diameter and hydrodynamic diameter and ensure identical behavior for each material under various analytical

conditions. In addition, the need for a variety of sizes requires that materials be chosen where size-tunable syntheses are accessible.

This study focuses on ligand-stabilized AuNPs because of their stability and their utility in a variety of potential applications.[4,9,41-43] In addition, there are several well-known methods for producing AuNPs with tunable core sizes.[15,44-48] Polydispersities for these materials often range from 15 – 25%, making it challenging but possible to differentiate mixtures with different size distributions. Specifically, this study utilizes three AuNP samples with unique average diameters and identical mercaptoethoxyethoxyethanol Bunte salt (MEEE) ligand shells as reference materials. These ligands were chosen because AuNPs can be synthesized with a wide range of sizes where the particles exhibit long-term stability, as demonstrated previously.[49]

The four workhorse techniques are evaluated in their ability to analyze each of the three pure reference materials, the three corresponding binary mixtures, and a ternary mixture of these samples. The sample variables of interest are: (1) average particle diameter, (2) distribution polydispersity, and (3) relative volume of each mixed sample. In addition, each technique is evaluated for whether standard analytical procedures identify the multiple modes of mixed solutions in an automated fashion to facilitate future application of this analysis to unknown samples.

Experimental

Materials

Hydrogen tetrachloroaurate hydrate ($HAuCl_4 \bullet xH_2O$, 99.9%, Strem), sodium citrate dihydrate (Mallinckrodt), sodium hydroxide (Macron), sodium borohydride (Sigma

Aldrich) were purchased and used as received. Water used for aqueous syntheses was purified with a Barnstead NANOpure filtration system (18.2 MΩ resistivity). MEEE Bunte Salt ligand was prepared using known procedures.[50] Briefly, 1 molar equivalent of 2-[2-(2-chloroethoxy)-ethoxy]ethanol was dissolved in nanopure water. 0.8 molar equivalents of sodium thiosulfate were added and the solution was refluxed for 3 hours. Water was removed in vacuo, and the crude products were purified by dissolution in cold ethanol followed by gravity filtration.

Au Nanoparticle Synthesis

All glassware and stir bars were cleaned with aqua regia, rinsed with nanopure water, and dried before synthesis. Stir rates were kept low, at ~ 200 rpm.

Synthesis of Pure Reference Materials: 3 nm Sample A and 9 nm Sample B. All AuNPs were synthesized in batch reactions. Samples A and B were synthesized directly using the MEEE Bunte Salt. Syntheses were designed to yield core diameters of ~ 3 nm for Sample A and ~ 9 nm for Sample B. The difference in core size was achieved using the method described in previously,[49] where AuNP core size is controlled by pH-dependent Au(III) speciation in solution upon addition of reducing agent. Briefly, the particles were synthesized in 80 mL batches using 250 mL round bottom flasks. Nanopure water (39.05 mL) was added to the flask first. The appropriate amount of 1.0 M NaOH was added to the stirring flask (0.46 mL for Sample A synthesis; 0.21 mL for Sample B synthesis). The MEEE Bunte Salt (0.56 mg) was prepared in a centrifuge tube to produce 20 mL of a 1.0 mM solution from. The $HAuCl_4$ (20 mL of 5.0 mM solution, 34 mg) was prepared in a separate centrifuge tube and an appropriate amount of 1.0 M

NaOH was added to this solution to adjust the Au salt solution pH to ~ 3 and ~ 7, respectively (0.08 mL for the Sample A synthesis; 0.34 mL for Sample B synthesis). Approximately 15 min were allowed for this solution to reach equilibrium. A 0.10 M solution of $NaBH_4$ was prepared and 0.40 mL was added to the stirring round bottom flask. The MEEE Bunte Salt solution was then added to the stirring flask. ~ 20 second were allowed for equilibration, then the pH-adjusted $HAuCl_4$ solution was added rapidly to the stirring flask. An immediate color change was observed.

Synthesis of 15 nm Sample C. Sample C was prepared by using a modified Turkevich method from the literature[51] to produce AuNPs with ~ 15 nm diameter cores. Briefly, 99.0 mg of trisodium citrate was added to a three-neck 300 mL round bottom flask with 149 mL of nanopure H_2O and a stir bar. The solution was stirred vigorously and brought to reflux. A 25 mM aqueous solution of $HAuCl_4$ was heated to a low boil, then 1 mL of solution was added to the refluxing citrate solution. Color changed to grey immediately, then changed to red over 5 minutes, after which heat was removed. The solution was allowed to cool to room temperature over 3 hours while still stirring. The particles were passivated by MEEE Bunte salt via ligand exchange, where 10 mL of the as-synthesized citrate AuNPs were added to a separate flask and stirred vigorously and then 1.0 mL of 10 mM MEEE Bunte salt solution was added to the flask. The solution was allowed to stir for 10 hours, though exchange appears to be complete after ~ 30 min by UV/vis. Excess ligand was removed by diafiltration. This procedure for ligand exchange can be scaled up to larger batches as well. All AuNP samples were purified via diafiltration using a 75 kDa or 10kDa membrane (Pall) before analysis.[12]

AuNP Characterization

Each of the three reference AuNP samples was stable for long durations in solution (> 3 months) and stable to diafiltration.[12] Each was passivated with the mercaptoethoxyethoxyethanol Bunte salt (MEEE) during synthesis, which results in a mixture of thiolate linkages to the Au surface in addition to residual thiosulfate adsorbed to the surface. XPS analysis of S2p region (Appendix C) indicates the ratio between these two species, with bound thiolate appearing at ~ 163 eV and adsorbed thiosulfate appearing at ~169 eV. These XPS spectra indicate that no free ligand is left in the samples. Previous studies indicate that SAXS provides accurate determination of AuNP core size and polydispersity.[19] The SAXS core size distribution values for Samples A, B, and C were 3.1 ± 0.6 nm, 9.1 ± 1.9 nm, and 14.6 ± 2.2 nm, respectively.

SAXS Data Collection and Analysis. Details for nanoparticle size determination by SAXS are provided in our recent publication.[19] Briefly, AuNP samples were analyzed as synthesized and exposed to monochromated X-rays from a Long Fine Focal spot (LFF) sealed X-ray tube (Cu 1.54 Å) powered by a generator at 2 kW focused by multilayer optics, measured with a Roper CCD in a Kratky camera. The Anton Paar SAXSess, in line collimation mode, was set to average 50 scans of 80 sec for each sample. The corresponding dark current and background scans were subtracted from the data before desmearing was performed using the beam profile in Anton Paar SAXSQuant software. The desmeared data were imported to IGOR Pro (v. 6.22A) software for modeling. Initial estimates for the number of distributions, average diameters, and polydispersities were identified using the 'Size Distribution' software within the IRENA

macro (v. 2.49).[52] These estimated values were input into the 'Modeling 2' software within IRENA to determine quantitative values to be reported for each sample. The SAXS patterns were fitted using least-squares fitting (LSQF), a size distribution model, a spheroidal form factor (Aspect Ratio = 1), a Gaussian distribution, and a dilute system (Structure Factor = 1). For each sample, reported polydispersity and average core size values were determined through optimization of volume, mean size, and distribution width values to produce the lowest χ^2 value for the model fit to the data.

TEM Data Collection and Analysis. Transmission electron microscopy (TEM) was performed on an FEI Tecnai Spirit instrument, operating at 120kV accelerating voltage. Amine-functionalized SiO_2 Smart Grids (Dune Sciences) were used for all TEM analysis. TEM grids were prepared by aerosol spray deposition (two sprays for each sample grid) to ensure that no preferential adsorption of AuNPs occurred. The substrates were allowed to dry for 24 hours before analysis. TEM images were processed using Fiji software as discussed previously.[18]

DLS Data Collection and Analysis. DLS measurements were taken using a Mobiuζ instrument from Wyatt technologies. The samples were filtered using a 0.1 μm PTFE syringe filter to remove any particulate matter. Hydrodynamic diameters were calculated using Dynamics software and averaged over 20 measurements with 5 second integration time per acquisition.

UV/vis Data Collection and Analysis. An Ocean Optics UV/visible spectrometer was used to collect UV/vis data for these studies. The Spectrasuite software package was used to operate the spectrometer and view the data. A 1 cm

pathlength quartz cuvette was used to contain the sample solutions. Samples were diluted as necessary to obtain spectra.

XPS Data Collection and Analysis. XPS spectra were taken at 20 eV pass energy on a ThermoFisher ESCALab 250 with a monochromated Al K-alpha, using a 400 μm spot size. Spectra were corrected to Au 4f peak at 84.95 eV. Peak fitting was performed using ThermoFisher Avantage software.

Results and Discussion

Evaluation of Three Reference Materials

The reference materials were designed to have distinct average core diameters and modest polydispersities that result in partial overlap of the distributions. With the intention of later mixing these samples for analysis, the materials were synthesized to be challenging, but possible to differentiate in an equal-volume mixture. Each sample was diafiltered after synthesis to ensure that any excess ligand or salt species in solution were removed prior to analysis.[12] The reference samples were synthesized to have average diameters of ~3 nm, ~ 9 nm, and ~ 14 nm and 15 – 25% polydispersities (as determined by SAXS) for all of the experiments in this study. Each reference sample was functionalized with a neutral, water-soluble ligand: mercaptoethoxyethoxyethanol Bunte salt (MEEE).[50] Each sample used in this study was analyzed once with each technique using standard methodology and available software.

For SAXS measurements, each purified sample was analyzed in solution. After subtraction of the dark and water backgrounds using SAXSQuant software, the data were imported into the IGOR software. Then the IRENA macro was used with known

procedures to model the data and determine average diameter, polydispersity, and distribution volume values for each reference sample (Figure 1).[52] Within the IRENA macro, two programs are used sequentially to model the data. First, the Size Distribution program is used to identify the number of unique distributions within the data and give a rough estimate of the distribution parameters. These values are used as a starting point in the more rigorous program, Modeling II. This program quantitatively evaluates distribution parameters, but requires more information input. Fits in this program were optimized by minimizing reduced-χ^2 values. This two-step modeling process effectively identifies distributions, then applies quantitative models to extract size distribution parameters.

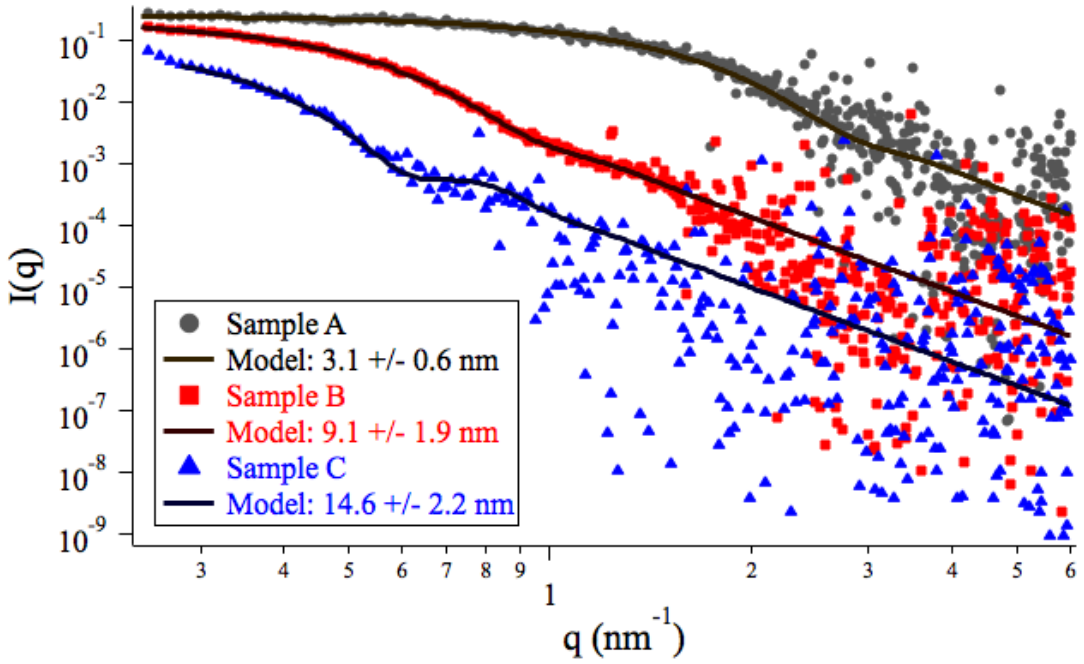

Figure 1. Modeled SAXS patterns for three reference samples used in this study. Imported data were binned logarithmically and modeled as such. An increase in the slope of the data at low q values corresponds to larger average AuNP sizes. Patterns are offset for clarity.

The SAXS measurements provided size distribution information rapidly. Reproducibility is high for these measurements, with confidence within 0.1 nm for core sizes. In all, we find that this is a highly reliable technique for measuring single distributions of particles in this size range.

For TEM measurements, each pure reference sample was deposited onto an amine-functionalized SiO_2 substrate using aerosol spray deposition.[53] Eight individual micrographs were captured for each sample at several magnifications on multiple grid windows. Each image was analyzed using known procedures to produce binary images where particle sizes were counted and a number distribution histogram was generated.[18] These number distribution histograms were converted to volume distribution histograms (Figure 2). These histograms were imported into IGOR v.6.31 software and were fitted to Gaussian distributions to determine average core size and polydispersity values for each reference sample. Bins with fewer than 5 particle counts on the periphery of each sample distribution were ignored for curve fitting.

TEM measurements, when performed with standard methodology, show similar average diameters to SAXS. Because of some observed rafting of particles (Appendix C), measured core sizes were slightly larger than SAXS values for Samples B and C. In addition, measured polydispersities from TEM data are typically larger than for SAXS measurements.[19] This has been attributed to the higher statistics and lack of deposition artifacts for SAXS measurements. Further, TEM data collection and processing are relatively time-consuming compared to SAXS.

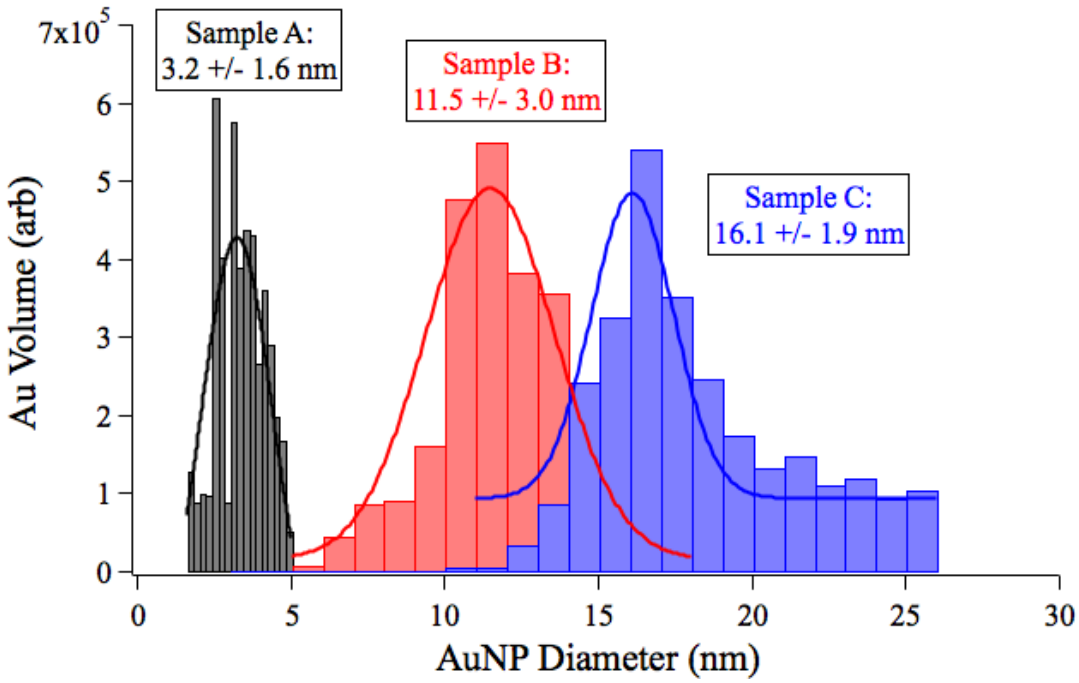

Figure 2. Overlaid histograms of the three individual reference samples used in this study. Each histogram was fitted to a Gaussian curve to determine average size and polydispersity. Listed polydispersities are one standard deviation from the average diameter. Note that the individual distributions of Samples B and C exhibit some overlap, and several of the larger diameter bins for Sample B are hidden behind those of Sample C.

For DLS measurements a beam of visible light (530 nm) is exposed to the sample solution. The light scattered off of particles in solution is monitored by a CCD detector. The DynaPro Dynamics software utilizes an autocorrelation function to fit the scattering data in real time, separating the random noise in the signal from the real fluctuations of the signal due to Brownian motion of the particles.[24] The software determines the rate of diffusion from these data, from which the hydrodynamic diameter of the particles is determined.[23] When multiple distributions are present the program outputs a normalized

intensity (displayed as % intensity), which indicates how much of the detected light is scattered from each particle distribution. Because larger particles will scatter more strongly, the program utilizes an algorithm to convert % intensity to % mass, based upon the observed intensity and the size of the particles.[24] During analysis of collected DLS data, peaks that exhibited a % intensity or % mass of less than 0.5% were ignored.

DLS analysis (Table 1) was very rapid, requiring only several minutes to collect the data. However, each of the three reference materials showed smaller values than would be expected from SAXS measurements of core size. Note that both techniques measure particle volume distributions. Subtracting the expected ligand shell thickness of ~1.5 nm (for the MEEE ligand) from DLS measurement of hydrodynamic diameter, the analyses showed smaller core sizes of Sample A by ~ 50%, Sample B by ~ 20%, and Sample C by 4% compared to SAXS measurements. While the value for Sample C is reasonable, the collective data suggest that AuNPs < 14 nm in core diamter are too small to accurately measure by DLS.

Table 1. DLS data for each of the three reference samples used in this study

Sample	DLS Size Distribution	Calculated DLS Core Diameter [a]
Sample A	4.4 ± 0.4 nm	1.4 nm
Sample B	10.2 ± 1.5 nm	7.2 nm
Sample C	17.0 ± 1.9 nm	14.0 nm

a - Expected ligand shell thickness is ~1.5 nm for all three pure samples

For UV/vis measurements (Figure 3), data were collected in a standard 1 cm path length cuvette. Size analysis was achieved by observing the absorbance values at 450 nm (A_{450}) and at the AuNP plasmon lambda-max (A_{SPR}). These values were input into Equation 1, taken from Haiss et al.[21] to determine AuNP core diameter (d_{CORE}).

$$d_{CORE} = EXP(3.00*(A_{SPR}/A_{450}) - 2.20) \quad (1)$$

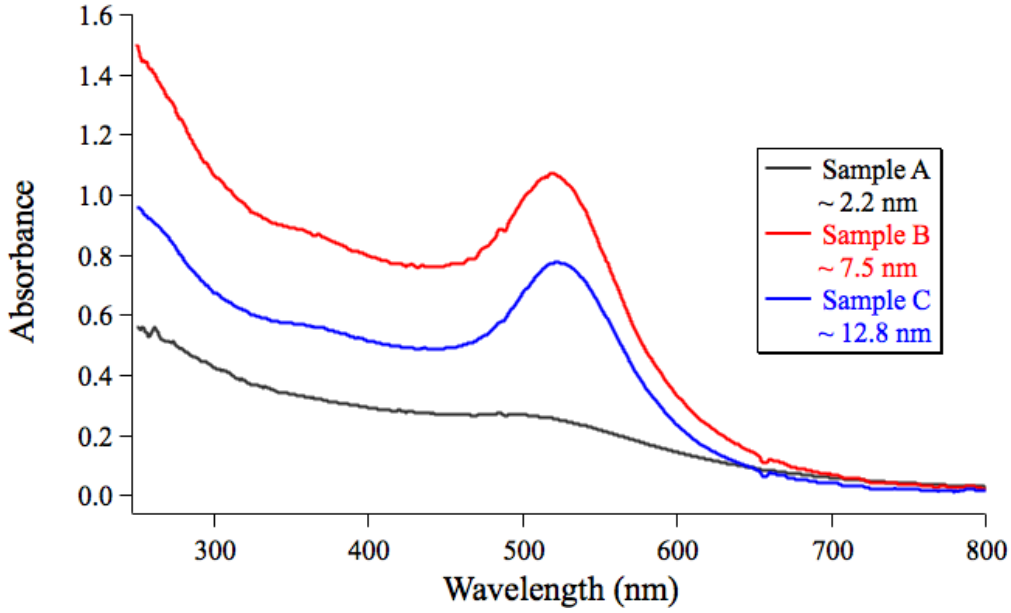

Figure 3. UV/vis data for the three reference samples. Increased intensity of the plasmon resonance relative to the absorbance at 450 nm corresponds to an increase in core diameter. Approximate core diameters were determined by using Equation 1.

Of the techniques discussed in this work, UV/vis analysis is the most rapid, requiring only a couple minutes to perform. UV/vis size analyses of the reference samples shows smaller core sizes than expected. Given that the literature trend was developed for particles 5 – 50 nm in diameter, it is not surprising that some error is

present here. In addition, very small AuNPs like Sample A do not have a sharp plasmon peak, making determination of the λ-max difficult.

The values shown in Table 2 were collected using typical analytical methodology for each technique. SAXS data yield reasonable core sizes for these samples. TEM micrographs showed deposition artifacts in the form of rafting for samples B and C, which is known to artificially increase the observed core diameter.[19] Given an expected ligand shell thickness of ~1.5 nm, the hydrodynamic diameter determined for sample C matches well with the expected value of 17.0 nm (calculated using SAXS measurement of core size). The observed diameter values for samples A and B are lower than the expected values of 5.7 nm and 11.7 nm, respectively. UV/vis core diameter determinations are lower than expected for all three samples. In summary, SAXS analyses showed values with no obvious indication of artifacts, TEM analyses appeared to overestimate AuNP size for samples exhibiting rafting, while DLS and UV/vis analyses underestimated particle size.

Table 2. Summary of size analyses for three reference samples

Sample	SAXS	TEM	DLS	UV/vis
A	3.1 ± 0.6 nm	3.3 ± 0.9 nm	4.4 ± 0.4 nm	~ 2.2 nm
B	9.1 ± 1.9 nm	11.3 ± 2.2 nm	10.2 ± 1.5 nm	~ 7.5 nm
C	14.6 ± 2.2 nm	16.2 ± 1.7 nm	17.0 ± 1.9 nm	~ 12.8 nm

Evaluation of Binary Mixtures

The reference samples were intentionally mixed to evaluate each of the workhorse techniques' ability to differentiate multiple, polydisperse distributions. To generate binary and ternary mixtures with equivalent volumes of gold in each distribution, the scatterer volumes determined by SAXS were utilized to identify the proper amounts of each sample to be mixed. Because SAXS measures particle volume distributions, the scatterer volume is a parameter output by the software, and can be readily used to calculate solution volumes needed for these mixtures. Thus, binary mixtures were generated combining samples [A+B], [A+C], and [B+C] where each mixed distribution contained the same amount of gold. These binary mixtures were analyzed with each of the four workhorse techniques using standard procedures.

SAXS analysis was performed on the binary mixtures following the same experimental procedure as the pure reference samples. By eye, bimodal distributions are apparent in the data, as distinct changes in slope are observed for each binary mixture below $q = 1\ nm^{-1}$. These changes in slope are distinct from the Bessel oscillations,[22] observed at $q > 2\ nm^{-1}$, which reach a local minimum, then rise away from the baseline as q increases. Bessel oscillations are indicative of relative monodispersity in a single distribution.[27] For each binary mixture, the Size Distribution program within the IRENA software[52] identified two distinct distributions. The Modeling II program output AuNP core size, polydispersity, and relative distribution volumes, which are summarized in Table 3. The modeled functions are shown in Figure 4 overlaid onto the raw data. Both the raw data and the modeled data give clear indication that bimodal distributions are present in each of the three binary mixtures.

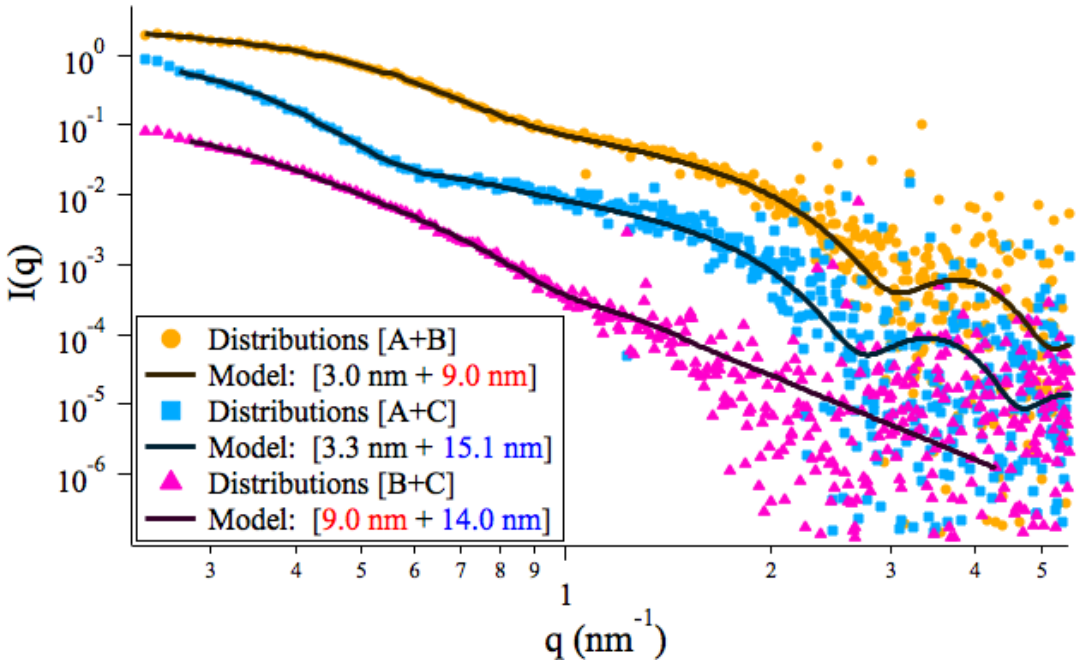

Figure 4. Modeled SAXS patterns for the three binary mixtures used in this study. The sharp changes in slope at ~ 0.9 nm^{-1}, ~ 0.6 nm^{-1}, and ~ 1.0 nm^{-1} for binary mixtures [A+B], [A+C], and [B+C] respectively indicate two unique distributions in the data. Comparing these data to the pure reference samples (Figure 1) reveals that these distinct changes in slope are not present for monomodal distributions. The local minima and maxima observed at q > 2 nm^{-1} for mixtures [A+B] and [A+C] correspond to Bessel oscillations from a single distribution, and are not indicative of additional distributions. Data are offset for clarity.

The SAXS size distributions match well to the that of the individual reference samples. Core size determinations were within 6% of values observed for the pure reference samples. Polydispersities for each mixture were higher than observed values for the corresponding pure samples. These data are summarized in Table 3. In all, the data

analysis procedure was effective at identifying each distribution and average core diameter, though polydispersity values were artificially inflated.

TEM data collection and processing were carried out as with the pure reference samples. In the case of [A+C] and [B+C] two modes were clearly visible, but not in the case of [A+B]. This was a surprising result, but is likely due to a low volume of 3 nm AuNPs. It is also possible that some of these particles were lost during image thresholding. When the original number distribution is converted to a volume distribution, these small, low-contrast particles are more difficult to observe, especially when particle counts are low (< 2000). Collection of more TEM images would improve this analysis, but would require more time. When samples clearly exhibited multiple distributions, IGOR software was used to fit models to the data. Peaks were added manually to model observed distributions. Multipeak least-squares fitting was used to optimize the distribution parameters (Figure 5). These data are summarized in Table 3.

DLS data were obtained for the binary mixtures following the same procedure as the pure samples. The autocorrelation function in the Dynamics software has the ability to pick out multiple distributions through detection of the Brownian motion of the different sizes of particles.[24] However, the user has little ability to impact the software's detection of these multiple distributions, in part because the raw data are difficult to interpret by eye. Thus, multiple distributions are only detected when the autocorrelation function picks out multiple, distinct fluctuations in the scattering signal that correspond to distinct sizes of particles. Overlapping, polydisperse distributions are difficult to observe this way. Of the three binary mixtures, only the [A+C] mixture showed a bimodal distribution in the DLS analysis, and both distributions modeled in this sample deviated

significantly from expected values. For the [A+B] and [B+C] mixtures, only the larger of the two expected distributions was observed. These data are summarized in Table 3.

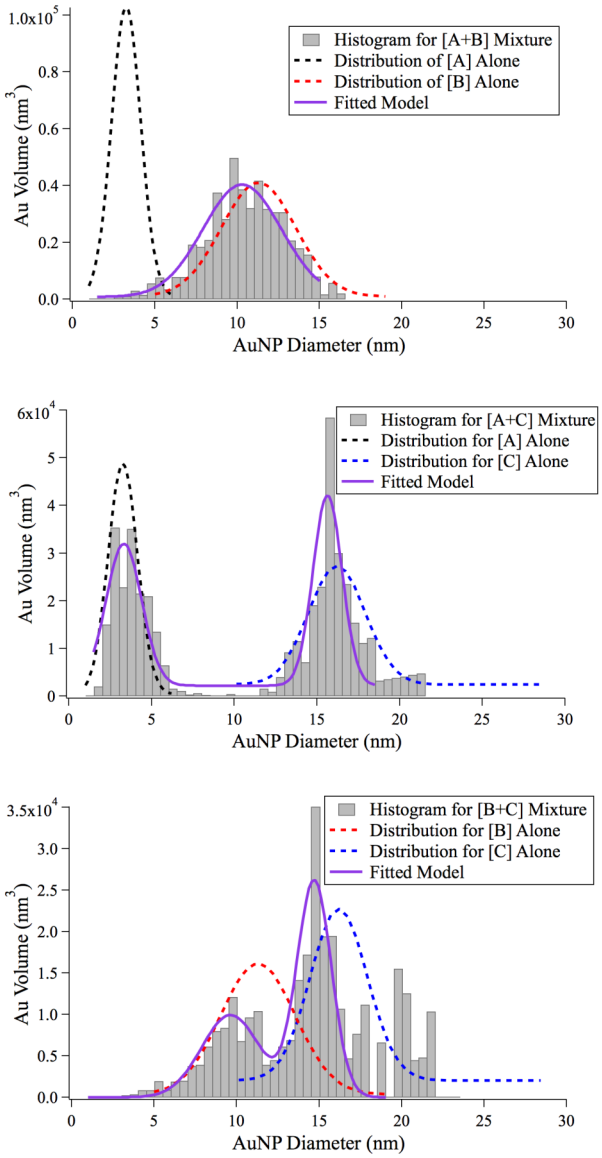

Figure 5. TEM histrograms generated from three different binary mixtures of samples A, B, and C. Binary mixtures [A+B], [A+C], and [B+C] are shown. TEM data are shown in gray histogram bars. Solid purple traces represent the optimized peak fits to the data, where bins with less than 5 particle counts were ignored. Expected distributions were taken from TEM analysis of the pure samples, and shown as dashed traces.

UV/vis data were collected for the binary mixtures in the same fashion as the pure reference samples. Each of the binary mixtures showed only a single plasmon peak in the UV/vis spectrum (Figure 6). Thus, there was no indication of multiple distributions. The size analysis was performed as if only a single distribution were present in the data. These size estimations are summarized in Table 3.

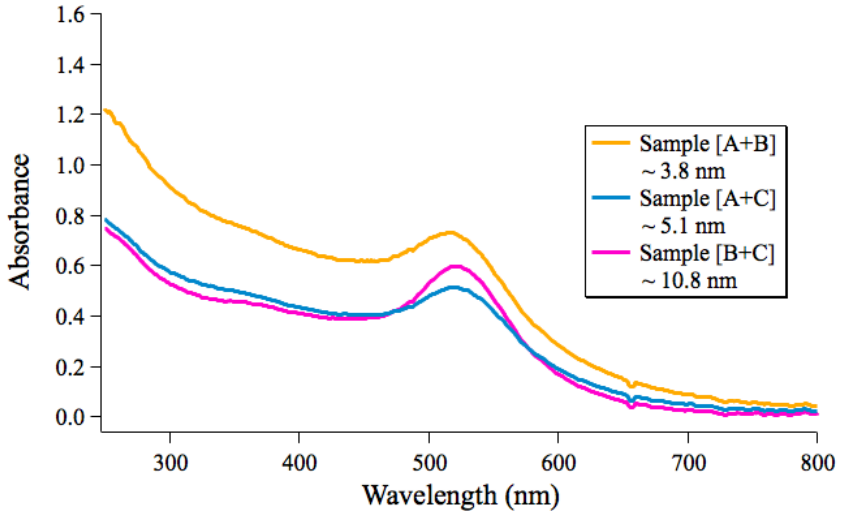

Figure 6. UV/vis spectra for each of the three binary mixtures. Because only one plasmon peak is observed for each sample, the multiple distributions are not detected. Size approximations were determined using Equation 1, and result in a value between the average diameters of the two pure samples for each mixture.

Table 3. Summary of size analysis for three binary mixtures†

Sample	SAXS	TEM	DLS	UV/vis
[A + B]	3.0 ± 1.7 nm **45%** 9.0 ± 2.2 nm **55%**	-- -- 10.3 ± 2.4 nm --	-- -- 8.6 ± 0.6 nm --	~ 3.8 nm
[A + C]	3.3 ± 2.0 nm **41%** 15.1 ± 2.9 nm **59%**	3.3 ± 1.0 nm **48%** 15.6 ± 0.8 nm **52%**	1.2 ± 0.2 nm **99%** 18.2 ± 3.6 nm **1.0%**	~ 5.1 nm
[B + C]	9.0 ± 1.5 nm **34%** 14.0 ± 3.7 nm **76%**	9.6 ± 1.8 nm **39%*** 14.7 ± 1.0 nm **61%***	-- -- 19.4 ± 8.5 nm **99%***	~ 10. 8 nm

† - Measured mass contributions for each distribution are shown in **bold**. The expected value is 50% for each distribution.
* - Additional large aggregates observed.

Compiled size determination data for the three binary mixtures generated from the three AuNP reference samples used in this study are shown in Table 3. SAXS data show clear indications of bimodal distributions for each mixture with no additional distributions indicated. Observed volumes deviate significantly from expected values when the distributions overlap. All core diameters are within 6% of expected values. Polydispersity values are off significantly in some cases. TEM and DLS data exhibit some ability to differentiate bimodal distributions, missing distributions for the [A+B] mixture and showing additional distributions for the [B+C] mixture. Both techniques are able to detect a bimodal distribution in the [A+C] mixture, as this mixture has the largest difference in average core size between the two distributions. UV/vis shows no ability to

resolve bimodal distributions, and yields an average value between the two mixed samples. In summary, SAXS was the only technique to identify each mode in the three binary mixtures using standard methodology, while TEM was able to identify both modes in two out of three mixtures, DLS identified both modes in only one out of three mixtures, and UV/vis could not identify multiple modes in any of the samples.

Evaluation of Ternary Mixture

Since the workhorse techniques showed some success at identifying the multiple modes in binary mixtures, we sought to determine if any of the investigated techniques could identify an even more complex mixture using all three reference materials. As with the binary mixtures, SAXS scatterer volumes were used to determine appropriate mixed amounts of each pure sample to obtain equal-volume distributions in the ternary mixture. This mixture was analyzed by each of the four workhorse methods to determine which of these techniques can differentiate the three particle size distributions present in solution. All data collection and analysis procedures remained the same as with previous pure samples and binary mixtures, simulating the expected analysis for an unknown sample. SAXS analysis of the ternary mixture is shown in Figure 7, while TEM and UV/vis analyses are shown in Figures 8, 9 respectively. DLS data are summarized in Table 3.

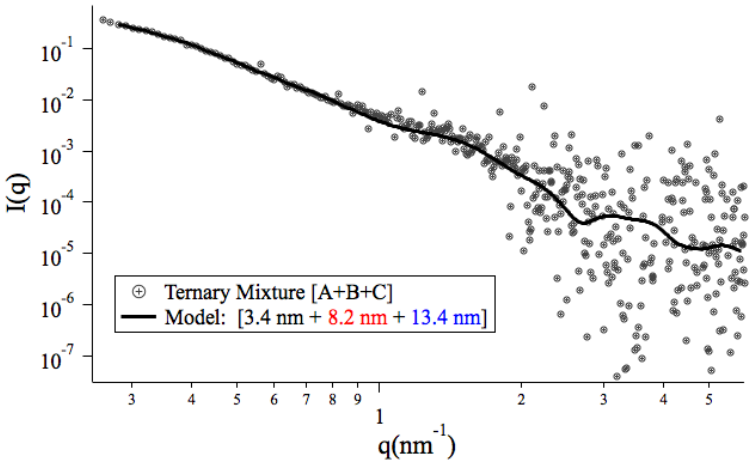

Figure 7. Raw SAXS data with fitted model from analysis of ternary mixture [A+B+C]. Each of the three mixed samples is clearly identified with average core diameters within 10% of expected values.

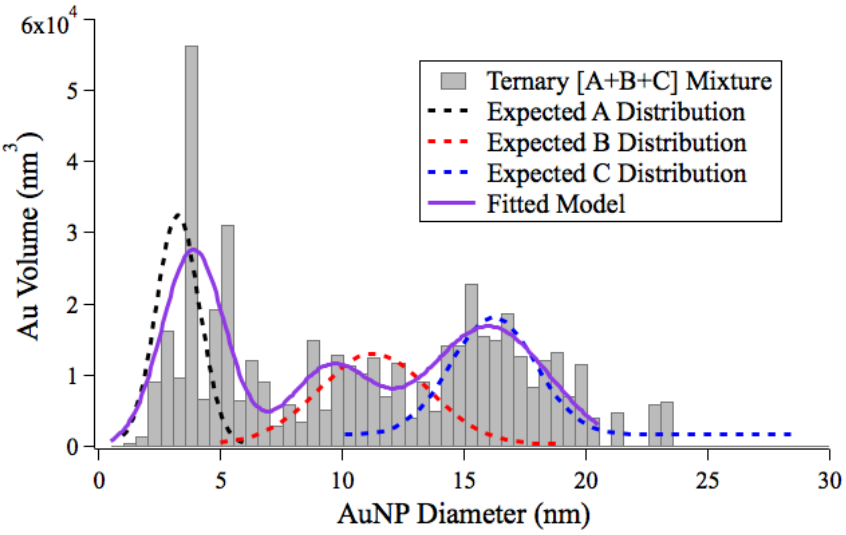

Figure 8. TEM histograms generated from the ternary mixture of samples A, B, and C. TEM data are shown in gray histogram bars. The solid purple trace represents the least-squares optimized peak fits to the data, where bins with less than 5 particle counts were ignored. Expected distributions were taken from TEM analysis of the pure samples, and shown as dashed traces. All three of the added mixtures are apparent in the histogram, though over 10,000 particle counts were required to resolve these modes.

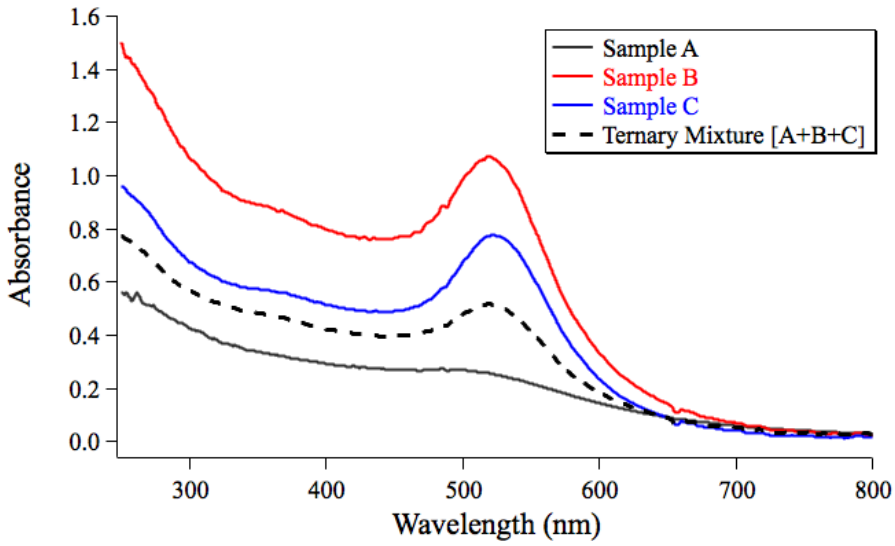

Figure 9. UV/vis spectrum of ternary mixture of pure samples A, B, and C. Traces of pure samples are shown for comparison. UV/vis shows no ability to differentiate the components of this mixture.

Table 3. Summary of size analysis for ternary mixture†

Sample	SAXS	TEM	DLS	UV/vis
[A+B+C]	3.4 ± 1.0 nm **24%**	3.9 ± 1.2 nm **38%**	2.0 ± 0.1 nm **97%**	~ 7.5 nm
	8.2 ± 3.0 nm **18%**	9.6 ± 1.5 nm **18%**	-- --	
	13.4 ± 3.7 nm **58%**	15.9 ± 2.4 nm **44%**	17.0 ± 1.0 nm **3%**	

† - Values in bold are measured distribution volumes. Expected values are 33% for each.

Compiled size determination data for the ternary mixture, [A+B+C], show that SAXS and TEM are able to resolve all three distributions. The particle core size values for each distribution have varying amounts of error. SAXS average diameters are within 10% of expected values, while volumes deviate from expected values by up to 25% and polydispersity values deviate by up to 60%. TEM average diameters are within 15% of

expected values, volumes deviate by up to 15%, and polydispersity values deviate by up to 50%. In summary, both SAXS and TEM can identify the individual modes of a ternary distribution, but SAXS provides the ability to perform this analysis more rapidly and identify the modes in an automated fashion. Modeled modes in the TEM data were picked manually, potentially introducing researcher bias. DLS and UV/vis measurements cannot resolve the trimodal distribution.

Comparison of Techniques

Comparing the four workhorse techniques, there are five general attributes by which to rate them: (1) ability to identify multimodal distributions without introducing researcher bias, (2) speed of analysis, (3) error associated with determination of average diameter, (4) error associated with determination of polydispersity for mixtures, and (5) error associated with determination of volumes for mixtures. This section will assess the selected techniques based on these attributes. These techniques will be summarized with respect to the error associated with each of the relevant parameters.

Of the four workhorse techniques, SAXS was the only technique to identify each individual distribution in an automated fashion. The two-step data processing procedure first identifies distributions, then allows the researcher a great deal of control over modeling the observed distributions. For each sample observed, SAXS analysis identified the correct number of distributions. Additional distributions were not observed, nor were any distributions missed during analysis. In addition, SAXS data collection was easily automated and data processing was rapid.

Observed average diameters for mixed samples were within 10% of expected values (from analysis of pure reference samples). Polydispersity values were more difficult to resolve, and varied by up to 60% from expected values. Distribution volumes varied up to 25% from expected values, where smaller particle distributions were underrepresented, especially when overlapping significantly with a larger distribution.

TEM analysis also shows the ability to resolve multimodal distributions, though it has limitations. However, even in the pure reference samples, deposition artifacts were observed and average diameters were larger than expected. This was more prominent for the larger AuNPs. For the mixed samples, TEM analysis was able to pick out the multiple distributions, but only when particle counts were >10,000 (mixtures [A+C] and [A+B+C]). When particle counts were lower than this (1700 counts for mixture [A+B] and 550 counts for [B+C]), the multiple distributions were not well resolved or were unobservable. It should be noted that the ability to resolve these distributions is only limited by the time input of the researcher. Given more images and particle counts, the data suggest that all of the mixtures could eventually be resolved, though the necessary time input could be prohibitive.

Gathering enough images to reach high particle counts (> 10,000) is time consuming and it is not practical to automate this data collection process. For some samples with less dense particle packing on the TEM substrate, dozens of images may be required to reach 10,000 particle counts. This high number of images is not typical, where 6 – 10 images are generally collected to achieve several hundred particle counts.[19,50] While automated image analysis is performed by some groups, each of the

TEM images were manually processed for this work, contributing to the considerable time input required to adequately analyze each sample.[13]

When particle counts were sufficiently high, TEM size analysis of mixed samples performed similarly to SAXS analysis. Average diameters were within 15% of expected values. Polydispersity values were within 50% of expected values. Distribution volume values were slightly closer to expected values than SAXS, remaining within 15% error. Overall, it appears that TEM and SAXS show similar ability to differentiate multiple distributions, though TEM requires considerably larger time input to obtain sufficient data and analysis can suffer from deposition artifacts.

DLS size analysis is more rapid than either SAXS or TEM measurements. Once the sample is loaded, the data are collected within minutes and the data processing is mostly automated.[24] This is convenient for simple samples, but the researcher has little control over modeling of the output signal. There is more advanced software that exists, but the standard, manufacturer-provided software was used for this study. Thus, while analysis is rapid, it is also limited to what distributions the software can identify. In the cases of the mixed samples used in this study, DLS showed poor ability to differentiate these multimodal distributions. It appears that mixed samples with the degree of polydispersity used in this study are not differentiable by DLS. Even in the cases where multiple distributions were identified, diameters, polydispersities, and volumes deviated significantly from expected values.

DLS analysis of the pure reference samples and comparison to SAXS core diameter values suggests that DLS can accurately determine the hydrodynamic diameter for the largest particles used in this study, Sample C. The measured hydrodynamic

diameter of 17.0 nm was within 4% of the expected value, given a core diameter of 14.6 nm (from SAXS analysis) and expected ligand shell thickness of 1.5 nm. However, DLS analysis of the smaller Samples A and B yielded hydrodynamic diameters that were lower than expected. Analysis of Sample B showed a diameter 21% lower than expected while Sample A showed a diameter 43% less than expected. It appears that these particles are too small for DLS to accurately determine their diameters.

UV/vis size analysis of the AuNPs used in this study showed no ability to resolve multiple distributions. The optical properties of the polydisperse AuNPs in Samples A, B, and C were too similar to differentiate with this method. While this technique is the most rapid of those investigated, it also proved to be the least informative. Size analysis for Samples A, B, and C yielded average diameters that were 29%, 18%, and 12% less than expected for these samples. This suggests that size analyses used here are not appropriate for AuNPs in this size range.

Table 4. Summary of size analysis for four workhorse techniques

Attribute	SAXS	TEM	DLS	UV/vis
Identifies Multiple Distributions	Yes	Yes, with enough NP counts	Limited ability	No
Researcher Time Input for One Sample	~ 30 min	~ 2.5 hours	~ 15 min	~ 5 min
Error for Mixed Sample Diameter Determination	10%	15%	--	--
Error for Mixed Sample Polydispersity Determination	60%	50%	--	--
Error for Mixed Sample Volume Determination	25%	15%	--	--

Conclusion

This work compared four prominent analytical methods with respect to their ability to analyze three pure reference samples, and mixtures of these samples. Each of the investigated techniques were able to adequately analyze the pure reference materials, where SAXS analysis showed the most reliable core size values, TEM analysis overestimated core size for some samples, and both DLS and UV/vis analyses underestimated core size. For binary mixtures, SAXS analysis identified each mode within 10% error. TEM and DLS identified both modes for some of the mixed samples, but not all. UV/vis showed no ability to identify multiple modes. For the ternary mixture, SAXS and TEM identified all three modes, though SAXS required much less time input and introduces less researcher bias.

It should be noted here that the observed performance of each technique is indicative of a single, standard analysis of each sample. This methodology is intended to represent a typical day-to-day analysis of a nanoparticle sample, and not necessarily an exhaustive analysis. Thus, the limitations of the analyses described here are not descriptive of the true limits for each analytical technique as a whole.

Of the tested techniques, SAXS provided the most consistent ability to detect multiple distributions. TEM shows similar ability to resolve different modes, but requires more time input to perform this analysis. However, it should be noted that SAXS is not a direct imaging method, and cannot access morphology information. For an unknown sample, SAXS is best performed in tandem with TEM, where morphology can be confirmed. A large number of particle counts is not needed to confirm the morphology of the particles, which reduces the time needed to collect the data. Further, DLS analysis is

the only method investigated here which can detect hydrodynamic diameter, and is a rapid technique. Similarly, UV/vis can be performed rapidly to gain qualitative information about the sample. It should be noted, that each of these techniques present distinct advantages, and each should be used in tandem to gain a broader understanding of a particular sample.

For the analysis of nanomaterials in general, each of the workhorse techniques described here provide valuable information (with the possible exception of UV/vis if there are no optical signatures). For the most complete characterization of a material, we recommend first using UV/vis to gain rapid qualitative information about the stability and size of the particles. Then, quick spot checks should be performed in TEM to confirm particle morphology, followed by DLS if ligand shell thickness is desired. Lastly, detailed SAXS analysis should be performed to obtain reliable, quantitative measures of particle size distributions. This flow of information will provide the most complete understanding of a new material while minimizing time input.

Bridge to Chapter VI

Chapter V showed that SAXS and TEM size analyses have the potential to differentiate binary and ternary mixtures, though SAXS requires less time, is more reliable, and introduces less researcher bias. Thus, we determined through this comparative study that SAXS is the best candidate to study AuNP formation processes. Chapter VI focuses on the use *in situ* SAXS incorporated into a microreactor to probe the size distributions of AuNPs at early reaction times to determine which mechanistic processes are relevant for AuNP growth when Bunte salt ligands are used.

CHAPTER VI

OBSERVING GOLD NANOPARTICLE GROWTH USING SIMULTANEOUS *IN SITU* SAXS AND UV/VISIBLE SPECTROSCOPY

Introduction

Gold nanoparticles (AuNPs) have been shown to be useful for a wide variety of applications because of their interesting size-dependent properties.[1-5] While these materials have been studied thoroughly for their interesting physical properties, much less is known about the mechanistic processes that form AuNPs.[6] Many studies of AuNP systems assume the Classic Nucleation Theory (CNT), as the operative mechanism for particle formation and growth.[7-9] This theory was developed in the 1920's and 1930's by several researchers to describe vapor to liquid phase transitions.[10,11] LaMer and Dinegar utilized CNT in 1950 to describe the formation of sulfur sols from molecular precursors in solution,[12] though it wasn't applied to NP systems until Sugimoto's work in 1986.[13] This theory has been generally useful to describe nanoparticle reactions, especially for semiconductor nanocrystals, but more recent work has demonstrated that CNT does not explain observed experimental results for specific AuNP systems.[6]

Study of AuNP formation mechanisms using traditional strategies has been challenging for several reasons. First, AuNP formation reactions are typically very rapid, occurring on the order of milliseconds, making these reactions difficult to monitor.[14-17] While the use of pseudo-first-order conditions has been used to simplify the kinetics and facilitate data collection for NP catalytic activity[18] or ligand exchange,[19] this strategy has not been useful for studying this very rapid particle formation because the necessary

changes in synthetic conditions yield unique size distributions. Further, polydispersity in samples complicates analysis and introduces an additional parameter that must be measured.[20] These product distributions can also change significantly with small changes to reaction conditions.[20] These challenges have necessitated new strategies to access mechanistic information on AuNP systems.[6]

Researchers are currently focusing on *in situ* methods to gain further insight into AuNP reactions, using citrate,[21] amines,[17] or weak ionic species to passivate the particles.[22] Microfluidics have proven essential in these studies, providing rapid mixing and steady-state observation conditions at each point along the reactor, facilitating *in situ* observation at early reaction times (as early as 100μs).[14,23-25] An observation cell incorporated into the system allows a specific residence time (corresponding to a specific reaction time) to be studied for extended durations as material flows through the cell. *In situ* studies with small-angle X-ray scattering (SAXS) have shown how particle size and polydispersity evolve over time.[7,21,22,26-29] *In situ* UV/visible spectroscopy (UV/vis) provides information about AuNP optical properties and concentration, along with a qualitative indication of particle size.[7,17,23,30] Other *in situ* studies (such as XANES and XAFS) have provided time-resolved information about molecular oxidation states (i.e.; precursor species), though these data provide limited insight about the nanoparticles themselves.[21,28,31-33] In combination, these *in situ* strategies have begun to illuminate reaction processes in AuNP systems.

A notable example by Polte et al.[22] studied AuNP formation using a combination of continuous flow and *in situ* SAXS to probe a synthesis with $HAuCl_4$ as a NP precursor and $NaBH_4$ as reducing agent. The authors observed a rapid reduction of Au(III) to

Au(0), forming small nuclei.[22] This was followed by growth exclusively through coalescence. Given that no passivating agent was used in this system, these observations are unsurprising, but another study using citrate as a passivating agent and reductant demonstrated AuNP growth via coalescence as well.[21] However, no study has yet investigated whether AuNP systems using strongly-binding ligands that form covalent linkages to the AuNP surface proceed through a coalescence mechanism.

Recent work in our lab has shown that AuNP synthesis using Bunte Salts ligands provides a convenient route to thiolate-passivated AuNPs.[34] Bunte salts form covalent thiolate linkages to a Au surface while initially having ionic character that can act as a stabilizing surfactant prior to conversion to thiolate.[35] This system is interesting because of the ability to tune the particle size and the wide range of ligands that can be easily synthesized with Bunte Salt functionality.[34,36,37] The utility of this synthetic system warrants further efforts to elucidate reaction processes.

The aim of this work was to determine whether coalescence is observed during AuNP growth when using Bunte salt ligands. Utilizing the steady-state observation conditions in a microreactor, simultaneous SAXS and UV/vis were used to probe AuNP growth as a function of reaction time. SAXS provided quantitative measurement of AuNP size and polydispersity,[38] while UV/vis provided real-time qualitative assessment of particle size and stability.[23] The combination of both techniques provided quantitative determination of AuNP concentration.[30] Assessment of time-resolved AuNP size, polydispersity, and concentration data showed that coalescence is an active process in AuNP growth when using Bunte salts, consistent with previous *in situ* studies.

Experimental

Materials

Hydrogen tetrachloroaurate hydrate ($HAuCl_4 \bullet xH_2O$, 99.9%) was purchased from Strem and used as received. Sodium hydroxide was purchased from Macron and used as received. Sodium borohydride was purchased from Sigma Aldrich and used as received. Water used for aqueous syntheses was purified with a Barnstead NANOpure filtration system (18.2 MΩ resistivity). MEEE Bunte Salt ligand was prepared using known procedures.[34] Briefly, 1 molar equivalent of 2-[2-(2-chloroethoxy)-ethoxy]ethanol was dissolved in nanopure water. 0.8 molar equivalents of sodium thiosulfate were added and the solution was refluxed for 3 hours. Water was removed en vacuo, and the crude products were purified by dissolution in cold ethanol followed by gravity filtration.

Microfluidic AuNP Synthesis

Aqueous solutions were prepared for three successive microfluidic syntheses at each reaction condition. Thus, 30 mL of 5.0 mM $HAuCl_4$, 30 mL of 1.0 mM Bunte Salt ligand, and 60 mL of 1.0 mM $NaBH_4$ were prepared. A total of 0.825 mL of 1 M NaOH was added to the $NaBH_4$ solutions. Once the appropriate amount of base was added to the respective solutions, each of the three solutions was aspirated by the three syringe pumps as shown in Figure 1.

60 mL/min Conditions. The 20 mL of $NaBH_4$ solution was dispensed at 30 mL/min, mixed with a stream of 10 mL of ligand solution flowing at 15 mL/min, allowed to mix for 1 second in the reactor before introducing the third stream of 10 mL of $HAuCl_4$ solution flowing at 15 mL/min. Two simple T-mixers were used to mix the reagents.

20 mL/min Conditions. The 20 mL of $NaBH_4$ solution was dispensed at 10 mL/min, mixed with a stream of 10 mL of ligand solution flowing at 5 mL/min, allowed to mix for 1 second in the reactor before introducing the third stream of 10 mL of $HAuCl_4$ solution flowing at 15 mL/min. Two simple T-mixers were used to mix the reagents.

3 mL/min Conditions. The 20 mL of $NaBH_4$ solution was dispensed at 1.5 mL/min, mixed with a stream of 10 mL of ligand solution flowing at 5 mL/min, allowed to mix for 1 second in the reactor before introducing the third stream of 10 mL of $HAuCl_4$ solution flowing at 0.75 mL/min. Two simple T-mixers were used to mix the reagents.

Microreactor System

Three syringe pumps each equipped with 3-way distribution valves were purchased from Kloehn (Versa 6, 48k model with rotary valve). All other microreactor components were purchased from IDEX Health and Science. FEP tubing (1/16" outer diameter, 0.030" inner diameter), T-mixers (1/16", 1/4-28, 0.020" Thru, ETFE), 15 psig check valves, and appropriate fittings (1/4-28) and ferrules were assembled with the syringe pumps as shown to enable microfluidic generation of AuNPs. The microreactor system was rinsed with nanopure water three times (full aspirate/dispense cycles of the syringe pumps) after each synthesis. After each set of three syntheses, the downstream T-mixer that introduces the $HAuCl_4$ solution and tubing thereafter was replaced with a clean mixer and tubing. The used mixers are later cleaned with aqua regia and water to remove any plated Au material left behind. All used tubing was discarded.

In Situ Measurements

SAXS measurements were performed at BL 7.3.3 at the Advanced Light Source (ALS, LBNL, Berkeley, CA). BL 7.3.3 is a SAXS/WAXS facility and also is mounted on a regular ALS bending magnet. A Mo/BC double multilayer monochromator provides monochromatic X-rays at 10 keV, and the spot size at the sample is 1 mm horizontal x 0.24 mm vertical. The volume of solution observed by SAXS, defined by the pathlength and the dimensions of the X-ray beam, is 0.72 μL. At a flow rate of 3 mL/min, this volume is refreshed every 14 milliseconds. At a flow rate of 60 mL/min, this volume is refreshed every 0.72 milliseconds.

The scattering intensity, I(q), as a function of the modulus of the scattering vector $q=(4\pi/\lambda) \sin(\theta/2)$, where θ is the scattering angle and λ is the wavelength of the X-rays was recorded using ADSC Quantum 4u CCD detectors. With SAXS and WAXS measurements, the total q range of the system is between 0.004 and 8.7 A^{-1}. The accumulation time for SAXS measurements of each sample was between two and five minutes. At least seven measurements were taken for each sample and averaged to determine scattering intensity. The observed scattering intensities were corrected by subtraction of scattering of the solvent-filled cell and with corrections for the fluctuation of the beam intensity. *In situ* UV-visible absorbance spectra were collected from flowing nanoparticle solutions in H_2O using ferrule-terminated fiber optics (Ocean Optics - FIA-P400-UV), an Ocean Optics DT-MINI-2-GS Deuterium-Tungsten-Halogen light source, and an Ocean Optics USB2000 spectrometer.

SAXS Data Analysis

SAXS data were processed using IGOR Pro v6.02A software. SAXS data averaging, background subtraction, and conversion from 2D CCD images to 1D plots were performed using the Nika v1.17 macro. Application of models to the SAXS plots was performed using the Irena v2.27 macro.[39] Solvent plots were normalized at large q values to compensate for the variation in X-ray intensity between runs. Normalized solvent plots were then subtracted from corresponding Au nanoparticle plots, and the resultant data were fitted to an appropriate model as discussed below.

Each set of Au nanoparticle data was fitted to a monomodal distribution of scatterers, and each component of the distribution was modeled using a spheroidal form factor, F, defined by the equation:

$$F^2 = \frac{3}{qR^3} * (\sin(qR)) - (qR * \cos(qR)) \qquad (1)$$

where q refers to the scattering vector in nm^{-1} and R is the average spheroid radius. Data were fitted to both Gaussian and lognormal distributions of nanoparticle sizes. Best-fit models were developed by minimizing χ^2 values. In all cases, models using a lognormal distribution output a smaller χ^2 value than for the corresponding Gaussian distribution. Thus, all reported values for nanoparticle size and polydispersity have been derived from models using a lognormal distribution. Final SAXS patterns were depicted as $I_{fit}(q)$ vs. q, where q is expressed in nm^{-1} and $I_{fit}(q)$ is defined by the equation:

$$I_{fit}(q) = |\Delta\rho|^2 \sum_{r_{min}}^{r_{max}} |F(q,r)|^2 V^2(r) * N * P(r) * \Delta\rho \qquad (2)$$

where $\Delta\rho$ refers to contrast, F(q,r) is the structure form factor, V(r) is the particle volume, N is the total number of scattering particles, and P(r) is the probability that a particle possesses a radius equal to r according to the lognormal distribution.

Results and Discussion

A microreactor system, shown in Figure 1, was used to collect simultaneous SAXS and UV/vis data *in situ*. The steady-state observation conditions provided by a microfluidic system are ideal for these studies because residence times correspond to reaction times. This approach to *in situ* observation is advantageous because sample damage from X-ray exposure is minimized, as individual particles spend very short durations in the beam path.[23] Moving the observation cell closer to or further from the final mixer accesses unique residence times, facilitating observation of the reaction progression.

Two different flow rates were utilized to observe a wider range of residence times. At a total flow rate of 60 mL/min, residence times from 0.15 – 3.0 sec were observed. To observe longer residence times, up to 60 sec, a 3 mL/min flow rate was used. While varied flow rates result in different final size distributions,[40] it is necessary to use slower flow rates to observe the longer reaction times needed for this study. The difference in size is attributed to differences in mixing rates. At higher flow rates a larger number of AuNPs with smaller diameters are formed,[40] and, conversely, slower flow rates result in a small number of AuNPs with larger diameters. While the data taken at different flow rates cannot be directly compared, relevant mechanistic pathways should be similar because the reaction conditions are still very similar.

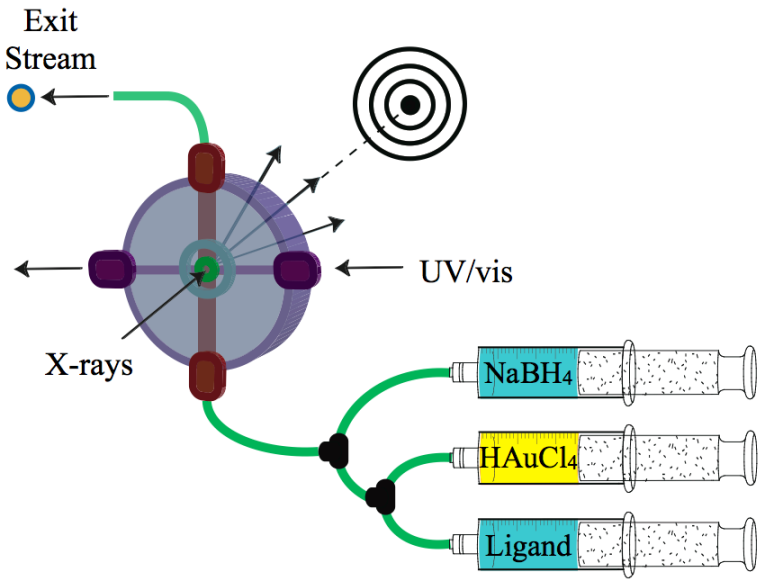

Figure 1. Microreactor setup for *in situ* studies. Steady-state conditions at each point along the microreactor after mixing allows residence time to be correlated to reaction time. Inclusion of an observation cell allows a specific residence time (and thus reaction time) to be observed for extended durations as material flows through the system. The length of tubing between the final mixer and the observation cell is varied to select the residence time observed. There are practical maximum and minimum tubing lengths available in this setup, meaning that for specific flow rates, defined residence times are observable. Thus, fast flow rates are used to access early residence times while slow flow rates are used to access later residence times. A 60 mL/min flow rate was used to observe 0.15 – 3 sec and 3 mL/min was used to observe 1 – 60 sec residence times.

Studies at the highest observed flow rate (60 mL/min) show that the AuNPs are 1.8 nm in diameter by 150 ms residence time (Figure 2). This corresponds to ~ 200 Au atoms in the particle cores at this very early reaction time. This matches well to

observations made by Polte et al. that AuNPs were ~ 1.6 nm in diameter by 100 ms.[22] Indeed, it appears that AuNPs are formed immediately upon exposure to $NaBH_4$, and that no buildup of reactive species is necessary for AuNP formation and growth. This is in contrast to systems with weaker reducing agents, such as citrate, where particle growth continues for several hours.[21]

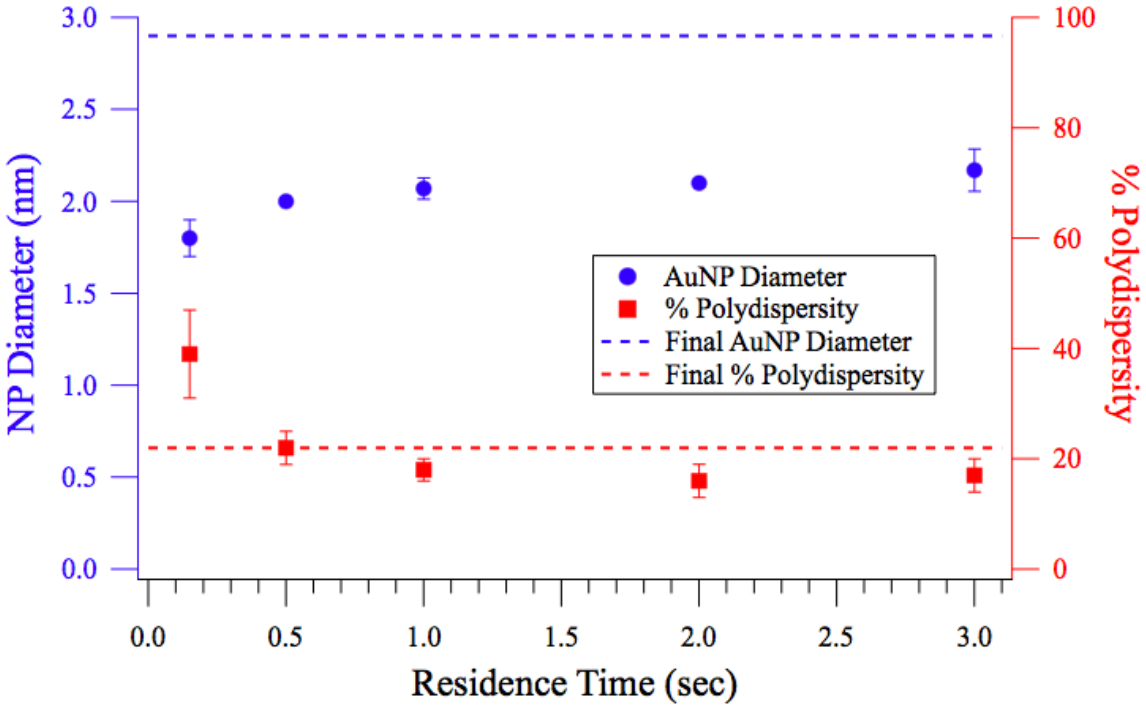

Figure 2. Compiled SAXS data for AuNPs observed at 60 mL/min. Data points shown are from three individual synthetic runs and corresponding *in situ* data collection to determine run-to-run error. The dashed lines depict final values for AuNP diameter and polydispersity from collected AuNP samples. These data demonstrate very rapid AuNP formation, with ~ 200 Au atoms in the particle cores by 150 ms residence time. The particles then continue to grow, with polydispersity decreasing during growth.

To determine how long the AuNPs continue to grow, slower flow rates were necessary. Reactions were run at 3 mL/min to access longer residence times up to 60 sec. Observation at longer residence times shows that the AuNPs continue to grow in diameter until ~ 20 sec (Figure 3). In addition, relative polydispersity drops until this point. After 20 sec residence time, there appear to be no further changes in the size distribution. It is interesting that the AuNP reaction reaches completion so rapidly. This means that the particles can be synthesized very quickly, and implies that performing the reactions in flow can reduce long reaction times used in other systems.[36,41-44]

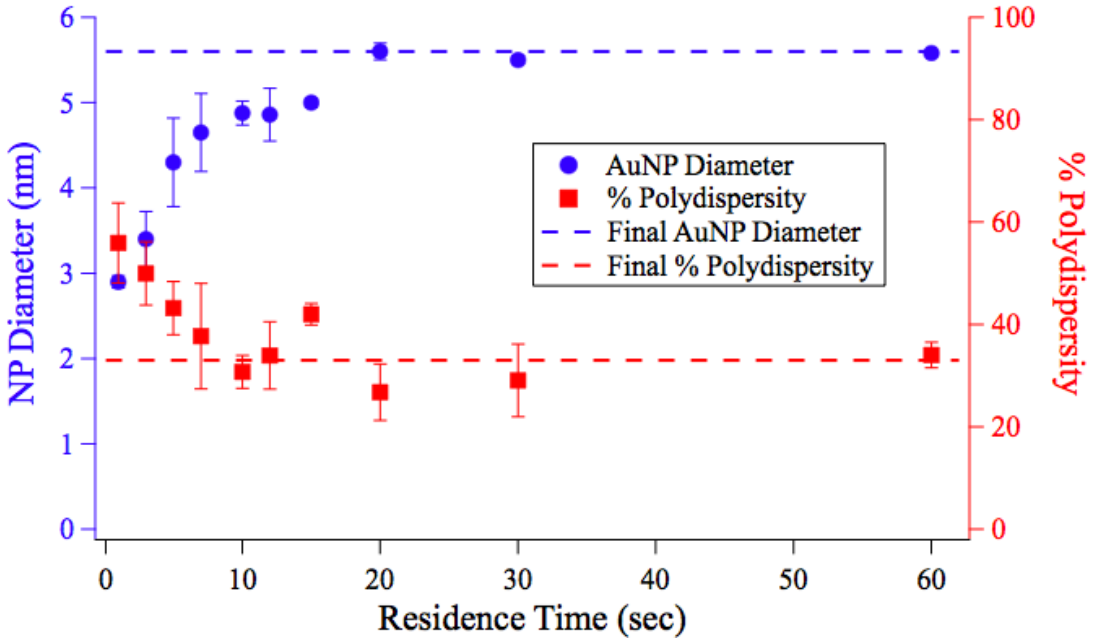

Figure 3. Compiled SAXS data for AuNPs observed at 3 mL/min flow rates. Data were collected from 1 – 60 sec residence times. AuNPs reach final size distribution dimensions by ~ 20 sec. While the final size distribution is distinct from that produced at a 60 mL/min flow rate, all reagent concentrations are identical and it is expected that reaction processes proceed similarly, aside from the number of nuclei initially produced.

To determine quantitative AuNP concentrations, SAXS and UV/vis data were used in concert (Equation 1).[30] SAXS data provide determination of the average particle core diameter, which correlates to a specific extinction coefficient of the plasmon resonance. UV/vis data provide the absorbance at the plasmon resonance. The UV/vis path length was fixed and SAXS and UV/vis data were collected simultaneously, allowing the concentration of particles to be determined quantitatively at each residence time.

$$A_{SPR} = \varepsilon_{SPR} * b * c_{AuNPs} \qquad (1)$$

Examining the time-resolved AuNP concentration data reveals strikingly that the concentration of nanoparticles in solution drops during particle growth (Figure 4). For all flow rates investigated, a decrease in AuNP concentration is observed as the reaction progresses. These observations suggest that a ripening[45-47] or coalescence[48-50] mechanism is active, rather than the CNT prediction of simple particle growth. Because of literature precedent showing coalescence,[6,21,22] and previous work in our lab[51] that shows how multiple distributions can be observed by SAXS (as in Ostwald ripening), coalescence is the most likely mechanism for AuNP growth using Bunte salt ligands.

The observed coalescence is similar to that observed in previous literature utilizing weakly-passivating ligands.[6,21,22] In cases using more strongly-passivating ligands, coalescence is not observed.[17,26,31] Notably, coalescence ceases after ~ 20 sec when using Bunte salts, while cases using purely ionic passivation exhibit coalescence for long durations (~ 24 hours).[22] This suggests that Bunte salts act as weak passivants during particle growth, then strong passivants after ~ 20 sec of reaction time.

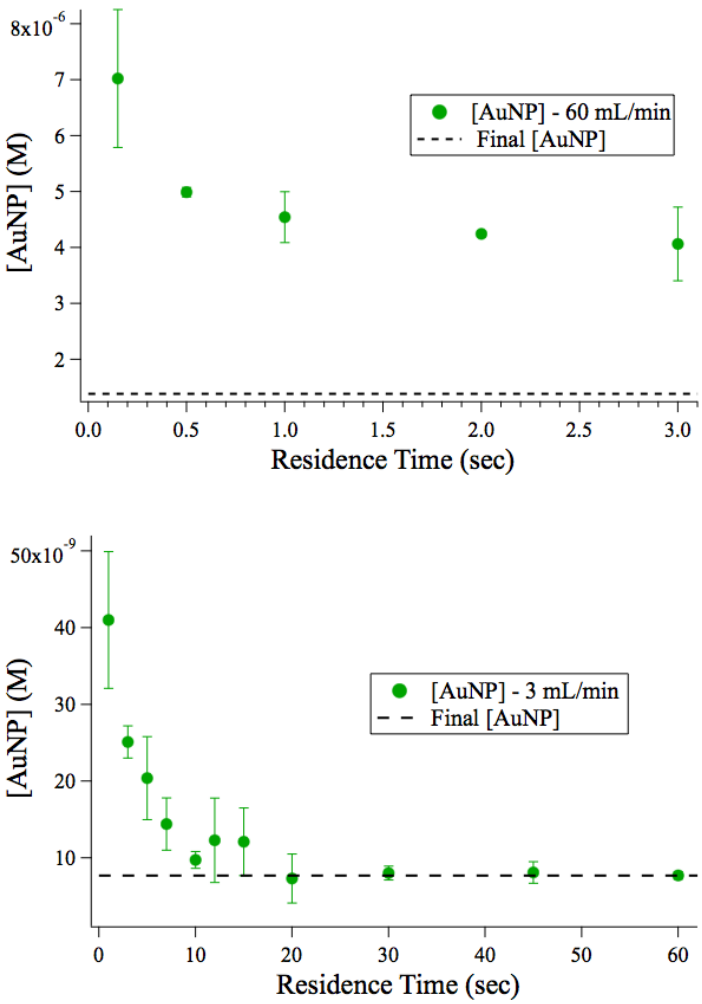

Figure 4. Combined SAXS and UV/vis data collected *in situ* simultaneously enable determination of quantitative AuNP concentrations. As residence time (and thus reaction time) increase, AuNP concentration decreases. This is observed for all flow rates investigated. The cessation of the AuNP concentration drop coincides with cessation of particle growth. These data show clearly that the particles are growing through a mechanism other than that predicted by CNT. Though ripening could be occurring, SAXS data show monomodal distributions at all time points, meaning a coalescence mechanism is more likely.

These observations of particle coalescence have interesting implications for Bunte salt ligands. It is known that Bunte salts first associate with a Au surface in ionic form.[35] After associating with the Au surface, the sulfite group dissociates and eventually diffuses away from the surface, leaving a thiolate linkage to the Au surface.[35,52] Presumably, there is a phase during AuNP growth in this system where the particles are weakly passivated with ionic Bunte Salt ligands before thiolate linkages have formed (Figure 5). It is likely that during this stage the ionic passivation of the AuNPs is weak enough to facilitate coalescence, resulting in fusion of growing AuNP cores and a lower total concentration of particles over time. As the reaction progresses, more thiolate linkages are expected to form, fully stabilizing the particles and preventing further coalescence. This hypothesized model of reactivity is consistent with previous *in situ* studies,[6,21,22] and fits well with the available data.

In summary, it has been observed in cases with weak, ionic passivation that particles grow through coalescence over long durations.[6,21,22] In cases with strong, covalent passivation, no coalescence is observed.[17,26,31] Shown here, the AuNP synthesis using Bunte salts resembles cases using ionic passivation at early reaction times, with observed particle coalescence. However, this observed coalescence occurs only for ~ 20 sec, while cases using purely ionic passivants continue to exhibit coalesence for hours of reaction time.[22] These comparisons support the idea that Bunte salts act as ionic passivants early in the AuNP reaction, while forming strong, covalent linkages on the final particle surfaces.

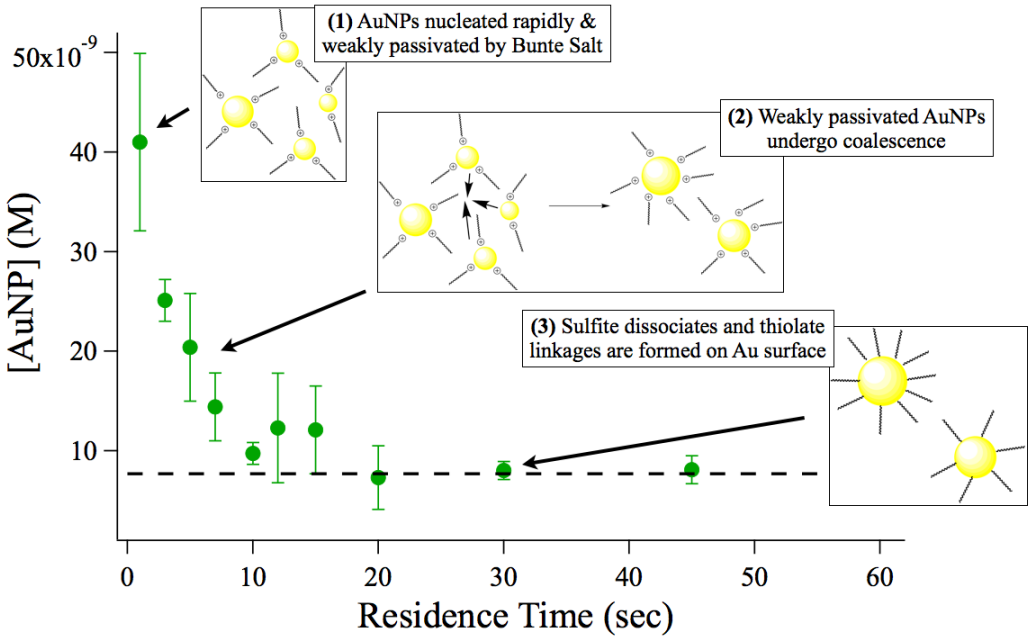

Figure 5. Hypothesized model for AuNP growth using Bunte salt ligands. Nucleation occurs when Au salt is introduced to $NaBH_4$ in the presence of Bunte salt ligand. This process is not well understood, but occurs very rapidly (<150 ms). After the nuclei are formed, Bunte salt ligands weakly associate with the particle surface in their ionic form. The weakly passivated AuNPs proceed to grow through a coalescence pathway. As the reaction progresses, the weakly-bound Bunte salt functionalities are converted to thiolate linkages as sulfite dissociates from the ligand substrate, more strongly passivating the particle surface. Thus, the particles become more stable as the reaction proceeds, until ~ 20 sec when sufficient Bunte salt has converted to thiolate to prevent further coalescence. Thus, by ~20 sec reaction time the AuNPs reach their final size distribution.

This work demonstrates *in situ* observation of AuNP reactions by SAXS and UV/vis, utilizing a microreactor system to enhance mixing. We have shown particle growth occurs rapidly in this system, where AuNPs of appreciable size (d_{CORE} ~ 1.8 nm)

are present by 150 ms reaction time. This rapid NP formation corresponds well to studies using $NaBH_4$ as reducing agent.[22] We have also shown that AuNPs grow through a coalescence mechanism, where a decrease in particle concentration is observed, consistent with the works of Polte, et al. that use weakly-passivating ligands.[6,21] Notably, a study that used strongly passivating polymeric ligands showed no evidence of coalescence.[31] Collectively, these findings suggest that the ligand identity has a significant impact on the mechanism of growth in AuNP systems. Specifically, Bunte salts are unique ligands due to their ionic passivation during particle growth and covalent passivation of final products.

APPENDIX A

SUPPORTING INFORMATION FOR CHAPTER II

Additional Characterization Data for the Four Au Nanoparticle Standards Used in this Study

Ex situ UV-vis data were collected in tandem with solution deposition onto TEM grids. These data confirmed nanoparticle identity and provided a link between TEM and *in situ* UV-vis data.

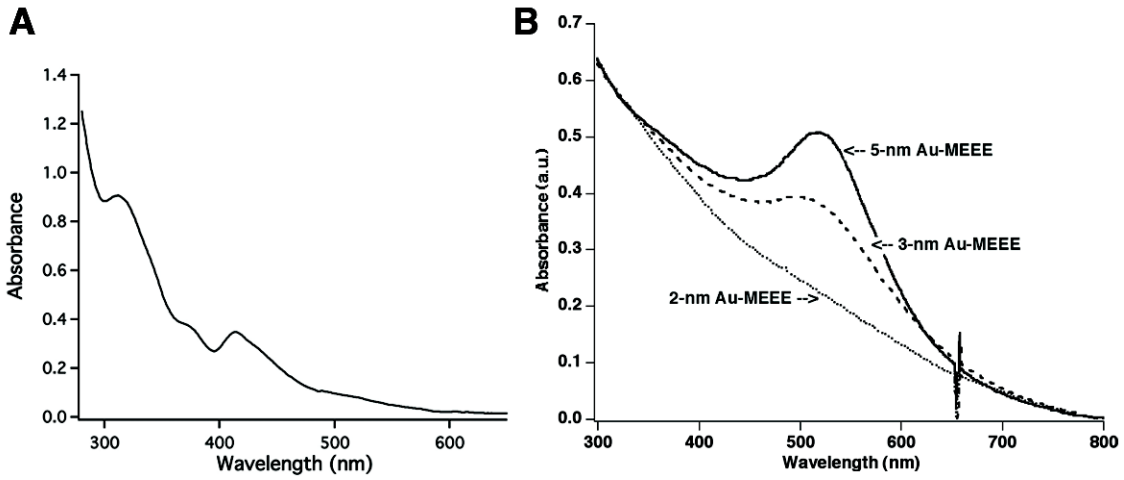

Figure S1. *Ex situ* UV-visible absorbance spectra for (A) Au_{11} and (B) 2nm-AuNP-MEEE, 3nm-AuNP-MEEE, and 5nm-AuNP-MEEE samples. Note that the peak at ~655nm in (B) is an artifact due to poor subtraction of the D-alpha feature from the deuterium spectrum.

TEM micrographs were taken for each of the four Au nanoparticle standards. The micrographs shown here are representative images of the larger data sets. A major goal of collecting these data was to correlate TEM size analysis with SAXS size analysis.

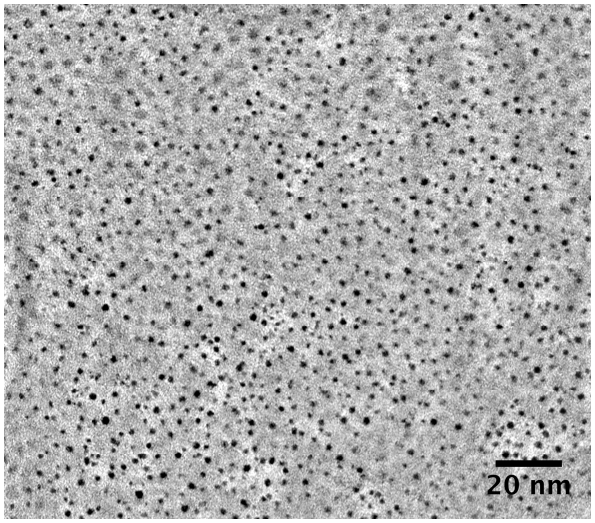

Figure S2. Processed TEM micrograph of recrystallized Au_{11} sample.

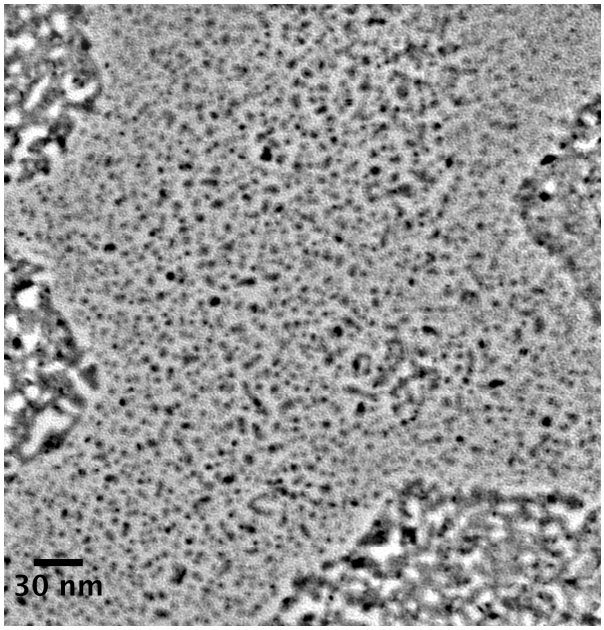

Figure S3. Processed TEM micrograph of 2nm-AuNP-MEEE sample. Note the significant degree of aggregation and/or agglomeration.

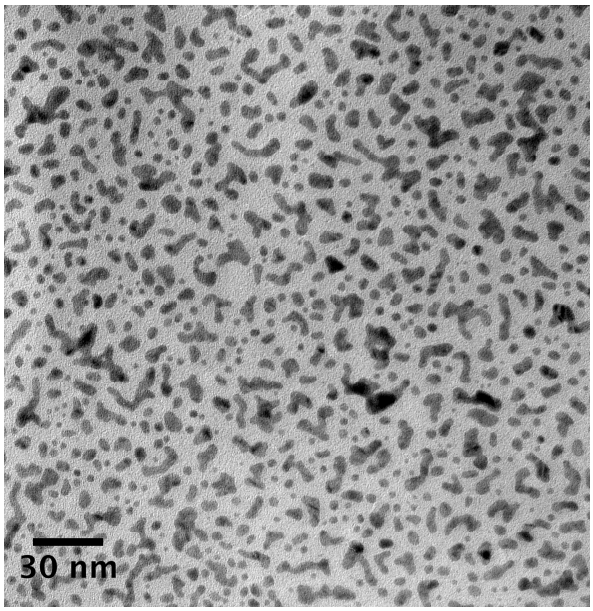

Figure S4. Processed TEM micrograph of 3nm-AuNP-MEEE sample. While it is a concern that this TEM micrograph shows a number of non-spherical particles, UV-vis analysis suggests that neither aggregation nor agglomeration are occurring in solution. If either were occurring in solution, a λ_{max} plasmon shift or a baseline rise would be evident in the UV-vis spectrum. Since neither occurred, we concluded that these non-spherical particles are the result of deposition artifacts. Thus, when these micrographs were processed, each counted particle is analyzed for circularity and the non-spherical particles are filtered out. While this does decrease the number of particles counted, this micrograph was only one of four analyzed to provide size analysis for this sample. In this particular micrograph, about half of the particles counted passed our circularity criteria, providing 454 counted particles in this image alone.

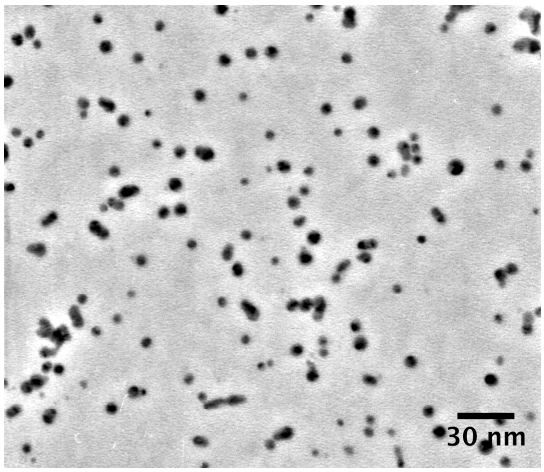

Figure S5. Processed TEM micrograph of 5nm-AuNP-MEEE sample.

SAXS Data to Identify Optimal Solvents for Flow Experiments

These data were collected and analyzed to determine the solvents that would provide minimal scattering backgrounds for SAXS experiments. Water and methanol were identified as the most desirable solvents of this selection based upon the SAXS data.

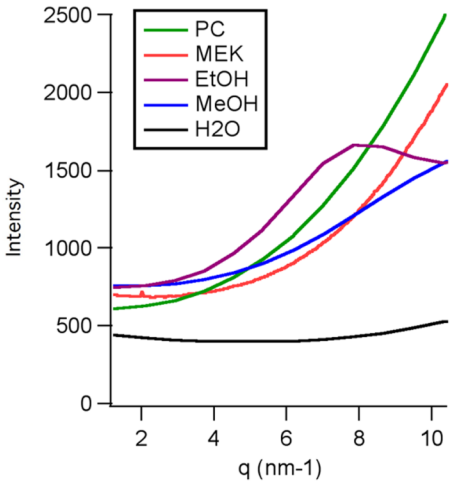

Figure S6. Comparison of X-ray scattering patterns from selected solvents. PC – propylene carbonate, MEK – methyl ethyl ketone, EtOH – ethanol, MeOH – methanol, H2O – water. The low scattering intensity of water across this q range makes it a desirable solvent for SAXS studies.

APPENDIX B

SUPPORTING INFORMATION FOR CHAPTER III

Materials and Analytical Methods

Hydrogen tetrachloroaurate hydrate ($HAuCl_4 \bullet xH_2O$, 99.9%) was purchased from Strem and used as received. Water used for syntheses was purified with a Barnstead NANOpure filtration system (18.2 MΩ resistivity). Bunte Salt ligands were prepared using known procedures, or slight modifications thereof.[1] Briefly, 1 molar equivalent of appropriate alkyl halide precursor was dissolved in nanopure water. Sodium thiosulfate (0.8 molar equivalents) was added and the solution was refluxed for 3 hours. Water was removed *in vacuo*, then the crude product was dissolved in ethanol and filtered to remove salt impurities. All other reagents and solvents were purchased from Sigma-Aldrich or Macron Chemicals and used as received.

The nanoparticle sizes in solution were determined by SAXS. Details are provided in our recent publication.[2] Briefly, AuNP samples were analyzed as synthesized and exposed to monochromated X-rays from a Long Fine Focal spot (LFF) sealed X-ray tube (Cu 1.54 Å) powered by a generator at 2 kW focused by multilayer optics, measured with a Roper CCD in a Kratky camera. The Anton Paar SAXSess, in line collimation mode, was set to average 50 scans of 20 sec for all samples. The corresponding dark current and background scans were subtracted from the data before desmearing was performed using the beam profile in Anton Paar SAXSQuant software. The desmeared

data were imported to IGOR Pro (v. 6.22A) software for modeling with 3rd party macros. The size distribution of the sample was determined by using the Modeling II macros in the IRENA package (v. 2.49).[3] The SAXS patterns were fitted using least-squares fitting (LSQF), a size distribution model, a spheroidal form factor (Aspect Ratio = 1), a Gaussian distribution, and a dilute system (Structure Factor = 1). For each sample, reported polydispersity and average core size values were determined through optimization of volume, mean size, and distribution width values to produce the lowest χ^2 value for the model fit to the data.

Transmission electron microscopy (TEM) was performed on an FEI Tecnai Spirit instrument, operating at 120kV accelerating voltage. Amine-functionalized SiO_2 SMART Grids (Dune Sciences) were used for all TEM analysis. TEM grids were prepared by floating the grid on top of a small droplet of the as-synthesized AuNP sample for ~ 30 sec. After removal from the droplet excess liquid was wicked away using a Kimwipe. TEM images were processed using Fiji software as discussed previously.[4] All AuNP samples were analyzed by UV/visible spectroscopy (Ocean Optics) for determination of particle concentration and qualitative determination of particle stability. Ligand precursors and final Bunte Salt products were analyzed by ^{1}H NMR (300 MHz, Varian). For XPS and TGA analysis, excess ligand and salts were removed from solution by diafiltration using a 75 kDa membrane (Pall).[5] XPS spectra were taken at 20 eV pass energy on a ThermoFisher ESCALab 250 with a monochromated Al K-alpha, using a 400 μm spot size. Spectra were corrected to Au 4f at 84.95 eV. Peak fitting was performed using ThermoFisher Avantage software. TGA measurements were conducted on a TA

Instruments Q500 TGA under nitrogen atmosphere. Samples were run from 25°C to 500°C at a ramp rate of 10°C/min. Gold nanoparticle samples were prepared by placing ~ 0.5 - 2 mg of lyophilized nanoparticles into a tared pan. The sample was then immediately analyzed.

NMR of Bunte Salt Ligands

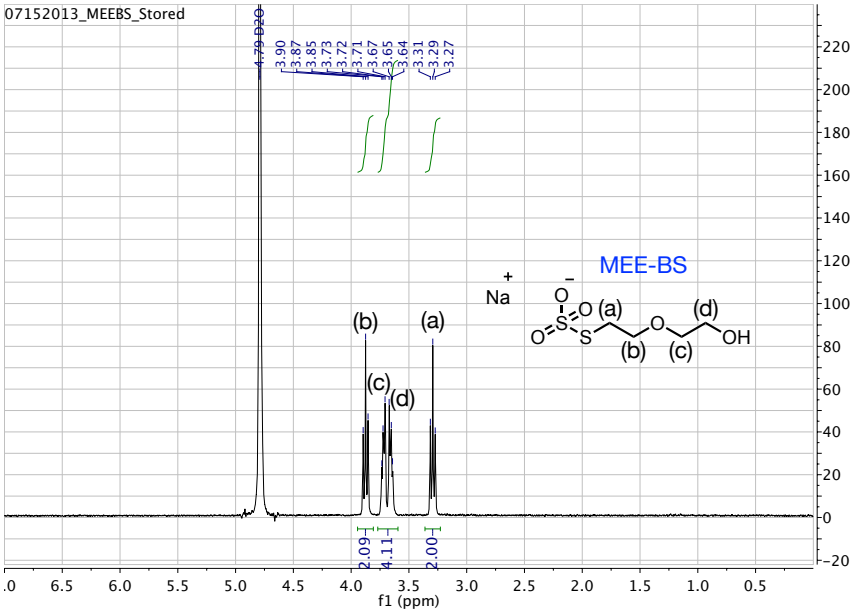

Figure S1. NMR spectrum for MEE Bunte salt ligand.

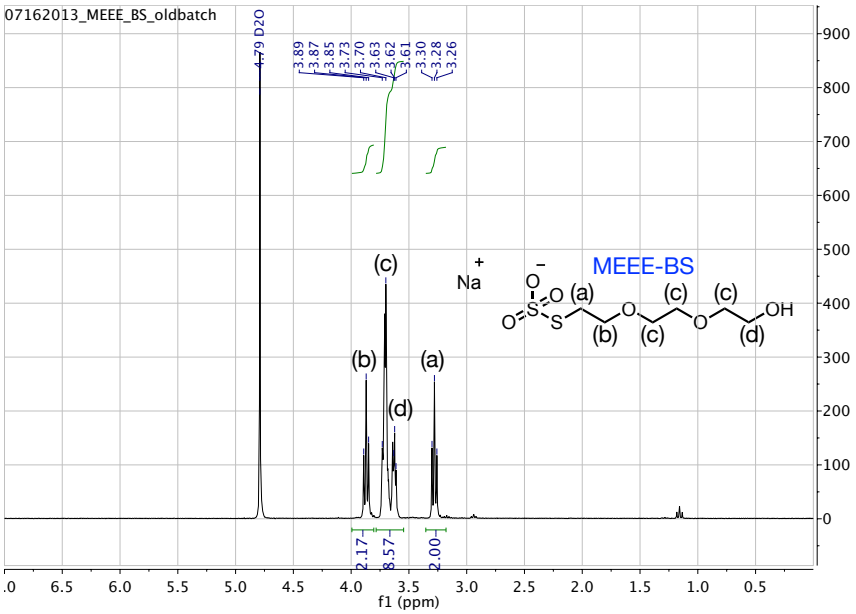

Figure S2. NMR spectrum for MEEE Bunte salt ligand.

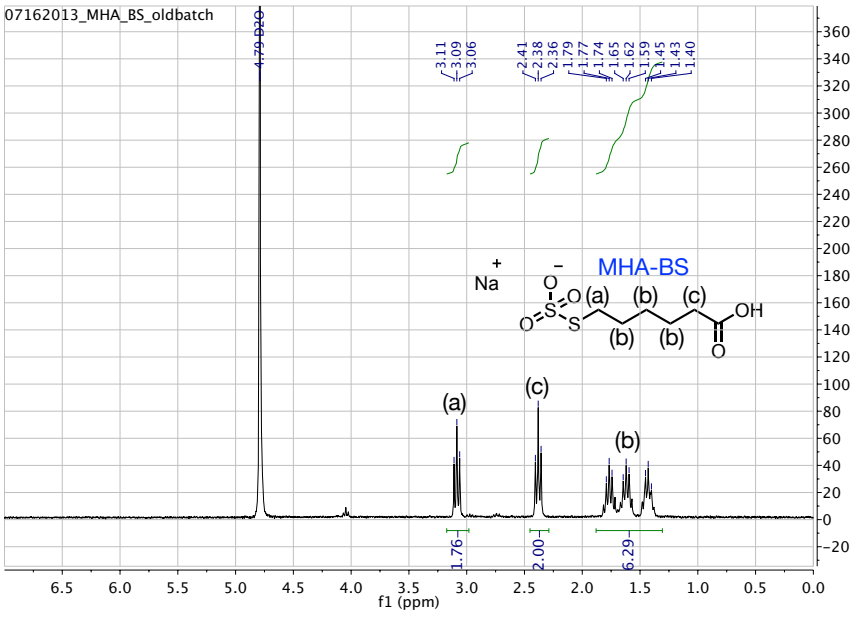

Figure S3. NMR spectrum for MHA Bunte salt ligand.

Experimental Details for Microreactor Synthesis

Three syringe pumps each equipped with 3-way distribution valves were purchased from Kloehn (Versa 6, 48k model with rotary valve). All other microreactor components were purchased from IDEX Health and Science. FEP tubing (1/16" outer diameter, 0.030" inner diameter), T-mixers (1/16", 1/4-28, 0.020" Thru, ETFE), 15 psig check valves, and appropriate fittings (1/4-28) and ferrules were assembled with the syringe pumps as shown to enable microfluidic generation of AuNPs. Tubing and T-mixers were swapped out if material deposition occurred. Solutions were pumped at a total flow rate of 60 mL/min, with tubing lengths selected to allow for sufficient mixing time in the microfluidic system.

Aqueous solutions were prepared to enable three successive microfluidic syntheses at each reaction condition. Thus, 30 mL of 5.0 mM $HAuCl_4$, 30 mL of 1.0 mM Bunte Salt ligand, and 60 mL of 1.0 mM $NaBH_4$ were prepared. A total of 0.825 mL of 1.0 M NaOH was added to these solutions, split between the $HAuCl_4$ and $NaBH_4$ solutions. The desired amount of NaOH (ranging from 0.127 mL – 0.510 mL) was first added to the $HAuCl_4$ solution, determining the initial Au(III) speciation and effectively controlling the final AuNP dimensions. Corresponding Au(III) pH values and added volumes of NaOH are summarized in Table S1. The remaining amount of total NaOH (ranging from 0.698 mL – 0.315 mL) was added to the $NaBH_4$ solution to maintain final pH of the system. It is advantageous to prepare the $HAuCl_4$ solution first, as it can take up to 20 min to reach equilibrium at high pH. Additionally, the $NaBH_4$ solution should be prepared last, as this reagent also undergoes undesirable hydrolysis in water, albeit

slowly.[6] Note that 0.012 mL of additional 1.0 M NaOH was added to the 30 mL of 1.0 mM MHA ligand solution to ensure the acid group was deprotonated at all conditions (a total of 0.837 mL base were added for these syntheses).

Table S1. Summary of NaOH volumes added to precursor solutions to tune Au(III) pH and achieve AuNP size selectivity.

Au(III) pH	Au(III) pH Abbreviation	1M NaOH added to HAuCl4 solution (mL)	1M NaOH added to NaBH4 solution (mL)
2.97	~ 3	0.127	0.698
3.93	~ 4	0.225	0.600
4.90	~ 5	0.325	0.502
5.87	~ 6	0.420	0.405
6.76	~ 7	0.510	0.315

Once the appropriate amount of base was added to the respective solutions, each of the three solutions was aspirated by the three syringe pumps as shown in Figure 1 in Chapter III. The 20 mL of $NaBH_4$ solution was dispensed at 30 mL/min, mixed with a stream of 10 mL of ligand solution flowing at 15 mL/min, mixed along a 1.64 m length of tubing (1 second of residence time), before introducing the third stream of 10 mL of Au (III) solution flowing at 15 mL/min. Two simple T-mixers were used to mix the reagents. 15 psig check valves were utilized at each of the 10 mL syringes to avoid backflow. At a total flow rate of 60 mL/min, the final mixed solution is allowed to flow through the reactor for ~ 2 seconds (~ 5 m of tubing) before being collected. Small fractions at the

beginning and end of each reaction were discarded. The microreactor system was rinsed with nanopure water three times (full aspirate/dispense cycles of the syringe pumps) after each synthesis. Each synthesis was repeated another two times, using the remainder of the prepared solutions, to determine reproducibility. After each set of three syntheses, the downstream T-mixer that introduces the Au(III) solution was replaced with a clean mixer. The used mixers are later cleaned with aqua regia and water to remove any plated Au material left behind. If any plated material was evident in the reactor tubing, it was discarded and replaced with fresh tubing.

Nanoparticle Characterization

Transmission Electron Microscopy

TEM analysis was performed across the size range for each working curve shown to determine particle morphology. AuNPs synthesized at all pH values were observed to be spherical. The following are representative images for each AuNP working curve.

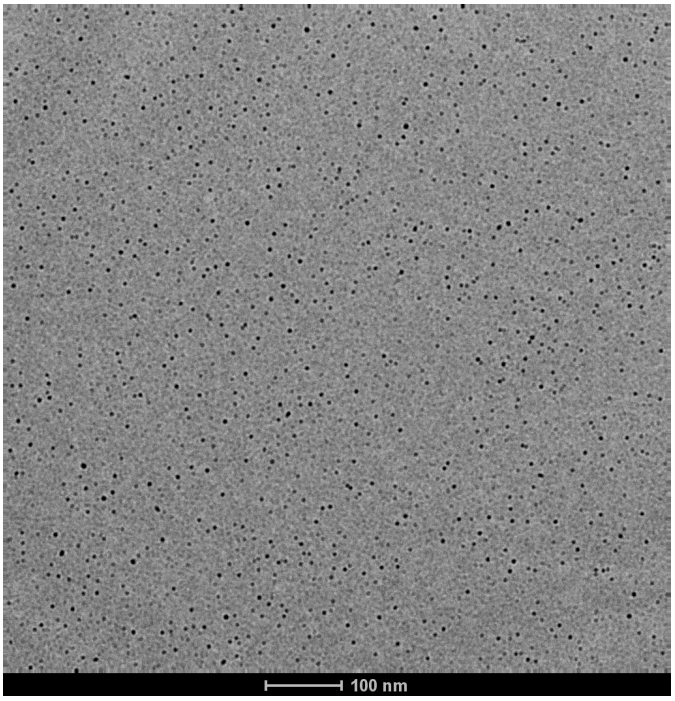

Figure S4. TEM micrograph of MHA-passivated AuNPs synthesized at Au(III) pH ~ 3.

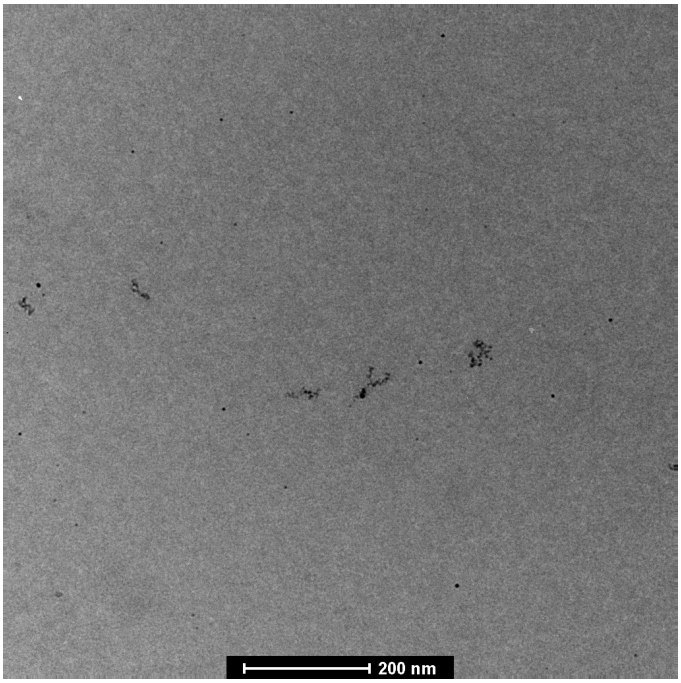

Figure S5. TEM micrograph of MHA-passivated AuNPs synthesized at Au(III) pH ~ 7.

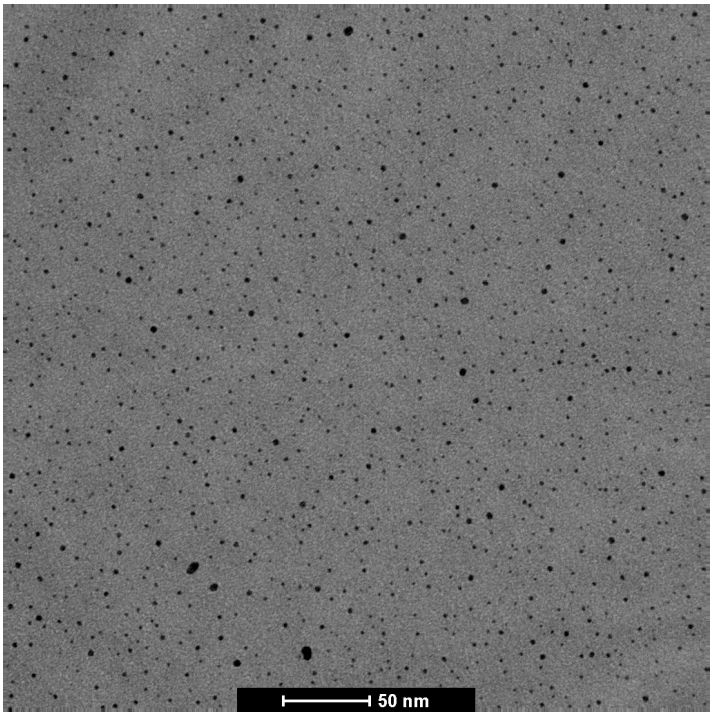

Figure S6. TEM micrograph of MEE-passivated AuNPs synthesized at Au(III) pH ~ 3.

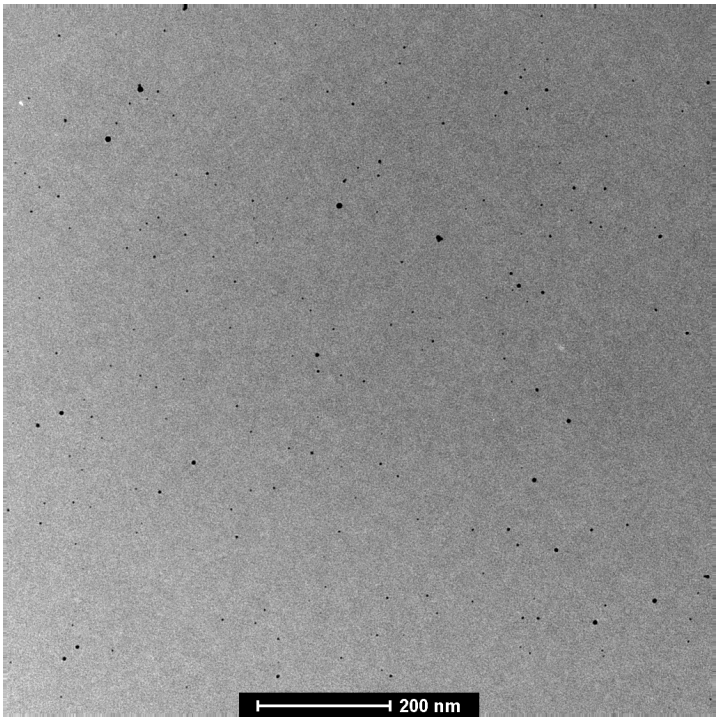

Figure S7. TEM micrograph of MEE-passivated AuNPs synthesized at Au(III) pH ~ 7.

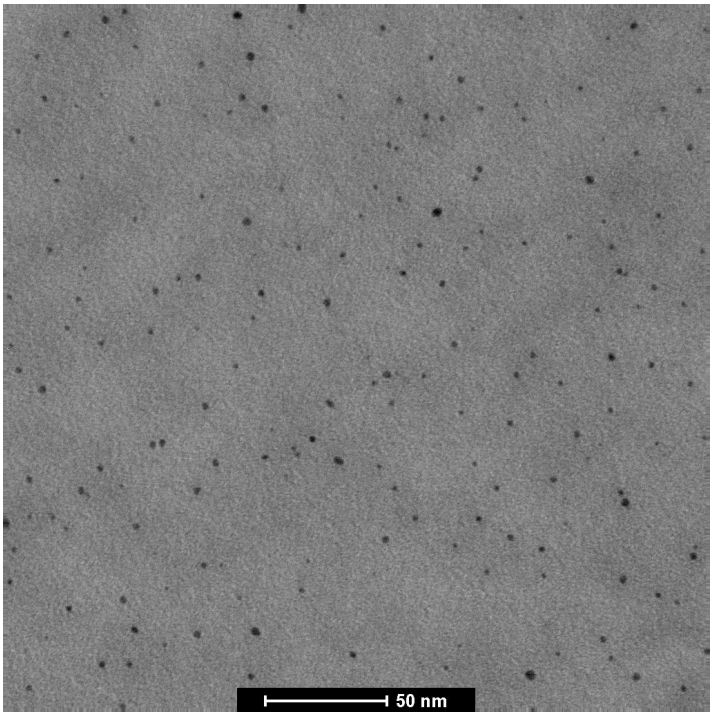

Figure S8. TEM micrograph of MEEE-passivated AuNPs synthesized at Au(III) pH ~ 3.

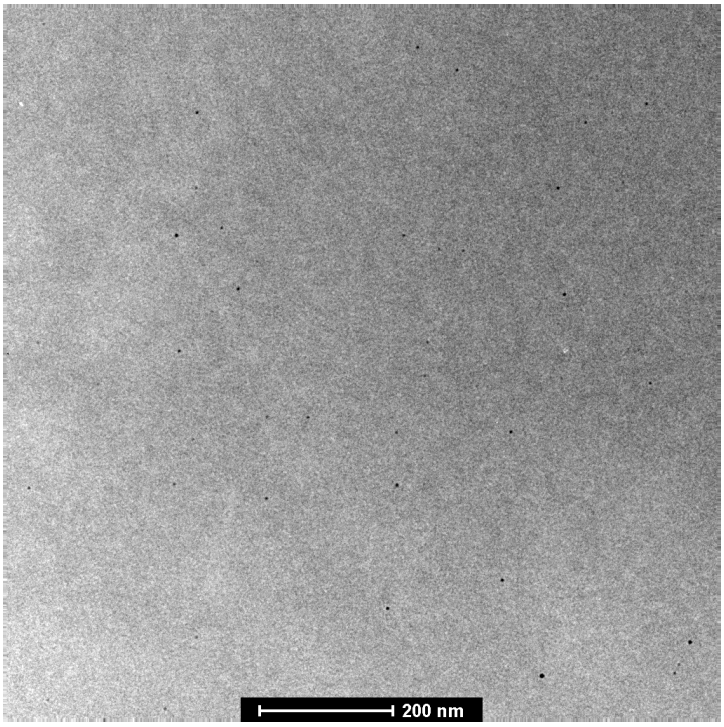

Figure S9. TEM micrograph of MEEE-passivated AuNPs synthesized at Au(III) pH ~ 7.

Thermogravimetric Analysis of AuNPs

TGA data were collected to determine the relative coverage of ligand on AuNPs at the extremes of the observed pH range. Beginning and end of ligand mass loss was determined by identifying when the derivative of mass loss vs. temperature had a slope of zero before and after the first major mass loss peak. All values match well to expected values.

Table S2. Comparison of calculated expected mass loss and observed mass loss for thiolate-passivated AuNPs.

Sample	Expected Mass Loss[a]	Observed Mass Loss
MEE-AuNPs pH ~ 3	10.5%	11.4%
MEE-AuNPs pH ~ 7	4.2%	5.1%
MEEE-AuNPs pH ~ 3	11.9%	15.8%
MEEE-AuNPs pH ~ 7	6.1%	6.0%
MHA-AuNPs pH ~ 3	13.1%	13.1%
MHA-AuNPs pH ~ 7	4.4%	6.1%

a - Expected mass loss calculated for complete thiolate monolayer on AuNP surface

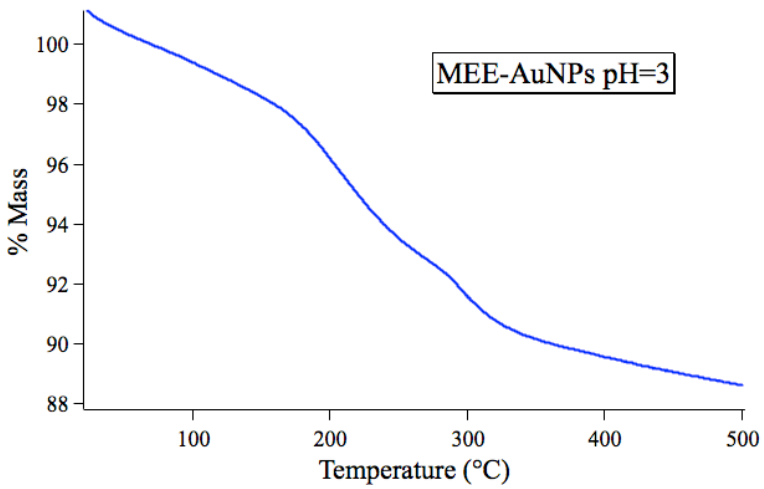

Figure S10. TGA data for AuNPs synthesized at Au(III) solution pH ~ 3 using MEE Bunte salt ligand.

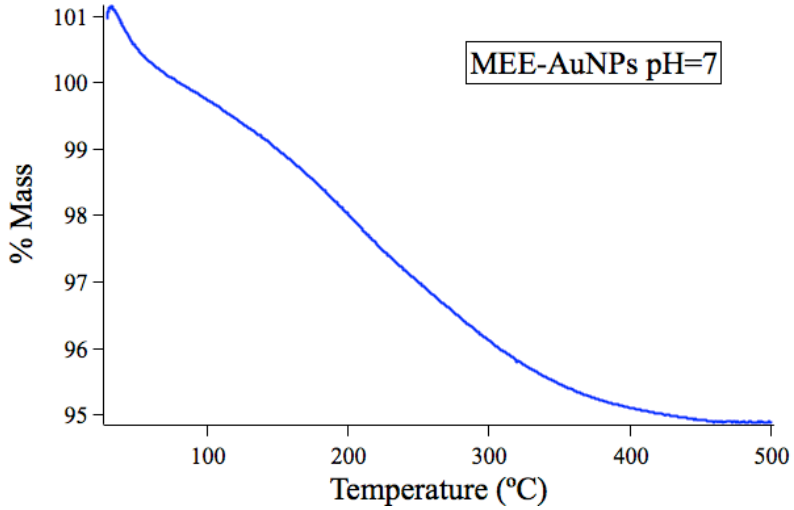

Figure S11. TGA data for AuNPs synthesized at Au(III) solution pH ~ 7 using MEE Bunte salt ligand.

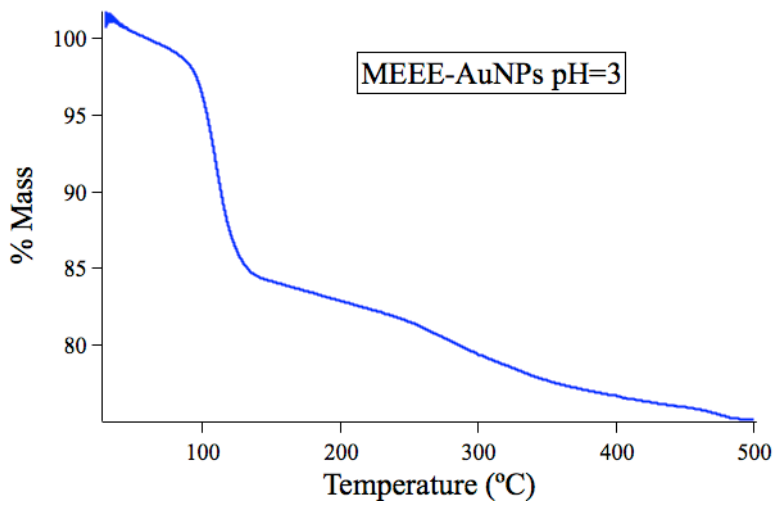

Figure S12. TGA data for AuNPs synthesized at Au(III) solution pH ~ 3 using MEEE Bunte salt ligand.

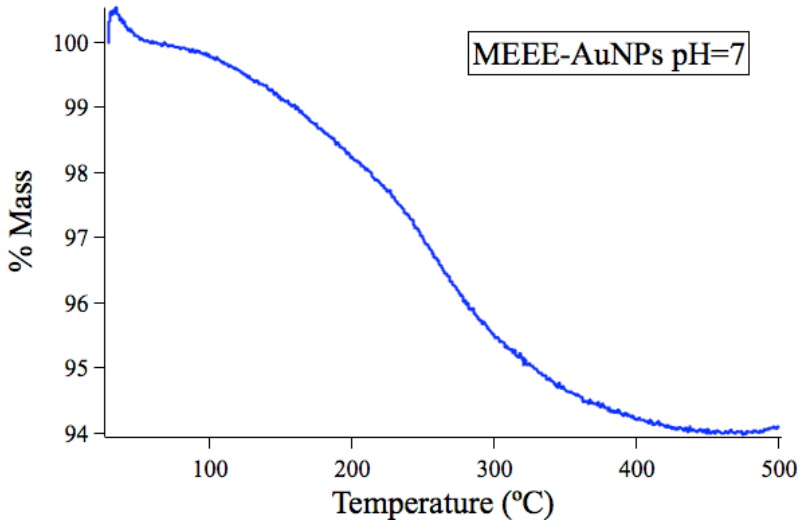

Figure S13. TGA data for AuNPs synthesized at Au(III) solution pH ~ 7 using MEEE Bunte salt ligand.

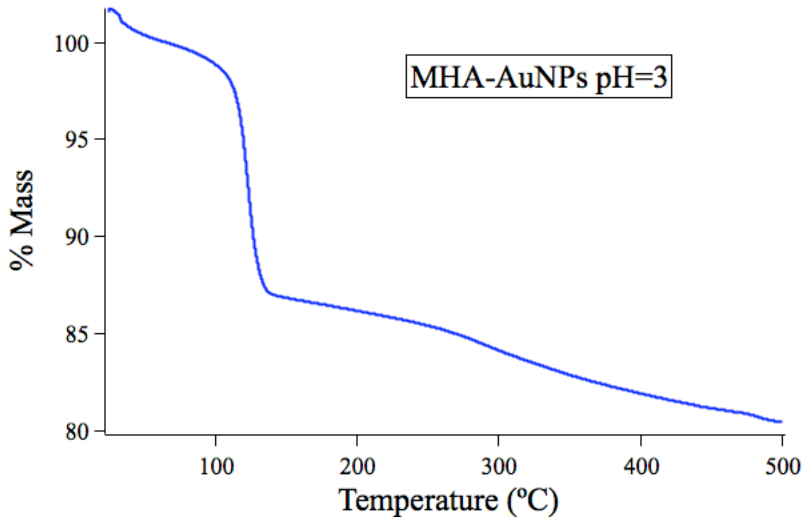

Figure S14. TGA data for AuNPs synthesized at Au(III) solution pH ~ 3 using MHA Bunte salt ligand.

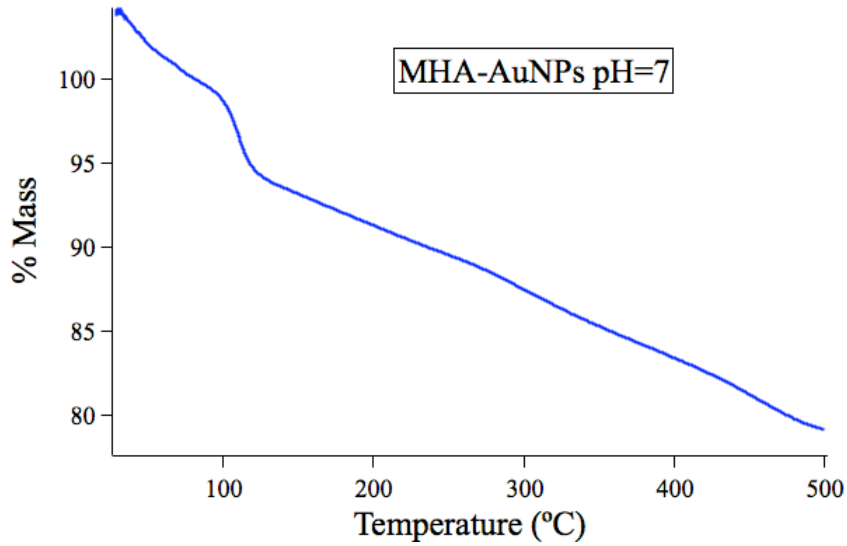

Figure S15. TGA data for AuNPs synthesized at Au(III) solution pH ~ 7 using MHA Bunte salt ligand.

X-ray Photoelectron Spectroscopy

XPS spectra were collected to ensure that thiolate linkages had been formed on the AuNP surface for AuNPs from each of the working curves. Peaks at ~163 eV correspond to thiolate linkages to the AuNP surface. Peaks observed at ~169 eV correspond to small amounts of oxidized sulfur, either from atmospheric oxidation or residual thiosulfate trapped in the ligand shell. These oxidized peaks comprise less than 10% of the sulfur in all cases.

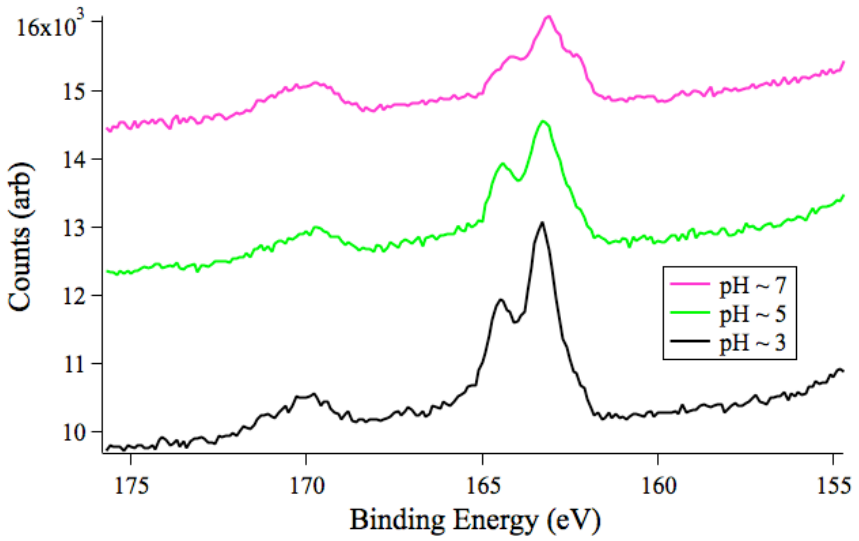

Figure S16. Representative XPS spectra for AuNPs synthesized using MEE Bunte salt ligand.

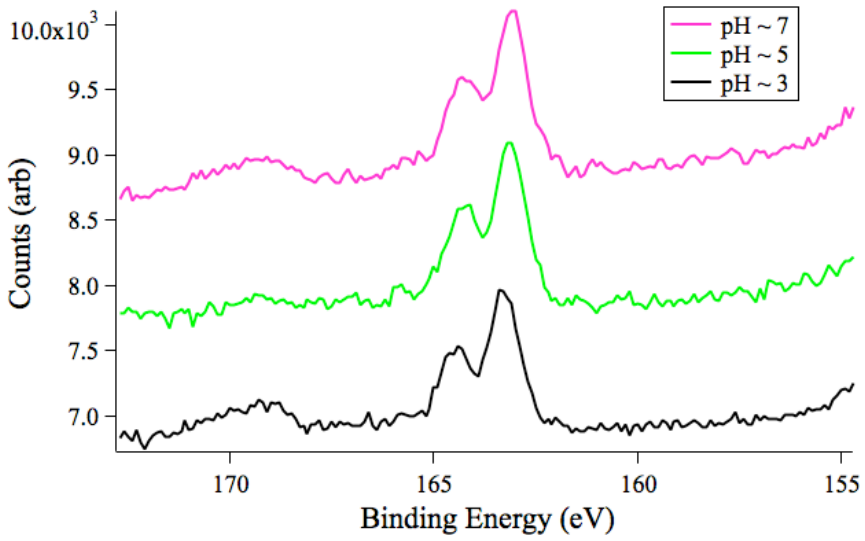

Figure S17. Representative XPS spectra for AuNPs synthesized using MEEE Bunte salt ligand.

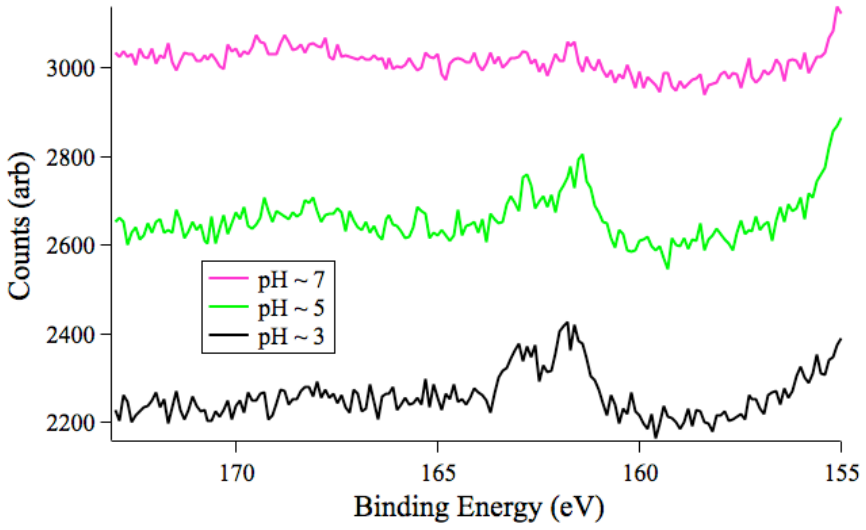

Figure S18. Representative XPS spectra for AuNPs synthesized using MHA Bunte salt ligand. Signal-to-noise is lower for these samples than the MEE- or MEEE-functionalized AuNPs due to a shorter collection time on the XPS instrument.

Determining Au(III) pH Dependence

UV/visible Spectroscopy

UV/vis was performed to corroborate other analyses and ensure that particles were stable in solution without flocculation. A plasmon lambda-max shift to higher wavelengths (~ 500 nm to ~ 520 nm across the range) as Au(III) solution pH increases was observed in all sample sets. This shift to higher lambda-max corresponds to observed increases in particle diameter by SAXS.

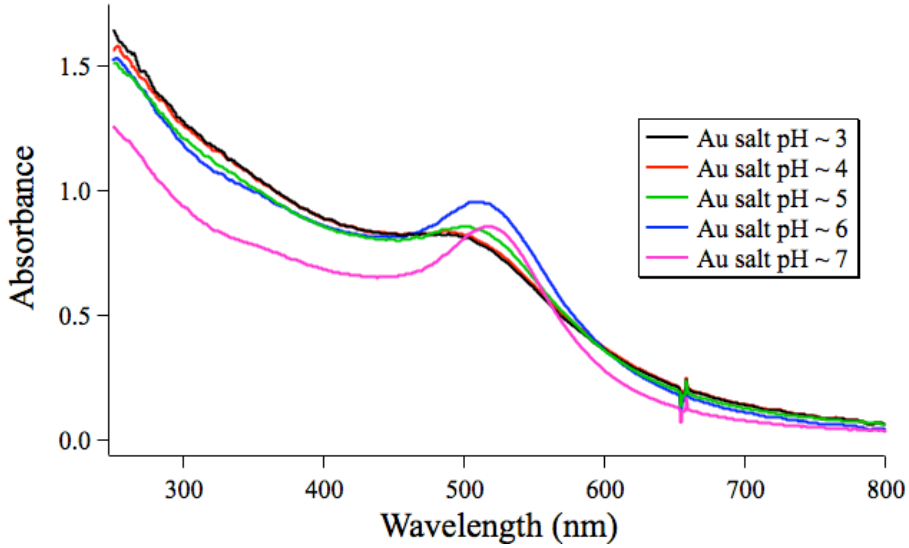

Figure S19. Representative UV/vis spectra of AuNPs synthesized with MEEE Bunte salt ligands. The samples shown were included in the sample set used to determine the MEEE Bunte salt working curve.

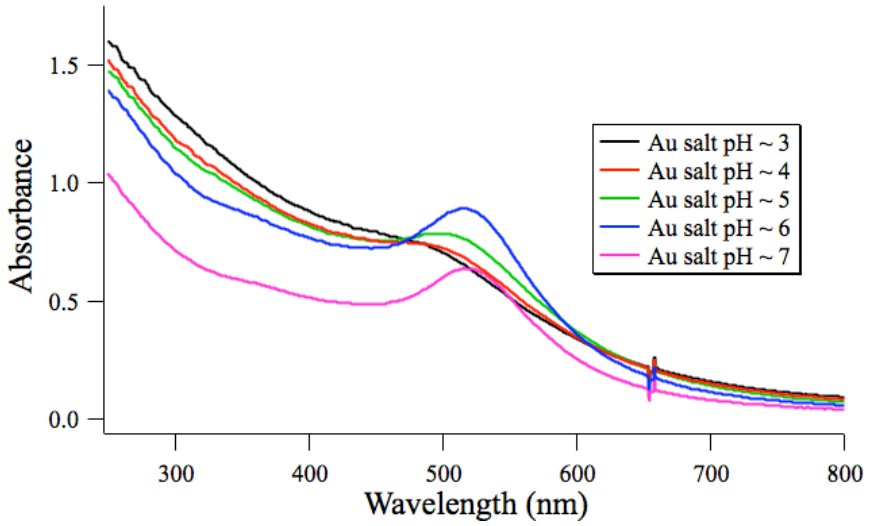

Figure S20. Representative UV/vis spectra of AuNPs synthesized with MEE Bunte salt ligands. The samples shown were included in the sample set used to determine the MEE Bunte salt working curve.

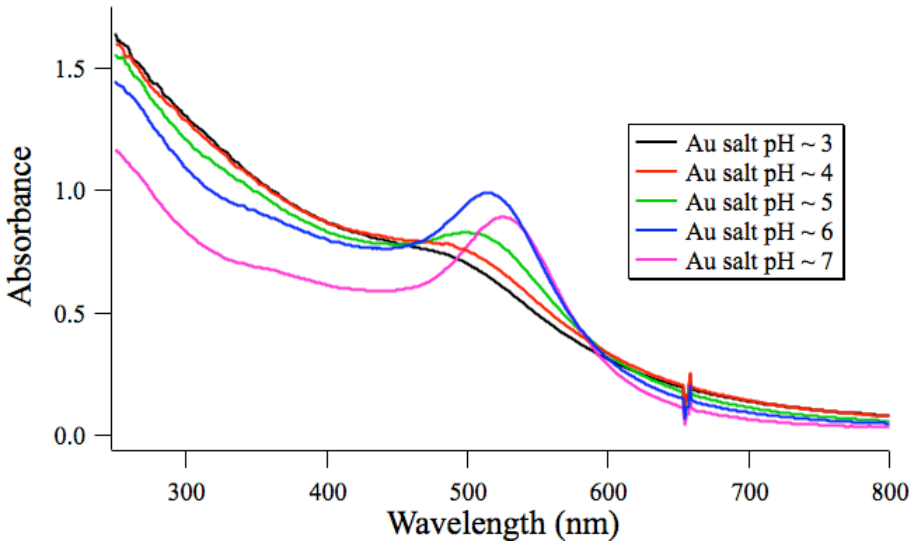

Figure S21. Representative UV/vis spectra of AuNPs synthesized with MHA Bunte salt ligands. The samples shown were included in the sample set used to determine the MHA Bunte salt working curve.

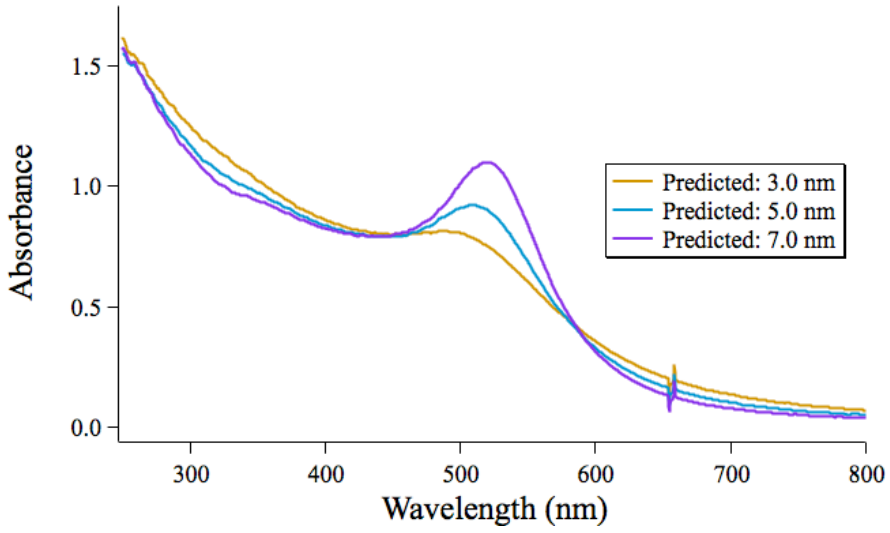

Figure S22. Representative UV/vis spectra of AuNPs synthesized with predictive sizes using MHA Bunte salt ligands. The samples shown were not included in the working curve fit, but match well to the observed trend (Figure 3 in Chapter III).

Raw SAXS Data

All working curves were based off of modeled SAXS data. Below are representative SAXS patterns for each pH point on the three working curves shown in this study. Data points in these graphs represent raw data while solid traces represent models from which size distributions were determined. Traces are offset for clarity.

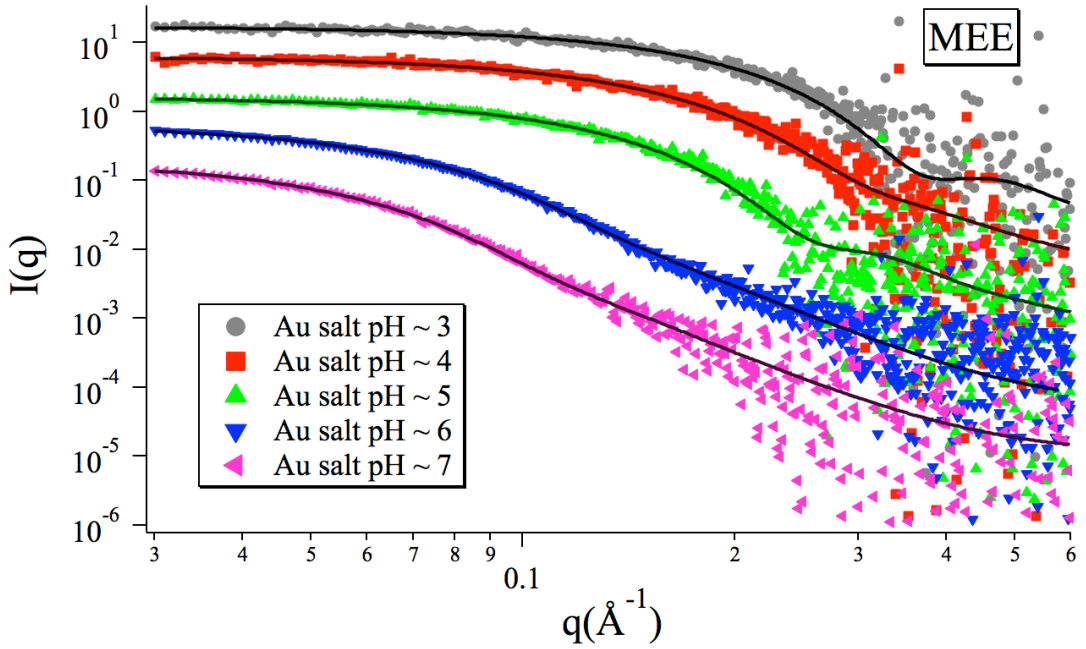

Figure S23. Raw SAXS data for the AuNP working curve using MEE Bunte Salt as ligand.

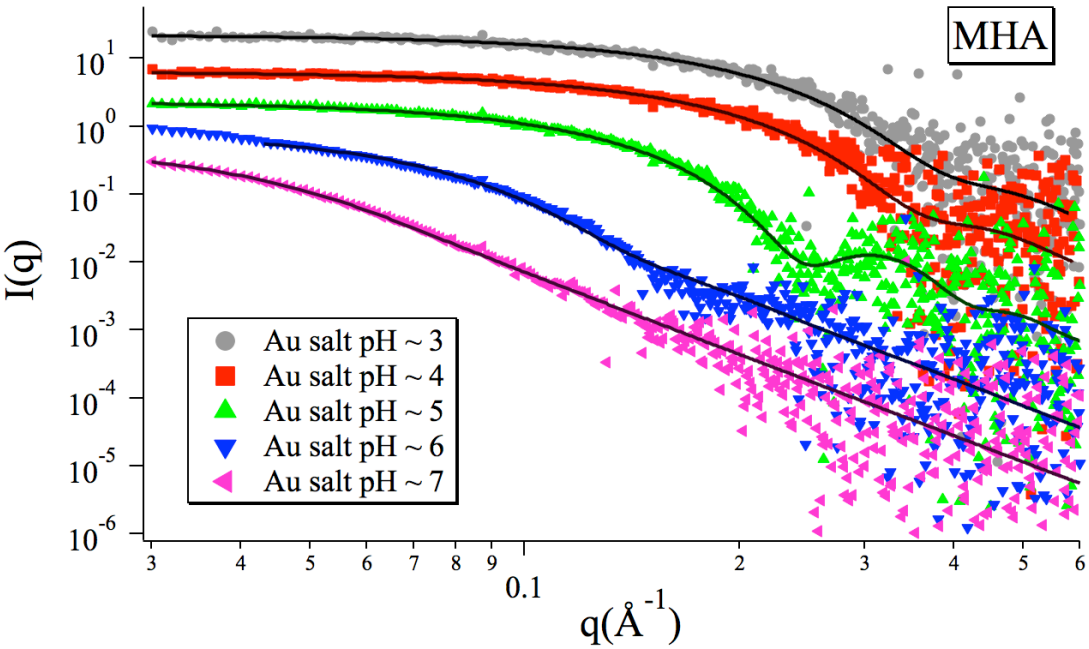

Figure S24. Raw SAXS data for the AuNP working curve using MHA Bunte Salt as ligand.

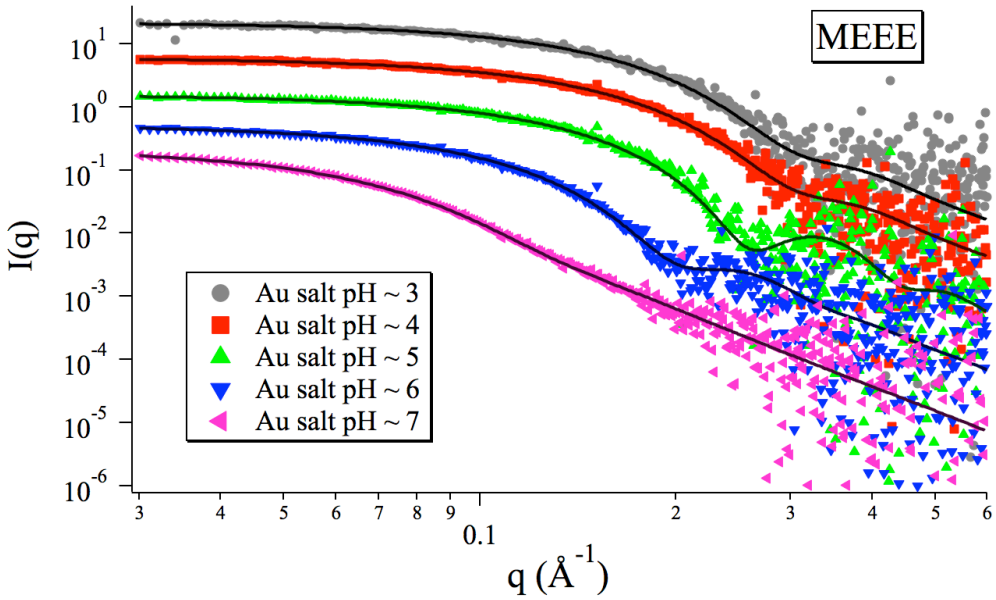

Figure S25. Raw SAXS data for the AuNP working curve using MEEE Bunte Salt as ligand.

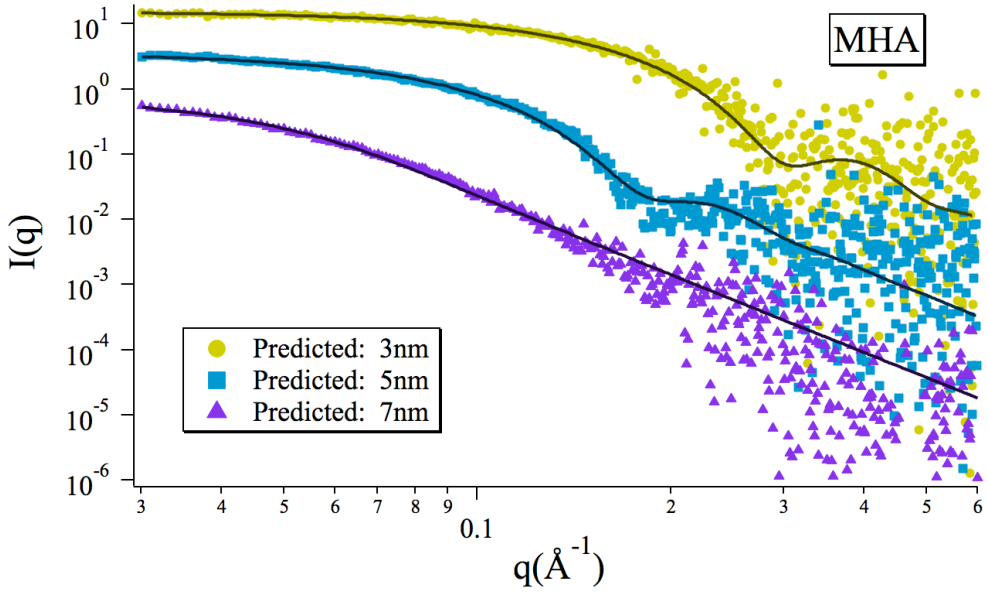

Figure S26. Raw SAXS data for the predictive AuNP syntheses (expected 3.0, 5.0, and 7.0 nm) using MHA Bunte Salt as ligand. Modeled AuNP diameters were found to be 3.0, 4.9, and 6.9 nm.

Nanoparticle core sizes were determined by SAXS for each sample produced for a given ligand across the range of pH from 3 to 7. Smooth working curves through these data were produced using a 3-variable polynomial function. For the following, equation (1) corresponds to the MHA ligand working curve while equations (2) and (3) correspond to MEE and MEEE ligand working curves, respectively:

$$D = 0.486(x^2) – 3.09e\text{-}2(x) + 7.12 \quad (1)$$

$$D = 0.366(x^2) – 2.26e\text{-}2(x) + 5.94 \quad (2)$$

$$D = 0.0716(x^3) - 0.722(x^2) + 2.60(x) - 0.410 \quad (3).$$

D represents average AuNP core diameter as determined by SAXS. The value x represents the Au(III) solution pH. Interested readers should note that size trends using other ligands might fit functional forms other than the polynomial fits utilized here. Fitted curves, however, should be smooth with no local minima or maxima between data points. To determine the appropriate amount of NaOH to add to a 30 mL solution of 5.0 mM $HAuCl_4$, a titration using 1.0 M NaOH was performed. Corresponding Au(III) solution pH values for NaOH additions are listed below in Table S3. Working curves were based on AuNP diameter vs. Au(III) solution pH. This titration was used to determine appropriate volumes of NaOH to add to adjust Au(III) solution pH to desired values.

Table S3. Titration of 1.0 M NaOH into 30 mL of 5.0 mM $HAuCl_4$.

Volume 1M NaOH (uL)	Au(III) pH	Volume 1M NaOH (uL)	Au(III) pH	Volume 1M NaOH (uL)	Au(III) pH
0	2.47	140	3.09	280	4.53
10	2.47	150	3.16	290	4.64
20	2.5	160	3.24	300	4.78
30	2.53	170	3.33	310	4.87
40	2.57	180	3.43	320	4.98
50	2.6	190	3.54	330	5.04
60	2.64	200	3.68	340	5.17
70	2.68	210	3.76	350	5.26
80	2.72	220	3.87	400	5.75
90	2.77	230	3.98	450	6.17
100	2.82	240	4.09	500	6.59
110	2.88	250	4.2	550	7.02
120	2.94	260	4.31		
130	3.00	270	4.42		

Individual working curves with polydispersities

Here each working curve is shown individually to demonstrate predictive ability and observed polydispersities across the pH range. Working curve data points are solid and predictive data points are open. For each data point, 3 syntheses were performed where corresponding SAXS size analyses were averaged to determine average diameters and standard deviations.

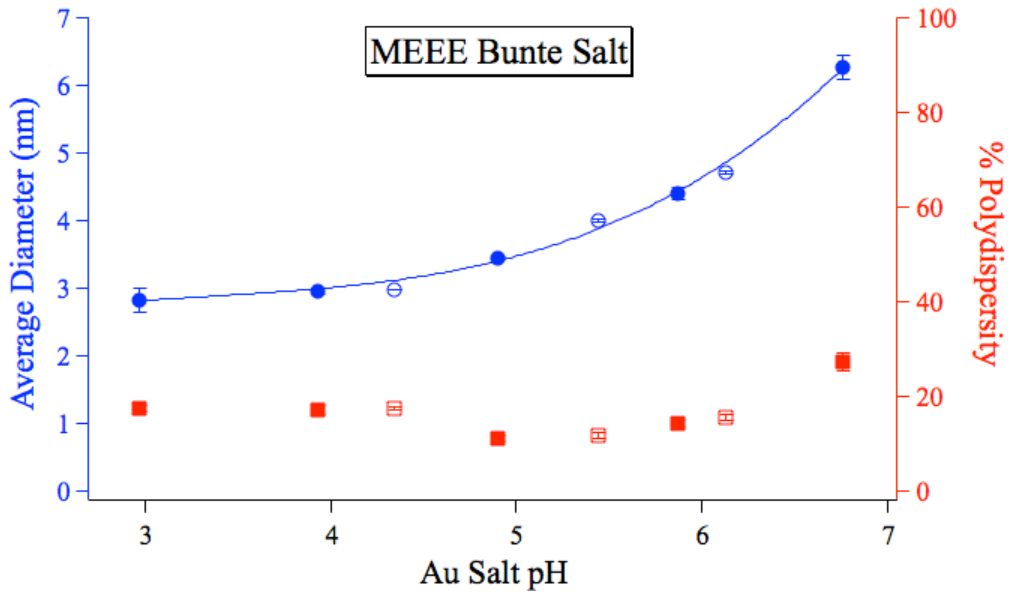

Figure S27. Combined SAXS data for AuNP working curve using MEEE Bunte salt as ligand.

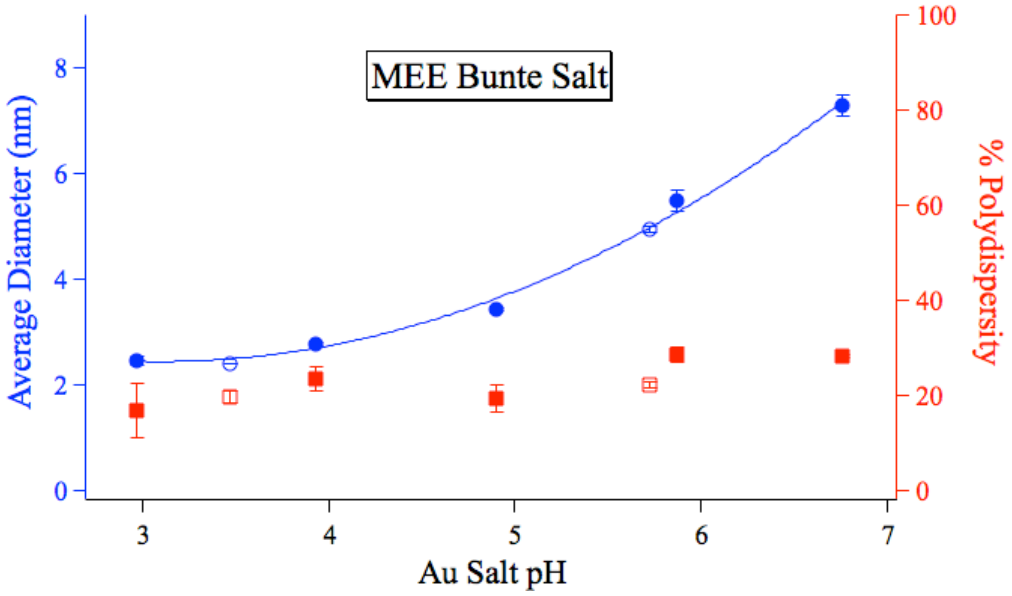

Figure S28. Combined SAXS data for AuNP working curve using MEE Bunte salt as ligand.

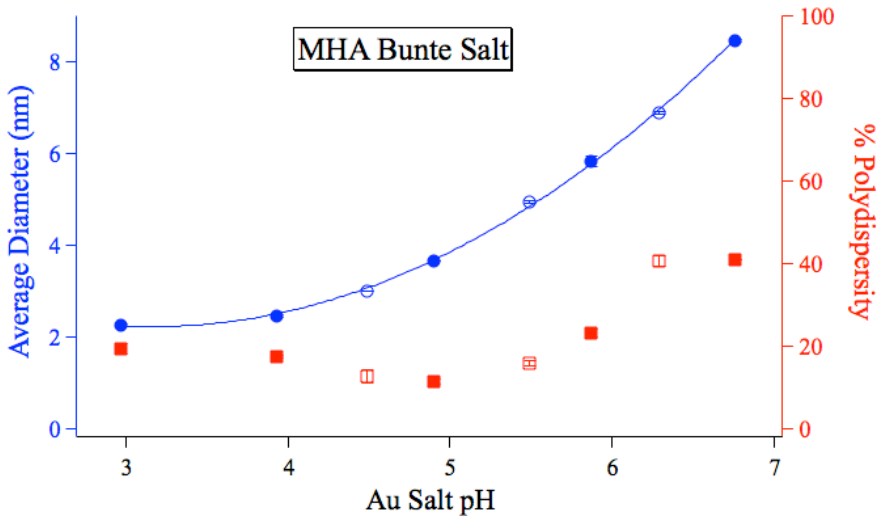

Figure S29. SAXS data for AuNP working curve using MHA Bunte salt as ligand.

Au(III) Speciation as a Function of pH

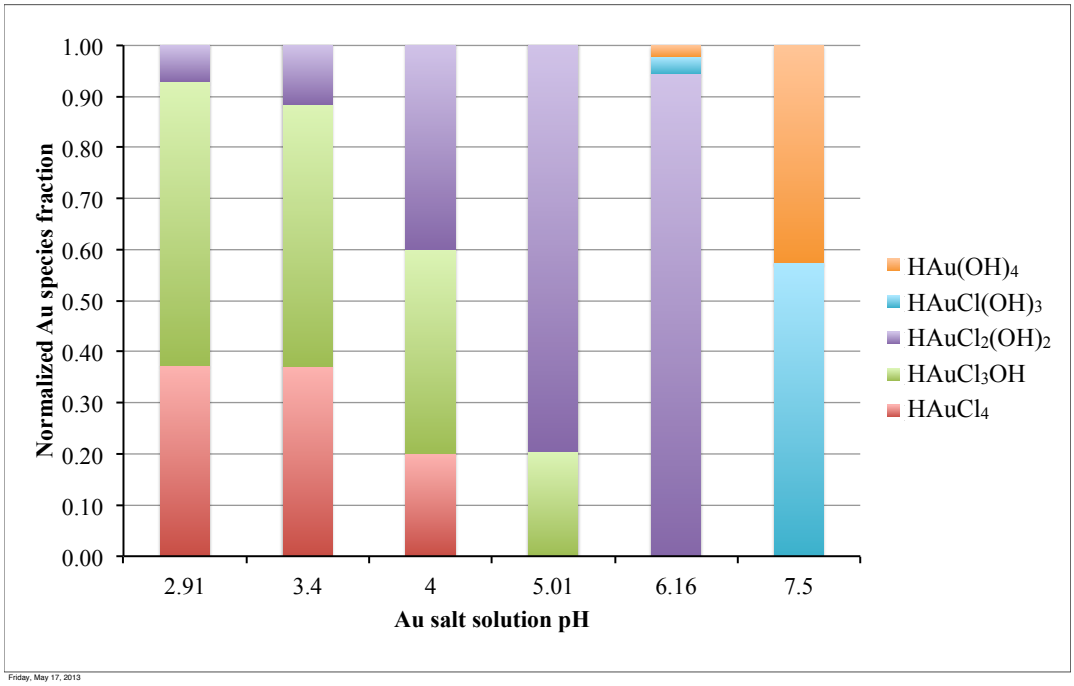

Figure S30. Normalized ratios of Au(III) species at varied pH, determined from ion chromatography by Wang et al.[7] Species with more chloro ligands exhibit higher reduction potentials and contribute more to AuNP formation.

Attempts to Vary Core Size in the Presence of Thiols and Disulfides

AuNPs were synthesized in flow using MEEE thiol ligand across the Au(III) pH range of interest (pH ~ 3 - 7) to determine if particle core size varied. AuNPs made in the presence of disulfide were only synthesized at extremes of this pH range. MEEE thiol was synthesized according to known procedures.[8] Briefly, 2 molar equivalents of thiourea were added to 1 equivalent of 2-(2-chloroethoxy)ethanol in 40 mL nanopure water with Ar(g) bubbling through solution. The solution was refluxed for 20 hours, then 20 mL of 5 M KOH was added and the solution was allowed to reflux for another 3 hours. The solution was then brought to pH ~ 1 with HCl. The acidified solution was extracted with chloroform, then the organic layer was extracted with brine solution. Chloroform was removed *in vacuo*. A 1 mM solution of MEEE thiol in sparged nanopure water was used as ligand solution in the described microfluidic synthesis (See Experimental Details above). This solution was then left open to air at pH = 10 for 48 hours to generate a 0.5 mM solution of MEEE disulfide. A second, 1 mM disulfide solution was also made in this fashion.

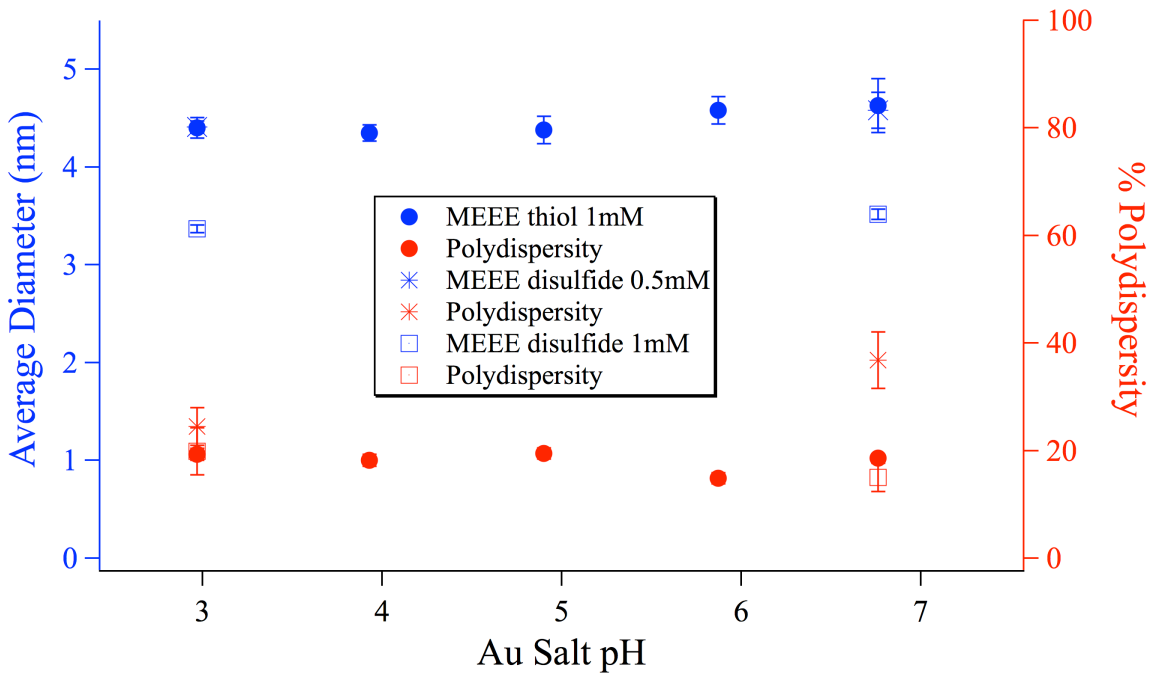

Figure S31. SAXS data of AuNPs synthesized in a microflow system across the Au(III) solution pH range of interest. No size selectivity is observed across this pH range. All syntheses performed with 1 mM MEEE thiol or 0.5 mM MEEE disulfide produce d_{CORE} ~ 4.5 nm AuNPs, though the particles made with disulfide show larger polydispersities. With a 1 mM ligand solution of MEEE disulfide, smaller (d_{CORE} ~ 3.5 nm) AuNPs are generated than with 0.5 mM disulfide solution. Note that AuNPs made with these ligands show no significant core size variation across this pH range while all Bunte salts investigated show significant differences in core diameters.

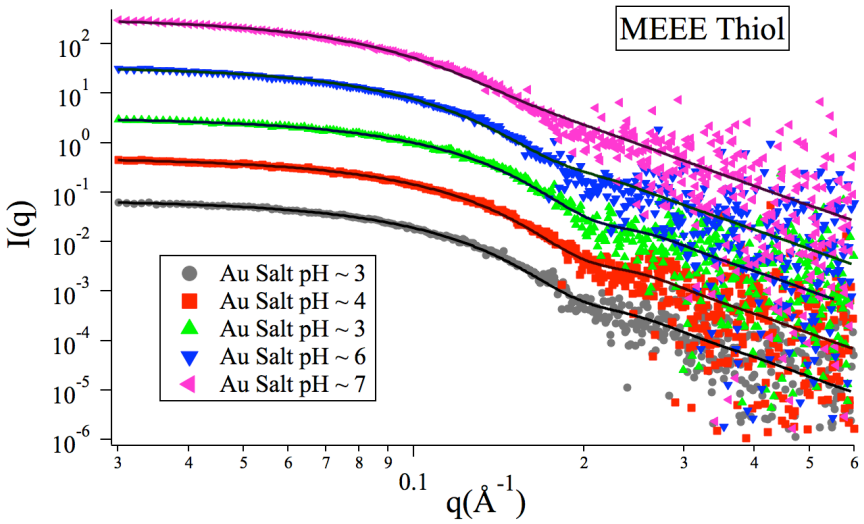

Figure S32. Raw SAXS data for AuNPs synthesized with MEEE thiol across Au(III) pH range. Models of these patterns yield average AuNP diameters that are very similar across the pH range. This result is surprising in comparison to AuNPs synthesized with analogous Bunte salt ligands where large differences in AuNP diameter are observed.

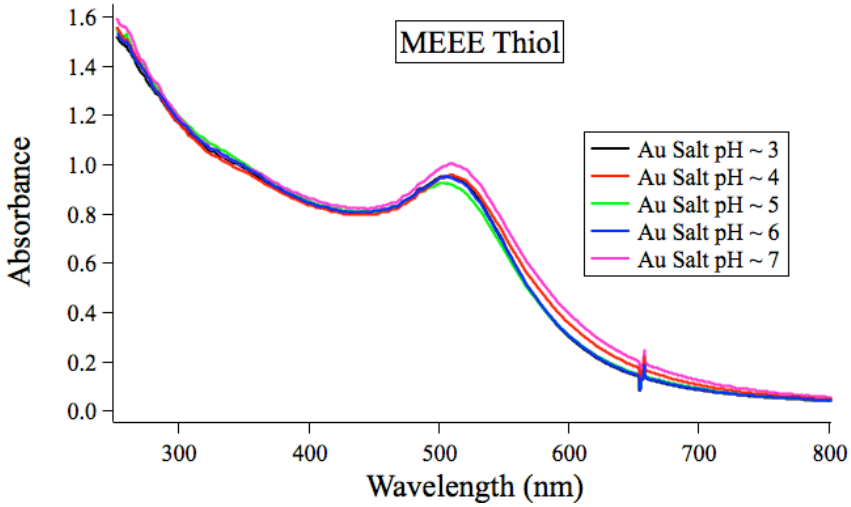

Figure S33. UV/vis spectra for AuNPs synthesized with MEEE thiol across the range of Au(III) pH ~ 3 - 7. Minimal differences in plasmon lambda max correlate well to similar observed AuNP sizes determined by SAXS.

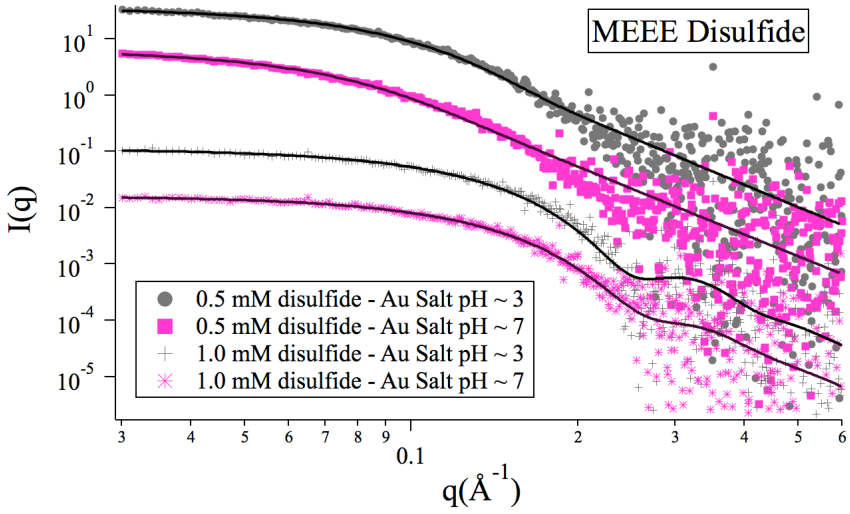

Figure S34. Raw SAXS data for AuNPs synthesized with two different concentrations of MEEE disulfide at two Au(III) pH values. Models of these patterns yield average AuNP diameters that are very similar at different pH values when the same ligand concentration is used.

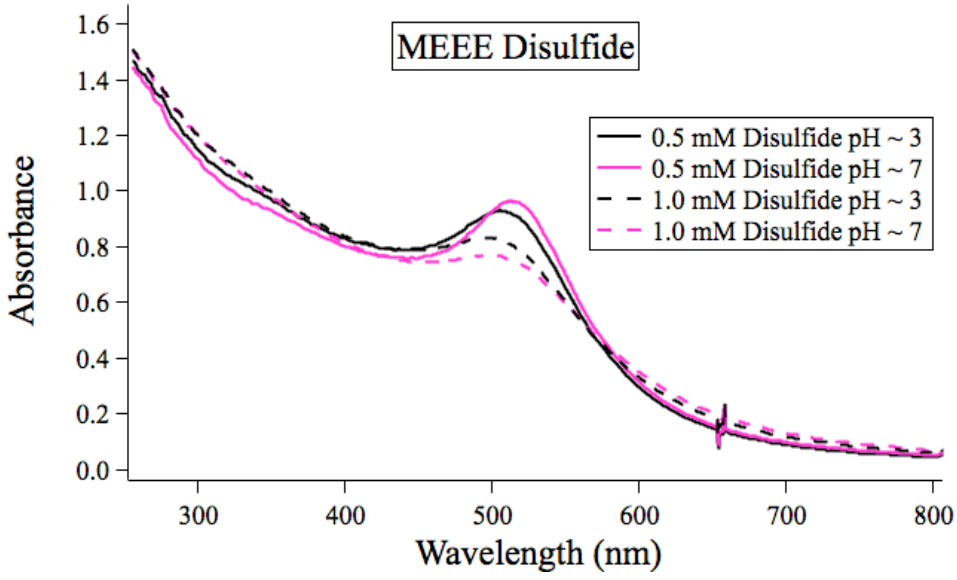

Figure S35. UV/vis spectra for AuNPs synthesized with MEEE disulfide at Au(III) pH ~ 3 and 7. Minimal differences in plasmon lambda max correlate well to similar observed AuNP sizes determined by SAXS.

Comparison of Batch and Microfluidic Syntheses

UV/visible Spectra for AuNPs across Au(III) pH range

UV/vis spectra were collected for each batch of AuNPs produced to determine stability and qualitative size distributions.

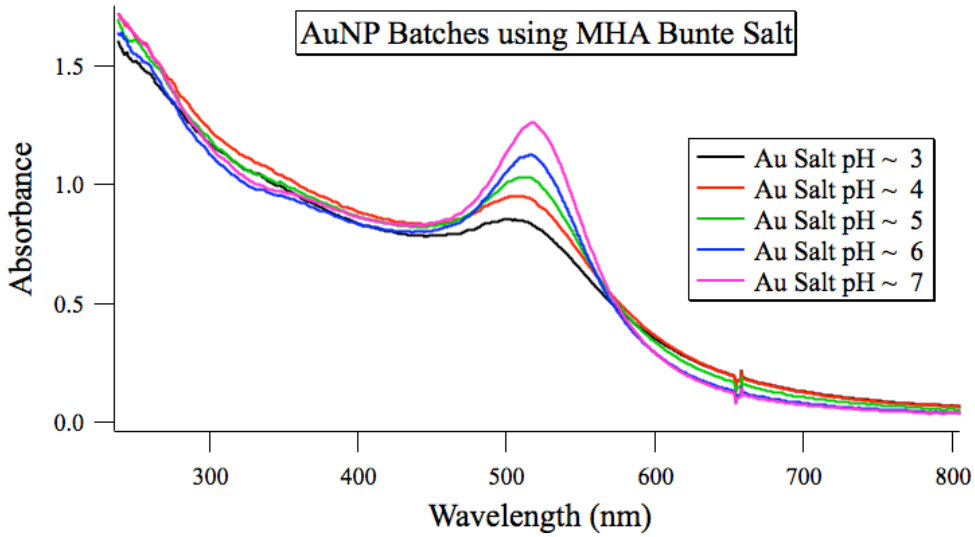

Figure S36. Selected UV/visible spectra for AuNPs synthesized in 80 mL batches using MHA Bunte Salt as ligand. A clear size trend, evidenced by increasing wavelength of the plasmon absorbance lambda-max, exists across the pH range, with higher Au(III) solution pH's resulting in larger AuNPs.

SAXS Working Curve for AuNPs made in Batch

SAXS data were collected for AuNPs synthesized in 80 mL batches. For each data point, 3 syntheses were performed where corresponding SAXS size analyses were averaged to determine average diameters and standard deviations.

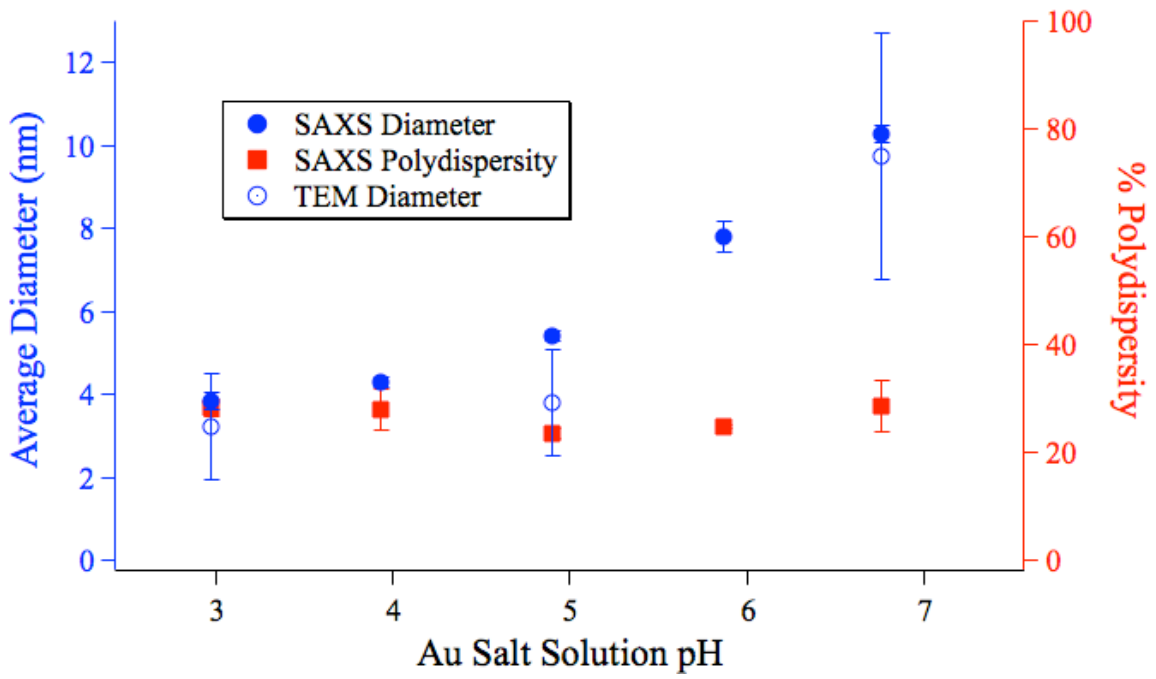

Figure S37. Combined SAXS data for batch AuNP working curve using MHA Bunte salt as ligand. These data correlate well to observed UV/vis trend. Sizes determined by TEM show much larger error bars than analogous SAXS analyses.

Comparison of Variability in AuNP Core Size for Batch and Flow Syntheses

AuNPs were synthesized in (1) batch reactions performed by a single researcher, (2) batch reactions performed by 3 different researchers, and (3) microfluidic reactions by multiple researchers. AuNP size distributions were determined by SAXS. Variability in core size is low when a single researcher performs batch syntheses in rapid succession, but rises dramatically when multiple researchers perform these batch syntheses. When syntheses are performed in a microreactor and the same stock solutions are utilized, researcher-dependent variables are eliminated and variability is much lower than for

reactions performed in batch. Microfluidic reactions performed by single or multiple researchers yield consistent results between syntheses.

Table S4. Summary of AuNP core sizes for 9 different AuNP syntheses, using he MHA ligand, as determined by SAXS

Synthetic Method	SAXS AuNP Diameter (nm)	Diameter Standard Deviation
Single Researcher Batch Syntheses	A) 7.77 B) 7.45 C) 8.22	5%
Multiple Researcher Batch Syntheses	A) 7.87 B) 5.71 C) 8.17	18%
Microfluidic Syntheses	A) 5.73 B) 5.88 C) 5.92	2%

APPENDIX C

SUPPORTING INFORMATION FOR CHAPTER V

Additional Characterization Data

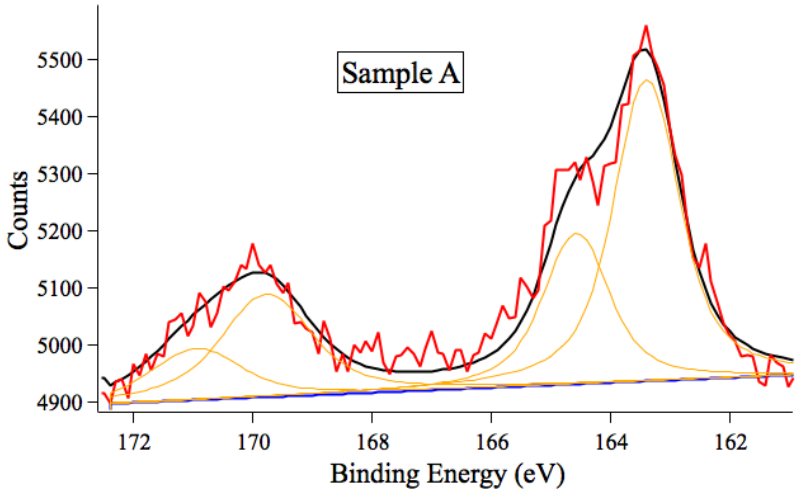

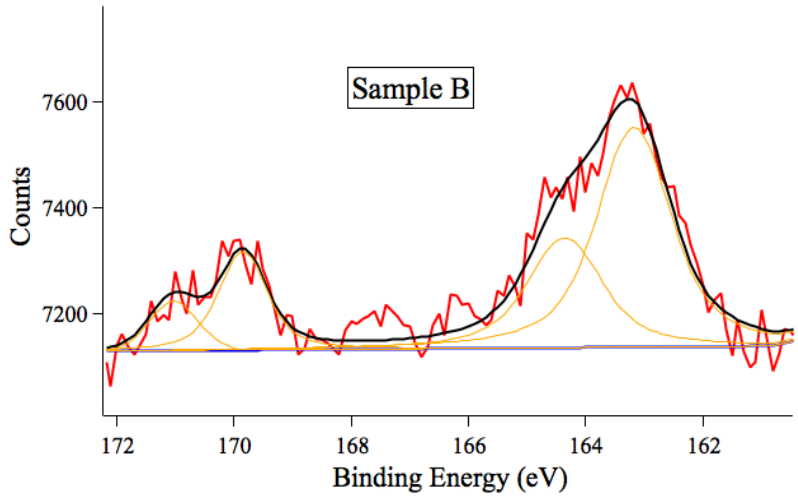

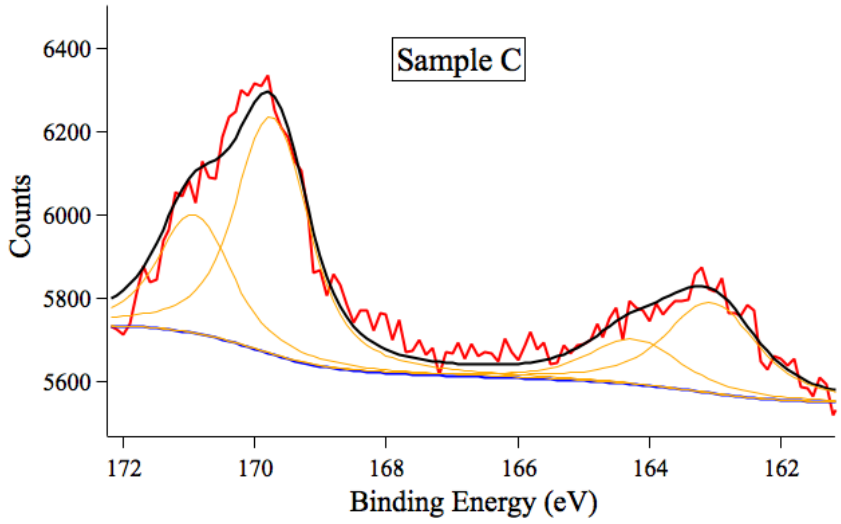

Figure S1. XPS spectra in S 2p region for pure reference materials A, B, and C. Red traces correspond to the raw data, blue traces correspond to fitted background, yellow traces correspond to individual peak fits, and black traces correspond to the overall fit to the data. A set of reduced and a set of oxidized sulfur peaks are observed in each sample. The reduced sulfur peaks (~ 163 eV) represent thiolate bonds to the AuNP surface, while the oxidized peaks (~ 169 eV) represent thiosulfate groups (Bunte salts) that are strongly associated with the Au surface. The percentage of the ligand shell that is composed of reduced sulfur is 69.3% for Sample A, 78.0% for Sample B, and 33.4% for Sample C. While the ratio of oxidized to reduced sulfur varies across these samples, each spectrum is typical of Bunte salt stabilized AuNPs, and each exhibits long-term stability in solution, suggesting strong passivation.

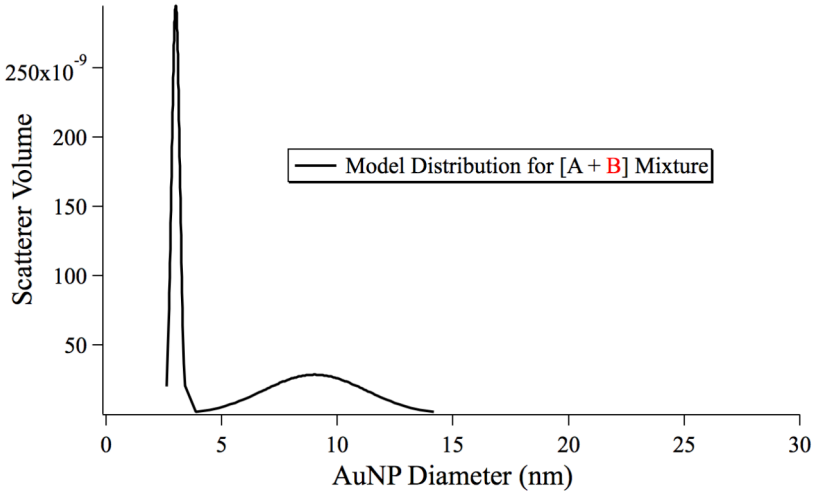
250x10-9
200
150
100
50
Scatterer Volume
Model Distribution for [A + B] Mixture
0
5
10
15
20
25
30
AuNP Diameter (nm)

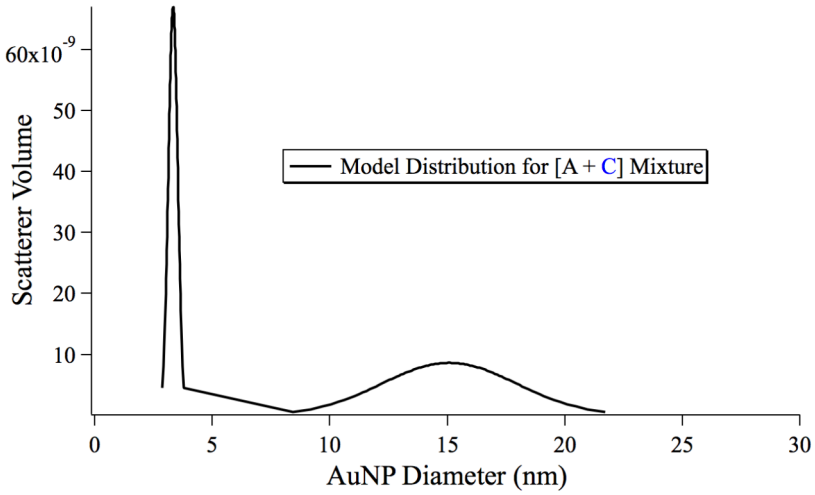
60x10-9
50
40
30
20
10
Scatterer Volume
Model Distribution for [A + C] Mixture
0
5
10
15
20
25
30
AuNP Diameter (nm)

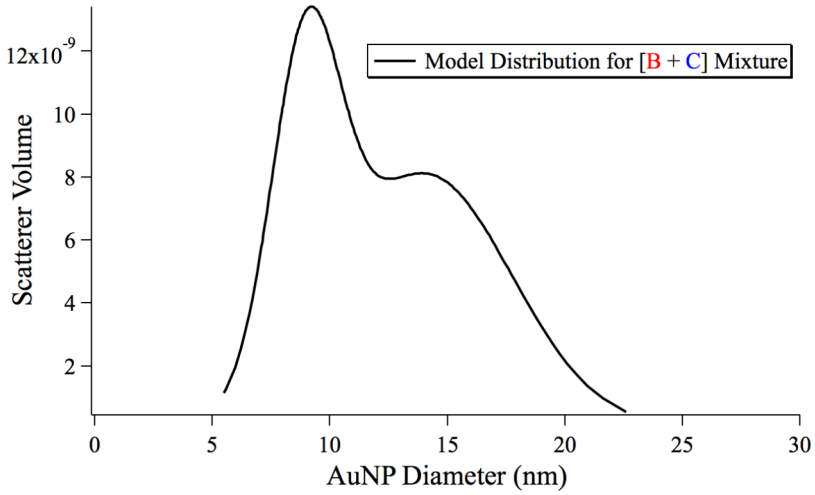
12x10-9
10
8
6
4
2
Scatterer Volume
Model Distribution for [B + C] Mixture
0
5
10
15
20
25
30
AuNP Diameter (nm)

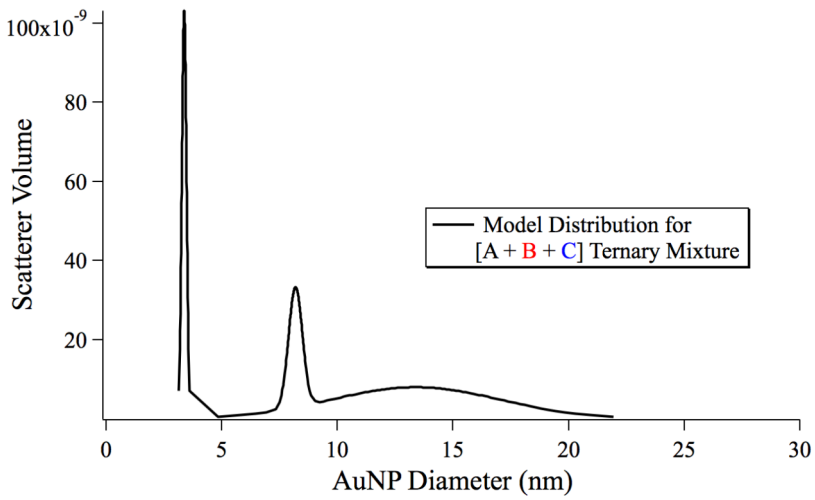

Figure S2. Modeled distributions output for SAXS analysis of binary mixtures [A+B] (S2a), [A+C] (S2b), [B+C] (S2c), and ternary mixture [A+B+C] (S2d). Each individual mode is clearly identified for these mixed samples.

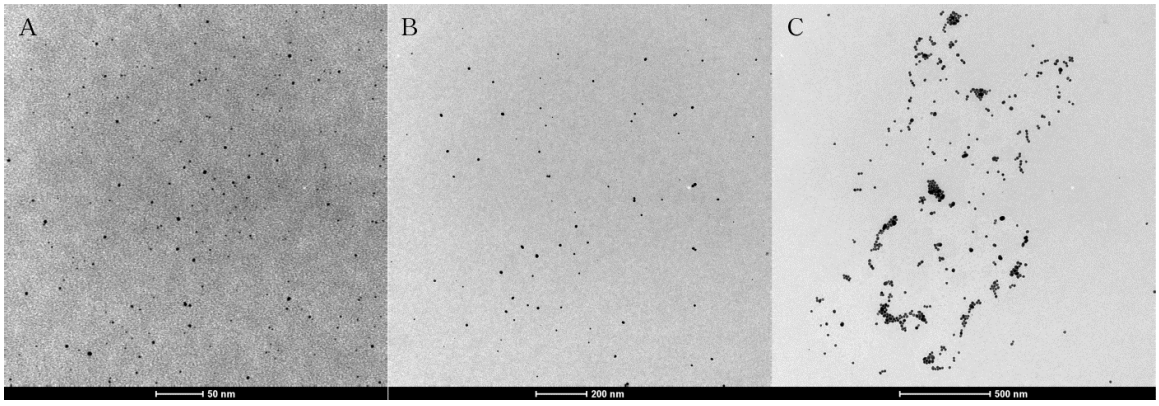

Figure S3. TEM micrographs for reference samples A, B, and C. Sample A shows good dispersion of AuNPs, while Sample B shows several dimers and trimers upon deposition, and Sample C shows significant rafting of particles.

REFERENCES CITED

Chapter I

(1) Aiken, J. D.; Finke, R. G. *J. Mol. Catal. A: Chem.* **1999,** *145*, 1-44.

(2) Alivisatos, A. P. *Science* **1996**, *271*, 933-937.

(3) Brust, M.; Kiely, C. J. *Colloids Surf., A* **2002**, *202*, 175-186.

(4) Dahl, J. A.; Maddux, B. L. S.; Hutchison, J. E. *Chem. Rev.* **2007**, 2228-2269.

(5) Daniel, M.-C.; Astruc, D. *Chem. Rev.* **2004**, *104*, 293-346.

(6) Freestone, I.; Meeks, N.; Sax, M.; Higgitt, C. *Gold Bull.* **2007**, *40*, 270-277.

(7) Shen, G. X.; Chen, Y. C.; Lin, L.; Lin, C. J.; Scantlebury, D. *Electrochim. Acta* **2005**, *50*, 5083-5089.

(8) Fouad, O. A.; Hassan, A. M.; El-Wahab, H. A.; Eldin, A. M.; Naser, A.-R. M.; Wahba, O. A. G. *J. Alloys Compd.* **2012**, *537*, 165-170.

(9) Chen, M.; Goodman, D. W. *Acc. Chem. Res.* **2006**, *39*, 739-46.

(10) Prati, L.; Rossi, M. *J. Catal.* **1998**, *176*, 552-560.

(11) Huang, D.; Liao, F.; Molesa, S.; Redinger, D.; Subramanian, V. *J. Electrochem. Soc.* **2003**, *150*, G412-G412.

(12) Cheng, Z.; Zaki, A. A.; Hui, J. Z.; Muzykantov, V. R.; Tsourkas, A. *Science* **2012**, *338*, 903-910.

(13) Lohse, S. E.; Murphy, C. J. *J. Am. Chem. Soc.* **2012**, *134*, 15607-20.

(14) Gupta, S. M.; Tripathi, M. *Cent. Eur. J. Chem.* **2012**, *10*, 279-294.

(15) Grainger, B. D. W.; Castner, D. G. *Adv. Mater.* **2008**, *20*, 867-877.

(16) Bhattacharyya, S.; Kudgus, R. a.; Bhattacharya, R.; Mukherjee, P. *Pharm. Res.* **2011**, *28*, 237-59.

(17) Woehrle, G. H.; Warner, M. G.; Hutchison, J. E. *J. Phys. Chem. B* **2002**, 9979-9981.

(18) Oh, E.; Delehanty, J. B.; Sapsford, K. E.; Susumu, K.; Goswami, R.; Blanco-Canosa, J. B.; Dawson, P. E.; Granek, J.; Shoff, M.; Zhang, Q.; Goering, P. L.; Huston, A.; Medintz, I. L. *ACS Nano* **2011**, *5*, 6434-6448.

(19) Wang, D.; Nap, R. J.; Lagzi, I.; Kowalczyk, B.; Han, S.; Grzybowski, B. A.; Szleifer, I. *J. Am. Chem. Soc.* **2011**, *133*, 2192-2197.

(20) Montenegro, M.; Amin, F.; Soenen, S. J.; Manshian, B.; Thiron, T.; Cornelissen, M.; Vanhaecke, F.; Doak, S.; Parak, W. J.; Smedt, S. D.; Braeckmans, K. *ACS Nano* **2012**, *6*, 5767-5783.

(21) Sardar, R.; Funston, A. M.; Mulvaney, P.; Murray, R. W. *Langmuir* **2009**, *25*, 13840-13851.

(22) Hodes, G. *Adv. Mater.* **2007**, *19*, 639-655.

(23) Thelander, C.; Magnusson, M. H.; Deppert, K.; Samuelson, L.; Poulsen, P. R.; NygaÃärd, J.; Borggreen, J. R. *Appl. Phys. Lett.* **2001**, *79*, 2106-2106.

(24) Haruta, M. *Gold Bull.* **2004**, 27-36.

(25) Ghosh, A.; Basak, S.; Wunsch, B. H.; Kumar, R.; Stellacci, F. *Angew. Chem., Int. Ed. Eng.* **2011**, *50*, 7900-5.

(26) Chen, M. S.; Goodman, D. W. *Science* **2004**, *306*, 252-255.

(27) Banerjee, P.; Conklin, D.; Nanayakkara, S.; Park, T.-H.; Therien, M. J.; Bonnell, D. A. *ACS Nano* **2010**, *4*, 1019-1025.

(28) Bukasov, R.; Ali, T. a.; Nordlander, P.; Shumaker-Parry, J. S. *ACS Nano* **2010**, *4*, 6639-50.

(29) Lee, K.-S.; El-Sayed, M. a. *J. Phys. Chem. B* **2006**, *110*, 19220-5.

(30) Lisowski, C. E.; Hutchison, J. E. *Anal. Chem.* **2009**, *81*, 10246-53.

(31) Upadhyayula, V. K. K. *Anal. Chim. Acta* **2012**, *715*, 1-18.

(32) Huang, Y.-F.; Sefah, K.; Bamrungsap, S.; Chang, H.-T.; Tan, W. *Langmuir* **2008**, 11860-11865.

(33) Murphy, C. J. *J. Mater. Chem.* **2008**, *18*, 2173-2173.

(34) Woehrle, G. H.; Hutchison, J. E. *Inorg. Chem.* **2005**, *44*, 6149-6158.

(35) Hill, H. D.; Millstone, J. E.; Banholzer, M. J.; Mirkin, C. A. *ACS Nano* **2009**, *3*, 418-424.

(36) Turkevich, J.; Stevenson, P. C.; Hillier, J. *Faraday Discuss.* **1951**, 55-75.

(37) Turkevich, J.; Stevenson, P. C.; Hillier, J. *J. Phys. Chem.* **1954**, *57*, 670-673.

(38) Frens, G. *Nature* **1973**, *241*, 20-22.

(39) Ojea-Jimenez, I.; Puntes, V. *J. Am. Chem. Soc.* **2009**, *131*, 13320-7.

(40) Bastus, N. G.; Comenge, J.; Puntes, V. *Langmuir* **2011**, *27*, 11098-11105.

(41) Polte, J. r.; Ahner, T. T.; Delissen, F.; Sokolov, S.; Emmerling, F.; Thuenemann, A. F.; Kraehnert, R. *J. Am. Chem. Soc.* **2010**, *132*, 1296-301.

(42) Kumar, S.; Gandhi, K. S.; Kumar, R. *Ind. Eng. Chem. Res.* **2007**, *46*, 3128-3136.

(43) Njoki, P. N.; Luo, J.; Kamundi, M. M.; Lim, S.; Zhong, C.-J. *Langmuir* **2010**, *57*, 13622-13629.

(44) Kimling, J.; Maier, M.; Okenve, B.; Kotaidis, V.; Ballot, H.; Plech, A. *J. Phys. Chem. B* **2006**, 15700-15707.

(45) Pong, B.-K.; Elim, H. I.; Chong, J.-X.; Ji, W.; Trout, B. L.; Lee, J.-Y. *J. Phys. Chem. C* **2007**, *111*, 6281-6287.

(46) Ji, X.; Song, X.; Li, J.; Bai, Y.; Yang, W.; Peng, X. *J. Am. Chem. Soc.* **2007**, *129*, 13939-48.

(47) Lohse, S. E.; Dahl, J. a.; Hutchison, J. E. *Langmuir* **2010**, *26*, 7504-11.

(48) Brust, M.; Walker, M.; Bethell, D.; Schiffrin, D. J.; Whyman, R. *J. Chem. Soc., Chem. Commun.* **1994**, 801-802.

(49) Hostetler, M. J.; Wingate, J. E.; Zhong, C.-J.; Harris, J. E.; Vachet, R. W.; Clark, M. R.; Londono, J. D.; Green, S. J.; Stokes, J. J.; Wignall, G. D.; Glish, G. L.; Porter, M. D.; Evans, N. D.; Murray, R. W. *Langmuir* **1998**, *14*, 17-30.

(50) Schaaff, T. G.; Shafigullin, M. N.; Khoury, J. T.; Vezmar, I.; Whetten, R. L.; Cullen, W. G.; First, P. N.; Gutierrez-Wing, C.; Ascensio, J.; Jose-Yacaman, M. J. *J. Phys. Chem. B* **1997**, *101*, 7885.

(51) Xia, M.; Huang, R.; Witt, K. L.; Southall, N.; Fostel, J.; Cho, M.-H.; Jadhav, A.; Smith, C. S.; Inglese, J.; Portier, C. J.; Tice, R. R.; Austin, C. P. *Environ. Health Perspect.* **2008**, *116*, 284-291.

(52) Brust, M.; Fink, J.; Schiffrin, D. J.; Kiely, C. *J. Chem. Soc., Chem. Commun.* **1995**, 1655-1656.

(53) Love, J. C.; Estroff, L. A.; Kriebel, J. K.; Nuzzo, R. G.; Whitesides, G. M. *Chem. Rev.* **2005**, *105*, 1103-1169.

(54) Templeton, A. C.; Wuelfing, W. P.; Murray, R. W. *Acc. Chem. Res.* **2000**, *33*, 27-36.

(55) Brinas, R. P.; Hu, M.; Qian, L.; Lymar, E. S.; Hainfeld, J. F. *J. Am. Chem. Soc.* **2008**, *130*, 975-82.

(56) Shon, Y.-S.; Gross, S. M.; Dawson, B.; Porter, M.; Murray, R. W. *Langmuir* **2000**, *16*, 6555-6561.

(57) Shon, Y.-S.; Wuelfing, W. P.; Murray, R. W. *Langmuir* **2001**, 1255-1261.

(58) Chan, E. M.; Alivisatos, A. P.; Mathies, R. A. *J. Am. Chem. Soc.* **2005**, *127*, 13854-61.

(59) Chan, E. M.; Mathies, R. a.; Alivisatos, A. P. *Nano Lett.* **2003**, *3*, 199-201.

(60) Yen, B. K. H.; Stott, N. E.; Jensen, K. F.; Bawendi, M. G. *Adv. Mater.* **2003**, *15*, 1858-1862.

(61) Fletcher, N. H. *J. Chem. Phys.* **1958**, *29*, 572-576.

(62) Sugimoto, T. *Adv. Coll. Inter. Sci.* **1987**, *28*, 65-108.

(63) Jose-Yacaman, M. J.; Gutierrez-Wing, C.; Miki, M.; Yang, D.-Q.; Piyakis, K. N.; Sacher, E. *J. Phys. Chem. B* **2005**, *109*, 9703-9711.

(64) Kukushkin, S. A.; Slyozov, V. V. *J. Phys. Chem. Solids* **1996**, *57*, 195-204.

(65) Clark, M. D.; Kumar, S. K.; Owen, J. S.; Chan, E. M. *Nano Lett.* **2011**, *11*, 1976-80.

(66) Woehrle, G. H.; Brown, L. O.; Hutchison, J. E. *J. Am. Chem. Soc.* **2005**, *127*, 2172-2183.

(67) Shipway, A. N.; Lahav, M.; Gabai, R.; Willner, I. *Langmuir* **2000**, *16*, 8789-8795.

(68) Maillard, F.; Schreier, S.; Hanzlik, M.; Savinova, E. R.; Weinkauf, S.; Stimming, U. *Phys. Chem. Chem. Phys.* **2005**, *7*, 385-393.

(69) Dinegar, H.; LaMer, V. *J. Am. Chem Soc.* **1950**, *72*.

(70) Schmidbaur, H. *Gold Bull.* **2000**, *33*, 3-10.

(71) Schmidbaur, H.; Cronje, S.; Djordjevic, B.; Schuster, O. *Chem. Phys.* **2005**, *311*, 151-161.

(72) Abecassis, B.; Testard, F.; Spalla, O.; Barboux, P. *Nano Lett.* **2007**, *7*, 1723-1727.

(73) Polte, J.; Erler, R.; Thu, A. F.; Sokolov, S.; Ahner, T. T.; Rademann, K.; Emmerling, F.; Kraehnert, R. *ACS Nano* **2010**, *4*, 1076-1082.

(74) Skrdla, P. J. *J. Phys. Chem. C* **2012**, *116*, 214-225.

(75) Wagner, C. *Elecktrochem* **1961**, *65*, 581-591.

(76) Avrami, M. *J. Chem. Phys.* **1939**, *7*, 1103-1112.

(77) Avrami, M. *J. Chem. Phys.* **1940**, *8*, 212-224.

(78) Avrami, M. *J. Chem. Phys.* **1941**, *9*, 177-184.

(79) Finney, E. E.; Finke, R. G. *Chem. Mater.* **2009**, *21*, 4692-4705.

(80) Finney, E. E.; Finke, R. G. *Chem. Mater.* **2008**, 1956-1970.

(81) Shields, S. P.; Richards, V. N.; Buhro, W. E. *Chem. Mater.* **2010**, *22*, 3212-3225.

(82) Skrdla, P. J.; Robertson, R. T. *Chem. Mater.* **2008**, *20*, 3-4.

(83) Finney, E. E.; Finke, R. G. *Chem. Mater.* **2010**, *22*, 2687-2688.

(84) Hutchison, J. E. *ACS Nano* **2008**, *2*, 395-402.

(85) Kim, Y.; Chung, B. L.; Ma, M.; Mulder, W. J. M.; Fayad, Z. A.; Farokhzad, O. C.; Langer, R. *Nano Lett.* **2012**, *12*, 3587-3591.

(86) Park, J. I.; Saffari, A.; Kumar, S.; Gunther, A.; Kumacheva, E. *Annu. Rev. Mater. Res.* **2010**, *40*, 415-443.

(87) Song, Y.; Hormes, J.; Kumar, C. S. S. R. *Small* **2008**, 698-711.

(88) Marmiroli, B.; Grenci, G.; Cacho-Nerin, F.; Sartori, B.; Ferrari, E.; Laggner, P.; Businaro, L.; Amenitsch, H. *Lab Chip* **2009**, 2063-2069.

(89) Edel, J. B.; Fortt, R.; DeMello, J. C.; DeMello, A. J. *Chem. Commun.* **2002**, 1136-1137.

(90) Cabeza, V. S.; Kuhn, S.; Kulkarni, A. a.; Jensen, K. F. *Langmuir* **2012**, *28*, 7007-13.

(91) Paclawski, K.; Streszewski, B. C.; Jaworski, W.; Luty-Blocho, M.; Fitzner, K. *Colloids Surf., A* **2012**, *413*, 208-215.

(92) DeMello, A. J. *Nature* **2006**, *442*, 394-402.

(93) Zhao, C.-X.; He, L.; Qiao, S. Z.; Middelberg, A. P. J. *Chem. Eng. Sci.* **2011**, *66*, 1463-1479.

(94) DeMello, J. C.; DeMello, A. J. *Lab Chip* **2004**, 11-15.

(95) Chan, E. M.; Marcus, M. A.; Fakra, S.; Elnaggar, M.; Mathies, R. A.; Alivisatos, A. P. *J. Phys. Chem. A* **2007**, 12210-12215.

(96) Haben, P. M.; McKenzie, L. C.; Kevan, S. D.; Hutchison, J. E. *J. Phys. Chem. C* **2010**, *114*, 22055-22063.

(97) Biswas, K.; Varghese, N.; Rao, C. N. R. *Small* **2008**, 649-655.

(98) Koerner, H.; Maccuspie, R. I.; Park, K.; Vaia, R. A. *Chem. Mater.* **2011**, *24*, 981-995.

(99) Richman, E. K.; Hutchison, J. E. *ACS Nano* **2009**, *3*, 2441-2446.

(100) Oosthoek, J. L. M.; Kooi, B. J.; De Hosson, J. T. M.; Wolters, R. A. M.; Gravesteijn, D. J.; Attenborough, K. *Microsc. Microanal.* **2010**, *16*, 291-299.

(101) White, R. G.; Nunney, T. S.; Strohmeier, B. R.; Piasecki, J. D.; Lee, R. J. *Microsc. Microanal.* **2010**, *16*, 436-437.

(102) Skoog, A. S.; Holler, F. J.; Nieman, T. A. *Principles of Instrumental Analysis 5th ed.*; Saunders Publishing, USA, 1998.

(103) Kearns, G. J.; Foster, E. W.; Hutchison, J. E. *Anal. Chem.* **2006**, *78*, 298-303.

(104) Ross, F. M. *Microsc. Microanal.* **2010**, *16*, 326-237.

(105) Bienert, R.; Emmerling, F.; Thuenemann, A. F. *Anal. Bioanal. Chem.* **2009**, *395*, 1651-1660.

(106) Larson-Smith, K.; Jackson, A.; Pozzo, D. C. *Langmuir* **2012**, *28*, 2493-2501.

(107) Glatter, O.; Kratky, O. *Small Angle X-ray Scattering*, 1982.

(108) Njoki, P. N.; Lim, I. S.; Mott, D.; Park, H.-Y.; Khan, B.; Mishra, S.; Sujakumar, R.; Luo, J.; Zhong, C.-J. *J. Phys. Chem. C* **2007**, *111*, 14664-14669.

(109) Haiss, W.; Thanh, N. T. K.; Aveyard, J.; Fernig, D. G. *Anal. Chem.* **2007**, *79*, 4215-4221.

(110) Liu, X.; Atwater, M.; Wang, J.; Huo, Q. *Colloids Surf.* **2007**, *58*, 3-7.

Chapter II

(1) Billinge, S. J. L.; Levin, I. *Science* **2007**, *316*, 561-565.

(2) Daniel, M. C.; Astruc, D. *Chem. Rev.* **2004**, *104*, 293-346.

(3) Richman, E. K.; Hutchison, J. E. *ACS Nano* **2009**, *3*, 2441-2446.

(4) Woehrle, G. H.; Hutchison, J. E.; Ozkar, S.; Finke, R. G. *Turk. J. Chem.* **2006**, *30*, 1-13.

(5) Borchert, H.; Shevehenko, E. V.; Robert, A.; Mekis, I.; Kornowski, A.; Grubel, G.; Weller, H. *Langmuir* **2005**, *21*, 1931-1936.

(6) Beaucage, G.; Kammler, H. K.; Pratsinis, S. E. *J. Appl. Crystallogr.* **2004**, *37*, 523-535.

(7) Baum, M. NIST Reference Materials Are 'Gold Standard' for Bio-Nanotech Research. http://www.nist.gov/mml/ceramics/gold-standard.cfm (Accessed November, 2010)

(8) Bhargava, S. K.; Booth, J. M.; Agrawal, S.; Coloe, P.; Kar, G. *Langmuir* **2005**, *21*, 5949-5956.

(9) Abecassis, B.; Testard, F.; Spalla, O.; Barboux, P. *Nano Lett.* **2007**, *7*, 1723-1727.

(10) Briois, V.; Giorgetti, C.; Dartyge, E.; Baudelet, F.; Tokumoto, M. S.; Pulcinelli, S. H.; Santilli, C. V. *J. Sol-Gel Sci. Technol.* **2006**, *39*, 25-36.

(11) Harada, M.; Kuramitsu, K.; Kimura, Y.; Saijo, K. *Colloids Surf., A* **2008**, *327*, 21-33.

(12) Angermund, K.; Buhl, M.; Endruschat, U.; Mausechick, T.; Mortel, R.; Mynott, R.; Tesche, B.; Waldofner, N.; Bonnemann, H.; Kohl, G.; Modrow, H.; Hormes, J.; Dinjus, E.; Gassner, F.; Haubold, H.-G.; Vad, T.; Kaupp, M. *J. Phys. Chem. B* **2003**, *107*, 7507-7515.

(13) Bienert, R.; Emmerling, F.; Thunemann, A. F. *Anal. Bioanal. Chem.* **2009**, *395*, 1651-1660.

(14) Bolze, J.; Pontoni, D.; Ballauff, M.; Narayanan, T.; Colfen, H. *J. Colloid Inter. Sci.* **2004**, *277*, 84-94.

(15) Schmolzer, S.; Grabner, D.; Gradzielski, M.; Narayanan, T. *Phys. Rev. Lett.* **2002**, *88*, 2583011-2583014.

(16) Cagiao, M. E.; Pozdnyakov, A. O.; Krumova, M.; Kudryavtsev, V. V.; Calleja, F. J. B. *Compos. Sci. Technol.* **2007**, *67*, 2175-2182.

(17) Martel, A.; Burghammer, M.; Davies, R. J.; Di Cola, E.; Vendrely, C.; Reikel, C. *J. Am. Chem. Soc.* **2008**, *ASAP*.

(18) Boissiere, C.; Grosso, D.; Amenitsch, H.; Gibaud, A.; Coupe, A.; Baccile, N.; Sanchez, C. *Chem. Commun.* **2003**, 2798-2799.

(19) Biswas, K.; Varghese, N.; Rao, C. N. R. *Small* **2008**, *4*, 649-655.

(20) Sakamoto, N.; Harada, M.; Hashimoto, T. *Macromolecules* **2006**, *39*, 1116-1124.

(21) Rothe, J.; Hormes, J.; Bonnemann, H.; Brijoux, W.; Siepen, K. *J. Am. Chem. Soc.* **1998**, *120*, 6019-6023.

(22) Mesu, J. G.; Beale, A. M.; de Groot, F. M. F.; Weckhuysen, B. M. *J. Phys. Chem. B* **2006**, *110*, 17671-17677.

(23) Zinoveva, S.; De Silva, R.; Louis, R. D.; Datta, P.; Kumar, C.; Goettert, J.; Hormes, J. *Nucl. Instrum. Methods Phys. Res., Sect. A* **2007**, *582*, 239-241.

(24) Wang, W.; Zhang, K.; Cai, Q.; Mo, G.; Xing, X. Q.; Cheng, W. D.; Chen, Z. J.; Wu, Z. H. *Eur. Phys. J. B* **2010**, *76*, 301-307.

(25) Jayanetti, S.; Mayanovic, R. A.; Anderson, A. J.; Bassett, W. A. *J. Chem. Phys.* **2001**, *115*, 954-962.

(26) Polte, J.; Erler, R.; Thunemann, A. F.; Sokolov, S.; Ahner, T. T.; Rademann, K.; Emmerling, F.; Kraehnert, R. *ACS Nano* **2010**, *4*, 1076-1082.

(27) Woehrle, G. H.; Warner, M. G.; Hutchison, J. E. *Langmuir* **2004**, *20*, 5982-5988.

(28) Woehrle, G. H.; Brown, L. O.; Hutchison, J. E. *J. Am. Chem. Soc.* **2005**, *127*, 2172-2183.

(29) Vollenbroek, F. A.; Bosman, W. P.; Bour, J. J.; Noordik, J. H.; Beurskens, P. T. *J. Chem. Soc., Chem. Commun.* **1979**, 387.

(30) Manassero, M.; Naldini, L.; Sansoni, M. *J. Chem. Soc., Chem. Commun.* **1979**, 385.

(31) Hall, K. P.; Mingos, D. M. P. *Prog. Inorg. Chem.* **1984**, *32*, 237-325.

(32) Weare, W. W.; Reed, S. M.; Warner, M. G.; Hutchison, J. E. *J. Am. Chem. Soc.* **2000**, *122*, 12890-12891.

(33) Kanaras, A. G.; Kamounah, F. S.; Schaumburg, K.; Kiely, C. J.; Brust, M. *J. Chem. Soc., Chem. Commun.* **2002**, 2294-2295.

(34) Sweeney, S. F.; Woehrle, G. H.; Hutchison, J. E. *J. Am. Chem. Soc.* **2006**, *128*, 3190-3197.

(35) Nagao, O.; Harada, G.; Sugawara, T.; Sasaki, A.; Ito, Y. *Jpn. J. Appl. Phys.* **2004**, *43*, 7742-7746.

(36) Ilavsky, J. "Nika" package of 2D -> 1D SAS data reduction macros for Igor Pro. http://usaxs.xor.aps.anl.gov/staff/ilavsky/nika.html (Accessed November, 2007)

(37) Ilavsky, J.; Jemian, P. R. *J. Appl. Crystallogr.* **2009**, *42*, 347-353.

(38) Dahl, J. A.; Maddux, B. L. S.; Hutchison, J. E. *Chem. Rev.* **2007**, *107*, 2228-2269.

(39) Hall, K. P.; Mingos, D. M. P. *Prog. Inorg. Chem.* **1984**, 237-325.

(40) Murray, C. B.; Kagan, C. R.; Bawendi, M. G. *Annu. Rev. Mater. Sci.* **2000**, *30*, 545-610.

(41) Woehrle, G. H.; Warner, M. G.; Hutchison, J. E. *J. Phys. Chem. B* **2002**, *106*, 9979-9981.

(42) Brust, M.; Walker, M.; Bethell, D.; Schiffrin, D. J.; Whyman, R. *J. Chem. Soc., Chem. Commun.* **1994**, 801-802.

(43) Bartlett, P. A.; Bauer, B.; Singer, S. J. *J. Am. Chem. Soc.* **1978**, *100*, 5085-5089.

(44) Wilcoxon, J. P.; Martin, J. E.; Provencio, P. *J. Chem. Phys.* **2001**, *115*, 998-1008.

(45) Burda, C.; Chen, X. B.; Narayanan, R.; El-Sayed, M. A. *Chem. Rev.* **2005**, *105*, 1025-1102.

(46) Plech, A.; Kotaidis, V.; Siems, A.; Sztucki, M. *Phys. Chem. Chem. Phys.* **2008**, *10*, 3888-3894.

Chapter III

(1) Sardar, R.; Schumaker-Parry, J. S. *J. Am. Chem. Soc.* **2011**, *133*, 8179-8190.

(2) Dahl, J. A.; Maddux, B. L. S.; Hutchison, J. E. *Chem. Rev.* **2007**, *107*, 2228-2269.

(3) Wang, D.; Nap, R. J.; Lagzi, I.; Kowalcyzk, B.; Han, S.; Grzybowski, B. A.; Szleifer, I. *J. Am. Chem. Soc.* **2011**, *133*, 2192-2197.

(4) Daniel, M.-C.; Astruc, D. *Chem. Rev.* **2004**, *104*, 293-346.

(5) Kemp, M. M.; Kumar, A.; Mousa, S.; Park, T.; Ajayan, P.; Kubotera, N.; Mousa, S. A.; Linhardt, R. J. *Biomacromolecules* **2009**, *10*, 589-595.

(6) Simpson, C. A.; Agrawal, A. C.; Balinski, A.; Harkness, K. M.; Cliffel, D. E. *ACS Nano* **2011**, *5*, 3577-3584.

(7) Popovtzer, R.; Agrawal, A.; Kotov, N. A.; Popovtzer, A.; Balter, J.; Carey, T. E.; Kopelman, R. *Nano letters* **2008**, *8*, 4593-4596.

(8) Sun, I.-C.; Eun, D.-K.; Na, J. H.; Lee, S.; Kim, I.-J.; Youn, I.-C.; Ko, C.-Y.; Kim, H.-S.; Lim, D.; Choi, K.; Messersmith, P. B.; Park, T. G.; Kim, S. Y.; Kwon, I. C.; Kim, K.; Ahn, C.-H. *Chem. Eur. J.* **2009**, *15*, 13341-13347.

(9) Jain, S.; Hirst, D. G.; O'Sullivan, J. M. *Brit. J. Radiol.* **2012**, *85*, 101-13.

(10) Unak, G.; Ozkaya, F.; Medine, E. I.; Kozgus, O.; Sakarya, S.; Bekis, R.; Unak, P.; Timur, S. *Colloids Surf., B* **2012**, *90*, 217-26.

(11) Lohse, S. E.; Murphy, C. J. *J. Am. Chem. Soc.* **2012**, *134*, 15607-15620.

(12) Kang, B.; Mackey, M. A.; El-Sayed, M. A. *J. Am. Chem. Soc.* **2010**, *132*, 1517-1519.

(13) Oh, E.; Delehanty, J. B.; Sapsford, K. E.; Susumu, K.; Goswami, R.; Blanco-canosa, J. B.; Dawson, P. E.; Granek, J.; Shoff, M.; Zhang, Q.; Goering, P. L.; Huston, A.; Medintz, I. L. *ACS Nano* **2011**, *5*, 6434-6448.

(14) Chen, A. H.; Silver, P. A. *Trends Cell Biol.* **2012**, *22*, 662-670.

(15) Brown, L. O.; Hutchison, J. E. *J. Am. Chem. Soc.* **1999**, *121*, 882-883.

(16) Woehrle, G. H.; Hutchison, J. E. *Inorg. Chem.* **2005**, *44*, 6149-6158.

(17) Hong, R.; Fernandez, J. M.; Nakade, H.; Arvizo, R.; Emrick, T.; Rotello, V. M. *Chem. Commun.* **2006**, 2347-2349.

(18) Brust, M.; Walker, M.; Bethell, D.; Schiffrin, D. J.; Whyman, R. *J. Chem. Soc., Chem. Commun.* **1994**, 801-802.

(19) Hill, H. D.; Millstone, J. E.; Banholzer, M. J.; Mirkin, C. A. *ACS Nano* **2009**, *3*, 418-424.

(20) Ivanov, M. R.; Bednar, H. R.; Haes, A. J. *ACS Nano* **2009**, *3*, 386-394.

(21) Ojea-Jimenez, I.; Puntes, V. *J. Am. Chem. Soc.* **2009**, *131*, 13320-13327.

(22) Brust, M.; Fink, J.; Schiffrin, D. J.; Kiely, C. *J. Chem. Soc., Chem. Commun.* **1995**, 1655-1656.

(23) Oh, E.; Susumu, K.; Goswami, R.; Mattoussi, H. *Langmuir* **2010**, *26*, 7604-7613.

(24) Hostetler, M. J.; Wingate, J. E.; Zhong, C.-J.; Harris, J. E.; Vachet, R. W.; Clark, M. R.; Londono, J. D.; Green, S. J.; Stokes, J. J.; Wignall, G. D.; Glish, G. L.; Porter, M. D.; Evans, N. D.; Murray, R. W. *Langmuir* **1998**, *14*, 17-30.

(25) Ji, X.; Song, X.; Li, J.; Bai, Y.; Yang, W.; Peng, X. *J. Am. Chem. Soc.* **2007**, *129*, 13939-48.

(26) Wang, S.; Qian, K.; Bi, X.; Huang, W. *J. Phys. Chem. C* **2009**, *113*, 6505-6510.

(27) Lisowski, C. E.; Hutchison, J. E. *Anal. Chem.* **2009**, *81*, 10246-10253.

(28) Lohse, S. E.; Dahl, J. A.; Hutchison, J. E. *Langmuir* **2010**, *26*, 7504-7511.

(29) Shon, Y.-S.; Gross, S. M.; Dawson, B.; Porter, M.; Murray, R. W. *Langmuir* **2000**, *16*, 6555-6561.

(30) Fealy, R. J.; Ackerman, S. R.; Ferguson, G. S. *Langmuir* **2011**, *27*, 5371-5376.

(31) Liu, X.; Atwater, M.; Wang, J.; Huo, Q. *Colloids Surf., B* **2007**, *58*, 3-7.

(32) Koerner, H.; MacCuspie, R. I.; Park, K.; Vaia, R. A. *Chem. Mater.* **2012**, *24*, 981-995.

(33) Haben, P. M.; McKenzie, L. C.; Kevan, S. D.; Hutchison, J. E. *J. Phys. Chem. C* **2010**, *114*, 22055-22063.

(34) Polte, J.; Ahner, T. T.; Delissen, F.; Sokolov, S.; Emmerling, F.; Thunemann, A. F.; Kraehnert, R. *J. Am. Chem. Soc.* **2010**, *132*, 1296-1301.

(35) Richman, E. K.; Hutchison, J. E. *ACS Nano* **2009**, *3*, 2441-2446.

(36) Marre, S.; Jensen, K. F. *Chem. Soc. Rev.* **2010**, *39*, 1183-1203.

(37) Park, J. I.; Saffari, A.; Kumar, S.; Gunther, A.; Kumacheva, E. *Annu. Rev. Mater. Res.* **2010**, *40*, 415-443.

(38) DeMello, A. J. *Nature* **2006**, *442*, 394-402.

(39) Woehrle, G. H.; Brown, L. O.; Hutchison, J. E. *J. Am. Chem. Soc.* **2005**, *127*, 2172-2183.

(40) (a) Reeves, J. H.; Song, S.; Bowden, E. F. *Anal. Chem.* **1993**, *65*, 683-688. (b) Takegawa, Y.; Deguchi, K.; Ito, S.; Yoshioka, S.; Sano, A.; Yoshinari, K.; Kobayashi, K.; Nakagawa, H.; Monde, K.; Nishimura, S. *Anal. Chem.* **2004**, *76*, 7294-7303.

Chapter IV

(1) Dahl, J. A.; Maddux, B. L. S.; Hutchison, J. E. *Chem. Rev.* **2007**, 2228-2269.

(2) Daniel, M.-C.; Astruc, D. *Chem. Rev.* **2004**, *104*, 293-346.

(3) Aiken III, J. D.; Finke, R. G. *J. Mol. Catal. A: Chem. 145* **1999**, *145*, 1-44.

(4) Baffou, G.; Quidant, R.; Garcia, F. J. *ACS Nano* **2010**, *4*, 709-716.

(5) Bhattacharyya, S.; Kudgus, R. A.; Bhattacharya, R.; Mukherjee, P. *Pharm. Res.* **2011**, *28*, 237-59.

(6) Grainger, D. W.; Castner, D. G. *Adv. Mater.* **2008**, *20*, 867-877.

(7) Lohse, S. E.; Murphy, C. J. *J. Am. Chem. Soc.* **2013**, *134*, 15607-20.

(8) Sardar, R.; Funston, A. M.; Mulvaney, P.; Murray, R. W. *Langmuir* **2009**, *25*, 13840-13851.

(9) Haben, P. M.; Elliott III, E. W.; Hutchison, J. E. *Submitted for publication.*

(10) Weare, W. W.; Reed, S. M.; Warner, M. G.; Hutchison, J. E. *J. Am. Chem. Soc.* **2000**, 12890-12891.

(11) Sweeney, S. F.; Woehrle, G. H.; Hutchison, J. E. *J. Am. Chem. Soc.* **2006**, 5220-5227.

(12) Schmid, G.; Pfeil, R.; Boese, R.; BAndermann, F.; Meyer, S.; Calis, G.; van der Velden, H. M. *Chem. Ber.* **1981**, *114*, 3634.

(13) Ji, X.; Song, X.; Li, J.; Bai, Y.; Yang, W.; Peng, X. *J. Am. Chem. Soc.* **2007**, *129*, 13939-48.

(14) Wang, S.; Qian, K.; Bi, X.; Huang, W. *J. Phys. Chem. C* **2009**, 6505-6510.

(15) DeMello, A. J.; Wooton, R. C. R. *Nature* **2010**, *464*, 839-840.

(16) DeMello, J. C.; DeMello, A. J. *Lab Chip* **2004**, 11-15.

(17) Edel, J. B.; Fortt, R.; DeMello, J. C.; DeMello, A. J. *Chem. Commun.* **2002**, 1136-1137.

(18) Fealy, R. J.; Ackerman, S. R.; Ferguson, G. S. *Langmuir* **2011**, *27*, 5371-6.

(19) Lukkari, J.; Meretoja, M.; Kartio, I.; Laajalehto, K.; Lindstrom, M. *Langmuir* **1999**, *15*, 3529-3537.

(20) Cabeza, V. S.; Kuhn, S.; Kulkarni, A. a.; Jensen, K. F. *Langmuir* **2012**, *28*, 7007-13.

(21) Held, M.; Kohler, J. M.; Hubner, U.; Wagner, J. *Chem. Eng. Technol.* **2007**, 347-354.

(22) Abeecassis, B.; Testard, F.; Kong, Q.; Francois, B.; Spalla, O. *Langmuir* **2010**, *26*, 13847-13854.

(23) Marmiroli, B.; Grenci, G.; Cacho-Nerin, F.; Sartori, B.; Ferrari, E.; Laggner, P.; Businaro, L.; Amenitsch, H. *Lab Chip* **2009**, *9*, 2063-2069.

(24) Lohse, S. E.; Dahl, J. a.; Hutchison, J. E. *Langmuir* **2010**, *26*, 7504-11.

(25) Haben, P. M.; McKenzie, L. C.; Kevan, S. D.; Hutchison, J. E. *J. Phys. Chem. C* **2010**, *114*, 22055-22063.

(26) Ilavsky, J.; Jemian, P. R. *Appl. Crystallogr.* **2009**, 347-353.

(27) Glatter, O.; Kratky, O. *Small Angle X-ray Scattering*, 1982.

(28) Nguyen, N.-T. *Micromixers: Fundamentals, Desing, and Fabrication, 2nd ed.*; William Andrew, 2011.

(29) Shon, Y.-S.; Gross, S. M.; Dawson, B.; Porter, M.; Murray, R. W. *Langmuir* **2000**, *16*, 6555-6561.

(30) Koerner, H.; Maccuspie, R. I.; Park, K.; Vaia, R. A. *Chem. Mater.* **2012**, *24*, 981-995.

(31) Woehrle, G. H.; Brown, L. O.; Hutchison, J. E. *J. Am. Chem. Soc.* **2005**, 2172-2183.

Chapter V

(1) Alivisatos, A. P. *Science* **1996**, *271*, 933-937.

(2) Chen, X.; Mao, S. S. *Chem. Rev.* **2007**, *107*, 2891-2959.

(3) Glover, R. D.; Miller, J. M.; Hutchison, J. E. *ACS Nano* **2011**, *5*, 8950-8957.

(4) Banerjee, P.; Conklin, D.; Nanayakkara, S.; Park, T.-H.; Therien, M. J.; Bonnell, D. A. *ACS Nano* **2010**, *4*, 1019-1025.

(5) Hodes, G. *Adv. Mater.* **2007**, *19*, 639-655.

(6) Jain, S.; Hirst, D. G.; O'Sullivan, J. M. *Brit. J. Radiol.* **2012**, *85*, 101-13.

(7) Lohse, S. E.; Murphy, C. J. *J. Am. Chem. Soc.* **2012**, *134*, 15607-20.

(8) Dahl, J. A.; Maddux, B. L. S.; Hutchison, J. E. *Chem. Rev.* **2007**, 2228-2269.

(9) Daniel, M.-C.; Astruc, D. *Chem. Rev.* **2004**.

(10) Zhao, P.; Li, N.; Astruc, D. *Coord. Chem. Rev.* **2013**, *257*, 638-665.

(11) Hutchison, J. E. *ACS Nano* **2008**, *2*, 395-402.

(12) Sweeney, S. F.; Woehrle, G. H.; Hutchison, J. E. *J. Am. Chem. Soc.* **2006**, 5220-5227.

(13) Richman, E. K.; Hutchison, J. E. *ACS Nano* **2009**, *3*, 2441-2446.

(14) Grainger, B.; Castner, D. *Adv. Mater.* **2008**, *20*, 867-877.

(15) Templeton, A.; Wuelfing, W.; Murray, R. W. *Acc. Chem. Res.* **2000**, *33*, 17-36.

(16) Skoog, A. S.; Holler, F. J.; Niemann, T. A. *Principles of Instrumental Analysis 5th ed.*; Saunders Publishing, **1998**.

(17) Lim, T. H.; McCarthy, D.; Hendy, S. C.; Stevens, K. J.; Brown, S. A.; Tilley, R. D. *ACS Nano* **2009**, *3*, 3809-13.

(18) Woehrle, G. H.; Hutchison, J. E.; Ozkar, S.; Finke, R. G. *Turk. J. Chem.* **2006**, *30*, 1-13.

(19) Haben, P. M.; McKenzie, L. C.; Kevan, S. D.; Hutchison, J. E. *J. Phys. Chem. C* **2010**, *114*, 22055-22063.

(20) Emilio, P.; Nunzio, D.; Martelli, S.; Bitti, R. R. *J. Dispersion Sci. Technol.* **2004**, *25*, 491-501.

(21) Haiss, W.; Thanh, N. T. K.; Aveyard, J.; Fernig, D. G. *Anal. Chem.* **2007**, *79*, 4215-4221.

(22) Koerner, H.; Maccuspie, R. I.; Park, K.; Vaia, R. A. *Chem. Mater.* **2012**, *24*, 981-995.

(23) Pecora, R. *J. Nanopart. Res.* **2000**, *2*, 123-131.

(24) Wyatt Technology Corporation. DYNAMICS Users Guide. **2010**.

(25) Tobler, D. J.; Shaw, S.; Benning, L. G. *Geochim. Cosmochim. Acta* **2009**, *73*, 5377-5393.

(26) Bell, N. C.; Minelli, C.; Tompkins, J.; Stevens, M. M.; Shard, A. G. *Langmuir* **2012**, *28*, 10860-10872.

(27) Glatter, O.; Kratky, O. *Small Angle X-ray Scattering*, **1982**.

(28) Bienert, R.; Emmerling, F.; Thuenemann, A. F. *Anal. Bioanal. Chem.* **2009**, 1651-1660.

(29) Fratzl, P. *J. Appl. Crystallogr.* **2003**, *36*, 397-404.

(30) Polte, J.; Erler, R.; Thunemann, A. F.; Sokolov, S.; Ahner, T. T.; Rademann, K.; Emmerling, F.; Kraehnert, R. *ACS Nano* **2010**, *4*, 1076-1082.

(31) Alceo, M.; Ciancaleoni, G.; Zuccaccia, C.; Zuccaccia, D. *Supramolecular Chemistry: From Molecules to Nanomaterials* **2012**, *2*, 319-330.

(32) Terrill, R. H.; Postlethwaite, T. A.; Poon, C.-h. C. C.-d.; Terzis, A.; Chen, A.; Hutchison, J. E.; Clark, M. R.; Wignall, G.; Londono, J. D.; Superfine, R.; Falvo, M.; Johnson Jr, C. S.; Samulski, E. T.; Murray, R. W. *J. Am. Chem. Soc.* **1995**, *117*, 12537-12548.

(33) Salorinne, K.; Lahtinen, T.; Koivisto, J.; Kalenius, E.; Nissinen, M.; Pettersson, M.; Hakkinen, H. *Anal. Chem.* **2013**, *85*, 3489-3492.

(34) Carney, R. P.; Kin, J. Y.; Qian, H.; Jin, R.; Mehenni, H.; Stellacci, F.; Bakr, O. M. *Nat. Commun.* **2010**, *2*, 1-8.

(35) Planken, K. L.; Colfen, H. *Nanoscale* **2010**, *2*, 1849-1869.

(36) Zook, J. M.; Rastogi, V.; Maccuspie, R. I.; Keene, A. M.; Fagan, J. *ACS Nano* **2011**, *5*, 8070-8079.

(37) Pristinski, D.; Chastek, T. Q. *Meas. Sci. Technol.* **2009**, *20*.

(38) Borchert, H.; Shevchenko, E. V.; Robert, A.; Mekis, I.; Kornowski, A.; Grubel, G.; Weller, H. *Langmuir* **2005**, 1931-1936.

(39) Benetatos, N. M.; Smith, B. W.; Heiney, P. A.; Winey, K. I. *Macromolecules* **2005**, 9251-9257.

(40) Roebben, G.; S, R.-G.; Hackley, V. A.; Roesslein, M.; Klasessig, F.; Kestens, V.; Lynch, I.; Gerner, C. M.; Rawle, A.; Elder, A.; Colvin, V. L.; Kreyling, W.; Krug, H. F.; Lewicka, Z. A.; McNeil, S.; Nel, A.; Patri, A.; Wick, P.; Wiesner, M.; Xia, T.; Oberdorster, G.; Dawson, K. A. *J. Nanopart. Res.* **2011**, *13*, 1675-2687.

(41) Bhattacharyya, S.; Kudgus, R. a.; Bhattacharya, R.; Mukherjee, P. *Pharm.l Res.* **2011**, *28*, 237-59.

(42) Cheng, Z.; Al Zaki, A.; Hui, J. Z.; Muzykantov, V. R.; Tsourkas, A. *Science* **2012**, *338*, 903-10.

(43) Sardar, R.; Funston, A. M.; Mulvaney, P.; Murray, R. W. *Langmuir* **2009**, *25*, 13840-13851.

(44) Brust, M.; Fink, J.; Bethell, D.; Schiffrin, D. J.; Kiely, C. *J. Chem. Soc., Chem. Commun.* **1995**, 1655-1656.

(45) Brust, M.; Walker, M.; Bethell, D.; Schiffrin, D. J.; Whyman, R. *J. Chem. Soc., Chem. Commun.* **1994**, 801-802.

(46) Shon, Y.-S.; Gross, S. M.; Dawson, B.; Porter, M.; Murray, R. W. *Langmuir* **2000**, *16*, 6555-6561.

(47) Turkevich, J. *Gold Bull.* **1985**, *18*, 86-91.

(48) Turkevich, J. *Gold Bull.* **1985**, *18*, 125-131.

(49) Haben, P.M.; Elliott III, E.W.; Hutchison, J.E. *Submitted for publication.*

(50) Lohse, S. E.; Dahl, J. A.; Hutchison, J. E. *Langmuir* **2010**, *26*, 7504-11.

(51) Ojea-Jimenez, I.; Bastus, N.; Puntes, V. *J. Phys. Chem. C* **2011**, *2*, 15752-15757.

(52) Ilavsky, J.; Jemian, P. R. *Appl. Crystallogr.* **2009**, 347-353.

(53) Kearns, G. J.; Foster, E. W.; Hutchison, J. E. *Anal. Chem.* **2006**, *78*, 298-303.

Chapter VI

(1) Dahl, J. A.; Maddux, B. L. S.; Hutchison, J. E. *Chem. Rev.* **2007**, 2228-2269.

(2) Daniel, M.-C.; Astruc, D. *Chem. Rev.* **2004**, *104*, 293-346.

(3) Grainger, B. D. W.; Castner, D. G. *Adv. Mater.* **2008**, 867-877.

(4) Haruta, M. *Gold Bull.* **2004**, 27-36.

(5) Hodes, G. *Adv. Mater.* **2007**, *19*, 639-655.

(6) Polte, J.; Tuaev, X.; Wuithschick, M.; Fischer, A.; Theunemann, A.; Rademann, K.; Kraehnert, R.; Emmerling, F. *ACS Nano* **2012**, *6*, 5791-5802.

(7) Koerner, H.; Maccuspie, R. I.; Park, K.; Vaia, R. A. *Chem. Mater.* **2012**, *24*, 981-995.

(8) Peng, Z.; Peng, X. *J. Am. Chem. Soc.* **2002**, *124*, 3343-53.

(9) Woehl, T. J.; Evans, J. E.; Arslan, I.; Ristenpart, W. D.; Browning, N. D. *ACS Nano* **2012**, *6*, 8599-8610.

(10) Becker, R.; Doring, W. *Annalen der Physik* **1935**, *5*, 1935.

(11) Frenkel, J. *J. Chem. Phys.* **1939**, *7*, 538-547.

(12) Dinegar, H.; LaMer, V. *J. Am. Chem. Soc.* **1950**, *72*.

(13) Sugimoto, T. *Adv. Coll. Inter. Sci.* **1987**, *28*, 65-108.

(14) Marmiroli, B.; Grenci, G.; Cacho-Nerin, F.; Sartori, B.; Ferrari, E.; Laggner, P.; Businaro, L.; Amenitsch, H. *Lab Chip* **2009**, 2063-2069.

(15) Robb, D. T.; Privman, V. *Langmuir* **2008**, *24*, 26-35.

(16) Zhao, C.-X.; He, L.; Qiao, S. Z.; Middelberg, A. P. J. *Chem. Eng. Sci.* **2011**, *66*, 1463-1479.

(17) Abecassis, B.; Testard, F.; Kong, Q.; Francois, B.; Spalla, O. *Langmuir* **2010**, *26*, 13847-13854.

(18) Tsunoyama, H.; Ichikuni, N.; Tsukuda, T. *Langmuir* **2008**, 11327-11330.

(19) Caragheorgheopol, A.; Chechik, V. *Phys. Chem. Chem. Phys.* **2008**, 5029-5041.

(20) Richman, E. K.; Hutchison, J. E. *ACS Nano* **2009**, *3*, 2441-2446.

(21) Polte, J. r.; Ahner, T. T.; Delissen, F.; Sokolov, S.; Emmerling, F.; Thuenemann, A. F.; Kraehnert, R. *J. Am. Chem. Soc.* **2010**, *132*, 1296-301.

(22) Polte, J. r.; Erler, R.; Thu, A. F.; Sokolov, S.; Ahner, T. T.; Rademann, K.; Emmerling, F.; Kraehnert, R. *ACS Nano* **2010**, *4*, 1076-1082.

(23) Haben, P. M.; McKenzie, L. C.; Kevan, S. D.; Hutchison, J. E. *J. Phys. Chem. C* **2010**, *114*, 22055-22063.

(24) Cabeza, V. S.; Kuhn, S.; Kulkarni, A. a.; Jensen, K. F. *Langmuir* **2012**, *28*, 7007-13.

(25) Harada, M.; Tamura, N.; Takenaka, M. *J. Phys. Chem. C* **2011**, *115*, 14081-14092.

(26) Abecassis, B.; Testard, F.; Spalla, O.; Barboux, P. *Nano Letters* **2007**, *7*, 1723-1727.

(27) Bremholm, M.; Felicissimo, M.; Iversen, B. B. *Angew. Chem. Int. Ed.* **2009**, 4788-4791.

(28) Hubert, F.; Testard, F.; Thill, A.; Kong, Q.; Tache, O.; Spalla, O. *Cryst. Growth Des.* **2012**, *12*, 1548-1555.

(29) Wang, W.; Zhang, K.; Cai, Q.; Mo, G.; Xing, X. Q.; Cheng, W. D.; Chen, Z. J.; Wu, Z. H. *Eur. Phys. J. B* **2010**, *76*, 301-307.

(30) Haiss, W.; Thanh, N. T. K.; Aveyard, J.; Fernig, D. G. *Anal. Chem.* **2007**, *79*, 4215-4221.

(31) Polte, J. r.; Emmerling, F.; Radtke, M.; Reinholz, U.; Riesemeier, H.; Thuenemann, A. F. *Langmuir* **2010**, *26*, 5889-94.

(32) Tanaka, T.; Ohyama, J.; Teramura, K.; Hitomi, Y. *Catal. Today* **2012**, *183*, 108-118.

(33) Beale, A. M.; Eerden, A. M. J. V. D.; Jacques, S. D. M.; Leynaud, O.; Brien, M. G. O.; Meneau, F.; Nikitenko, S.; Bras, W.; Weckhuysen, B. M. *J. Am. Chem. Soc.* **2006**, 12386-12387.

(34) Lohse, S. E.; Dahl, J. A.; Hutchison, J. E. *Langmuir* **2010**, *26*, 7504-11.

(35) Fealy, R. J.; Ackerman, S. R.; Ferguson, G. S. *Langmuir* **2011**, *27*, 5371-6.

(36) Shon, Y.-S.; Gross, S. M.; Dawson, B.; Porter, M.; Murray, R. W. *Langmuir* **2000**, *16*, 6555-6561.

(37) Haben, P.M.; Elliott III, E.W.; Hutchison, J.E. *Submitted for publication.*

(38) Glatter, O.; Kratky, O. *Small Angle X-ray Scattering*, **1982**.

(39) Ilavsky, J.; Jemian, P. R. *Appl. Crystallogr.* **2009**, 347-353.

(40) Paclawski, K.; Streszewski, B.C.; Jaworski, W.; Luty-Blocho, M.; Fitzner, K. *Colloids Surf., A* **2012**, *413*, 208-215.

(41) Wu, J.; Ferrance, J. P.; Landers, J. P.; Weber, S. G. *Anal. Chem.* **2010**, *82*, 7267-7273.

(42) Saunders, A. E.; Sigman Jr, M. B.; Korgel, B. A. *J. Phys. Chem. B* **2004**, 193-199.

(43) Owen, J. S.; Chan, E. M.; Liu, H.; Alivisatos, A. P. *J. Am. Chem. Soc.* **2010**, *132*, 18307-18213.

(44) Suh, C. W.; Hwang, S. Y.; Choi, H. J.; Seong, G. H.; Ahn, Y. M.; Kim, Y. S.; Lee, E. K. *Biotechnol. Bioprocess Eng.* **2004**, *9*, 132-136.

(45) Talapin, D. V.; Rogach, A. L.; Haase, M.; Weller, H. *J. Phys. Chem. B* **2001**, *105*, 12278-12285.

(46) Bastus, N. G.; Comenge, J.; Puntes, V. *Langmuir* **2011**, *27*, 11098-11105.

(47) Fujii, T.; Onaka, S.; Mori, T.; Kato, M. *ISIJ International* **1992**, *32*, 28-29.

(48) Shields, S. P.; Richards, V. N.; Buhro, W. E. *Chem. Mater.* **2010**, *22*, 3212-3225.

(49) Zheng, H.; Smith, R. K.; Jun, Y.-W.; Kisielowski, C.; Dahmen, U.; Alivisatos, A. P. *Science* **2009**, *324*, 1309-1312.

(50) Pawluk, T.; Wang, L. *J. Phys. Chem. C* **2007**, *111*, 6713-6719.

(51) Chapter V of this thesis. Manuscript in preparation.

(52) Lukkari, J.; Meretoja, M.; Kartio, I.; Laajelehto, K.; Rajamaki, M.; Lindstrom, M.; Kankare, J. *Langmuir* **1999**, *15*, 3529-3537.

Appendix B

(1) Lohse, S.E.; Dahl, J.A.; Hutchison, J.E. *Langmuir* **2010**, *26,* 10, 7504-7511

(2) Haben, P. M.; McKenzie, L. C.; Kevan, S. D.; Hutchison, J. E. *J. Phys. Chem. C* **2010**, *114*, 50, 22055-22063

(3) Ilavsky, J.; Jemian, P. R. *J. Appl. Crystallogr.* **2009**, *42*, 347-353

(4) Woehrle, G. H.; Hutchison, J. E.; Ozkar, S.; Finke, R. G. *Turk. J. Chem.* **2006**, *30*, 1-13

(5) Sweeney, S. F.; Woehrle, G. H.; Hutchison, J. E. *J. Am. Chem. Soc.* **2006**, *128*, 12, 5220-5227

(6) Pecsok, R. L. *J. Am. Chem. Soc.* **1953**, *75*, 2862-2864

(7) Wang, S.; Qian, K.; Bi, X.; Huang, W. *J. Phys. Chem. C* **2009**, *113*, 16, 6505-6510

(8) Woehrle, G.H.; Warner, M.G.; Hutchison, J.E. *Langmuir* **2004**, *20*, 5982-5988